이학박사 학위논문

Electrical and Structural Properties of Doped $BaSnO_3$ Single Crystals and Films

전하 주입된 $BaSnO_3$ 단결정과 박막의 전기적 구조적 특성 연구

2017년 8월

서울대학교 대학원

물리천문학부

이 웅 재

Electrical and Structural Properties of Doped $BaSnO_3$ Single Crystals and Films

전하 주입된 $BaSnO_3$ 단결정과 박막의 전기적 구조적 특성 연구

지도 교수 김 기 훈

이 논문을 이학박사 학위논문으로 제출함

2017년 8월

서울대학교 대학원

물리천문학부

이 웅 재

이웅재의 이학박사 학위논문을 인준함

2017년 8월

위 원 장 이 탁 희 (인)

부위원장 김 기 훈 (인)

위 원 유 재 준 (인)

위 원 이 규 철 (인)

위 원 박 재 훈 (인)

Electrical and Structural Properties of Doped $BaSnO_3$ Single Crystals and Films

Woong-Jhae Lee

Supervised by

Professor Kee Hoon Kim

A dissertation Submitted to the Faculty of

Seoul National University

in Partial Fulfillment of

the Requirements for the Degree of

Doctor of Philosophy

August 2017

Department of physics and Astronomy

Graduate School

Seoul National University

Abstract

Transparent conducting oxides (TCOs) and transparent oxide semiconductors (TOSs) have become necessary materials for a variety of applications in the information and energy technologies, ranging from transparent electrodes to active electronics components. Perovskite barium stannate ($BaSnO_3$), a new TCO or TOS system, is a potential platform for realizing optoelectronic devices and observing novel electronic quantum states due to its high electron mobility, stable electrical properties, high transparency, structural versatility, and flexible doping controllability. Recently, we discovered that La doped $BaSnO_3$ (BLSO) single crystals exhibited the highest electron mobility of 320 $cm^2V^{-1}s^{-1}$ at electron carrier density of ~10^{20} cm^{-3} among perovskite oxides and stable electrical properties at high temperatures. However, most BLSO films grown on the $SrTiO_3$(001) substrates have shown much lower electron mobility (10–70 $cm^2V^{-1}s^{-1}$) due to the large lattice mismatch between the films and the substrates. While there is great potential to increase electron mobility in doped $BaSnO_3$ films by defect minimization, heterostructure engineering provides another promising route for achieving a metallic state at the interface between the $BaSnO_3$(001) substrates and the insulating perovskite oxide layers.

Finding a suitable substrate to grow BLSO thin films has been one of major challenges. An ideal substrate would be the insulating $BaSO_3$ single crystal itself, as its lattice constant matches well with those of BLSO within 0.08%. Chapter three of this dissertation discusses the growth of insulating $BaSnO_3$(001) single crystals as a substrate. The insulating $BaSnO_3$(001) substrates were grown by the Cu_2O-CuO flux, in which the molar fraction of $KClO_4$ was systematically increased to reduce electron carrier density and thus induce a doping induced metal-insulator transition, exhibiting a resistivity increase from ~10^{-3} to ~10^{12} Ω cm at room temperature. By optical transmission measurement in the mid-IR to

UV light range, we observe that the crystals grown with $KClO_4$ show significantly less free-carrier absorption. Through Raman spectroscopy, we remark that the oxygen vacant $BaSnO_3$ crystals show first-order Raman scattering peaks at 138 cm^{-1} and 250 cm^{-1}, which indicates it is locally distorted even though the X-ray diffraction patterns show a cubic perovskite structure.

Chapter four introduces the enhanced electron mobility in epitaxial BLSO films grown on $BaSnO_3$(001) substrates. We find that all the degenerate BLSO films turn out to be epitaxial, showing good in-plane lattice matching with the substrate as confirmed by X-ray reciprocal space mappings and transmission electron microscopy studies. The BLSO films show degenerate semiconducting behavior, and the μ at room temperature reached 100 and 85 $cm^2V^{-1}s^{-1}$ at doping levels 1.3×10^{20} and 6.8×10^{19} cm^{-3}, respectively. We also show that a field-effect transistor with the homo-epitaxial $BaSnO_3$ film as an active channel exhibits an on/off ratio of 1.2×10^6 and a high field-effect mobility of 48.7 $cm^2V^{-1}s^{-1}$, being comparable to those of the well-known binary oxides and superior to those of the other perovskite materials. This work demonstrates that thin perovskite stannate films of high quality can be grown on the $BaSnO_3$ (001) substrates for potential applications in transparent electronic devices.

Chapter five discusses the oxygen diffusion phenomena in a BLSO thin film on $SrTiO_3$(001) substrate by measurements of time-dependent Hall effect at high temperatures around 500 ^oC under different gas atmosphere. Under the Ar (O_2) atmosphere, electron carrier density and electrical conductivity are increased (decreased) while electron mobility is slightly reduced (enhanced). This observation supports that although both electron carrier density and electron mobility are affected by the oxygen diffusion process, the change of electron carrier density is a major factor of determining electrical conductivity in the BLSO

films. Detailed analyses of the time-dependent electron carrier density exhibit fast and slow dynamics that possibly correspond to the oxygen exchange reaction at the surface and oxygen diffusion into the BLSO grains, respectively. Fitting the time-dependence of electron carrier density reveals that the chemical diffusion coefficient of oxygen in the BLSO grains becomes ~10^{-16} cm^2s^{-1}. This coefficient marks the lowest value among perovskite oxides around 500 °C, directly proving stable electrical properties of BLSO. These results support that the donor-doped $BaSnO_3$ system could be useful for realizing transparent semiconductor devices at high temperatures.

Chapter six introduces the realization of atomically flat terraces with nearly single SnO_2 layer-termination on the $BaSnO_3$(001) substrate with lateral dimension about 3 × 3 mm^2 by deionized water leaching and thermal annealing. The surface topography shows the evolution of the surface from chemically mixed termination to atomically flat single terminated surfaces with step-terrace structures of one unit cell step height of ~4.116 Å. The influence of out-of-plane and in-plane miscut angles on the surface, i.e., step bunching and kinked steps, is described. The single-terminated $BaSnO_{3-\delta}$(001) substrate has been studied by X-ray photoemission spectroscopy. From the Ba3$d_{5/2}$ and Sn3$d_{5/2}$ signals with its angle dependence, we confirmed that the topmost atomic layer of $BaSnO_{3-\delta}$(001) surface mostly consists of SnO_2 rather than BaO and that deoxidized Ba sources exist on the surface of $BaSnO_{3-\delta}$(001) substrates. These observations facilitate the preparation of atomically aligned $BaSnO_3$(001) substrates, which opens doors for realization of two-dimensional electron gases at the interface between $BaSnO_3$(001) and other oxides.

Chapter seven discusses the pathways to achieve two-dimensional electron gases at the interface between $BaSnO_3$ and other perovskite oxides. Theoretical predictions for two-dimensional electron gases (2DEGs) at the heterojunction of $BaSnO_3$ with $KTaO_3$, $LaAlO_3$,

$KNbO_3$, $LaAlO_3$, $SrTiO_3$, $CaSnO_3$, $SrSnO_3$, $SrHfO_3$, $SrZrO_3$, and $LaInO_3$ are introduced. Experimental efforts on 2DEGs in $BaSnO_3$ are presented and remaining challenges for observing novel quantum phenomena at the heterointerface between $BaSnO_3$ and candidate barrier materials are described. By employing modulation or polar discontinuity doping on the SnO_2-terminated $BaSnO_3$(001) substrates, superconductivity or quantum Hall effects in the $BaSnO_3$ system at ambient temperature may well be discovered.

Keyword : $BaSnO_3$, single crystal growth, thin film growth, high mobility, thermal stability, perovskite, heterostructure

Student Number : 2012-30900

Contents

List of Tables

List of Figures

Chapter 1 Introduction

1.1 Transparent conducing oxides and transparent oxide semiconductors

Transparent conducting oxides (TCOs) or transparent oxide semiconductors (TOSs) often refer to the materials having simultaneously electrical conductivity (~10^{-8} – 10^{3} $S \cdot cm^{-1}$) and high optical transmission (≥ 80 %). The combination of the two important features makes TCOs or TOSs key materials for the passive or active components in various modern optoelectronic or electronic devices (1-5). For example, transparent electrical leads, pn junctions, and field-effect transistors have been heavily used in liquid crystal displays (6), organic light-emitting diodes (7), solar cells (8), light-emitting diodes (9), and gas sensors (10) etc. (11) (Fig 1.1). Moreover, there exist increasing demands for the new TCOs or TOSs for next generation devices related to the information and energy technologies.

Figure 1.1 Varieties of industrial applications employing transparent conducting oxides & transparent oxide semiconductors. A central photograph and its expanded view represent the transparent $(In,Sn)_2O_3$ film on the glass substrate and $(Ba,La)SnO_3$ film on the $BaSnO_3(001)$ substrate. Image of transparent-flexible electronics adapted from Reference (*6*). Images of LCD and OLED, touch panels, transparent displays, and virtual reality in panel a from https://news.samsung.com/global.

Table 1.1 electrical properties of prototypical n-type TCOs at 300 K in a degenerate regime (high carrier concentrations above 10^{18} cm^{-3})

		In_2O_3	**SnO_2**	**ZnO**	**CdO**	**β-Ga_2O_3**	**a-$InGaZnO_4$**	**$SrTiO_3$**	**$BaSnO_3$**
Crystal structure		Bixbyite	Rutile	Wultzite	Rocksalt	Monoclinic	Non-crystalline solid	Perovskite	Perovskite
Band Gap type		Indirect	Direct	Direct	Direct	Direct	Indirect	Indirect	Indirect
E_g (eV)		2.7	3.6	3.4	2.28	4.9	3.2	3.2	2.95
Electron effective mass (m_0)		0.35	0.25	0.28	0.24	0.34	0.35	4.8	0.2-0.4
Dielectric constant		9	9.6 – 13.5	8.8 – 8.75	21.9	10	13	320	20
Dopant	Film	Sn	Ta	Al	Dy	Sn	V_O	La	La
	Crystal	Sn	V_O or I_{sn} **a**	V_O or I_{Al}	V_O	V_O		La	La
Electron density (cm^{-3})	Film	2.0×10^{20}	2.7×10^{20}	7.9×10^{20}	5.0×10^{19}	1.5×10^{19}	1.0×10^{20}	4.0×10^{18}	8.0×10^{19}
	Crystal	1.6×10^{20}	1.3×10^{17} **b**	4.1×10^{16}	6.0×10^{19}	9.6×10^{16} **b**	-	6.8×10^{20}	1.0×10^{20}
Electrical Conductivity (S/cm)	Film	3.1×10^{3}	3.6×10^{3}	1.0×10^{4}	4.0×10^{3}	79.3	160	6.4	1.9×10^{3}
	Crystal	2.5×10^{3}	5.0	1.6	96.1	2.4	-	9.8×10^{2}	5.1×10^{3}
Maximum Hall mobility ($cm^2/V{\cdot}s$)	Film	96 (*12*)	83 (*13*)	79 (*14*)	500 (*15*)	33 (*16*)	10	10 (*17*)	150 (*18*)
	Crystal	98 (*19*)	240 (*20*)	239 (*21*)	10 (*22*)	153 (*23*)	-	9 (*24*)	320 (*25*)
Reference		(*26*)	(*27, 28*)	(*29, 30*)	(*31, 32*)	(*33, 34*)	(*35, 36*)	(*37-39*)	(*25, 40*)

a) Cation interstitial

b) Non-degenerate semiconductor regime

The majority of known TCOs or TOSs are n-type semiconductors in which oxygen vacancies (V_O), ionized donor substitutions, and cation interstitials usually donate electrons to the conduction band, providing electron carriers for the flow of electric current (*41*). The

most archetypal n-type TCO is the Sn-doped In_2O_3 (ITO), which has been heavily used by more than six decades in industries and academies as passive transparent electrical leads (*26*). Other n-type TCOs include the F-doped SnO_2 (*28*), Al-doped ZnO (*29*), and so on (*12-25, 42, 43*). These well-known n-type TCOs have typically electron carrier concentrations (n) from 10^{18} to 10^{21} cm^{-3} and electron mobility (μ) from 10 to 100 $cm^2V^{-1}s^{-1}$, depending on the material qualities and growth conditions. These rather large mobility values are coined to the characteristic electronic structure of the n-type TCOs, in which the conduction band is mostly composed of spatially delocalized, metallic *s* orbitals to result in large dispersion and low electron effective mass. Such a characteristic condition is fulfilled in oxide materials with the cations having the closed-shell configuration of $4s^0$ or $5s^0$; In(III), Sn(IV), Zn(II), Cd(II), or Ga(III) (*44, 45*). For example, Fig. 1.2(a) shows the electronic band structure for In_2O_3 with a dispersive conduction band composed of mainly In 5*s* states (*46*). The large dispersion and small effective mass is thus a necessary condition to achieve a high electrical mobility in a given material system.

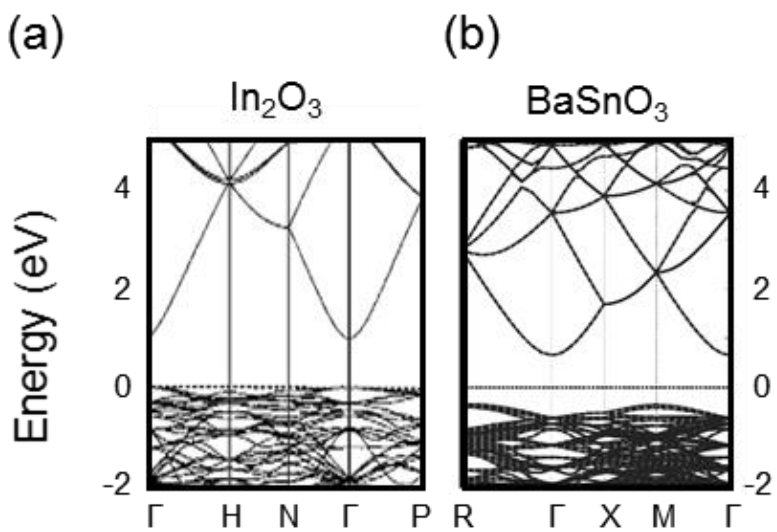

Figure 1.2 Band structures of In_2O_3 and $BaSnO_3$, respectively. adapted with permission from Reference (*46*) and Reference (*40*).

However, many known TCOs or TOSs still have their own limitations so that there have existed active scientific searches for finding alternative materials, which could potentially exhibit better physical properties. First, the overwhelming demands for ITO as transparent electrodes, coupled with the low natural abundance of indium, have made indium an increasingly expensive commodity, which has led to a large research drive to search for an alternative material (*47*). Second, for the long-term reliability of oxide electronic devices particularly operating in air, electrical stability of TCOs is crucial for overcoming interface degradation problems frequently observed in the oxide pn junctions and transistors. For example, the resistance of ZnO films at room temperature changed by 10^4 times after heat treatment at 400 ^oC for 2 hour (*48*). Such unstable electrical properties probably stem from the unstable properties of oxygen at high temperatures, which can also cause various unstable phenomena such as persistent current in the channel after photon irradiation and unstable p-type properties (*49, 50*). Thus, the realization of stable p-type TCOs remains as one of major challenges in oxide electronics (*51*). Third, the high carrier mobility is one of important ingredients for developing fast logic devices because it fundamentally limits the operation speed across the device (*52, 53*). Finally, controlling and minimizing the density of defects or dislocations become also important for realizing highly efficient devices based on TCOs or TOSs.

The materials with the perovskite structure have exhibited a plethora of interesting physical properties, such as large photovoltaic effects (*54, 55*), superconductivity (*56-58*), colossal magnetoresistance (*59*), ferroelectricity (*60, 61*), and multiferroicity (*62, 63*), etc. Extensive researches have been performed to utilize such versatile physical properties in the form of a single layered thin film and their heterostructures (*64, 65*). There have also been growing interests toward new perovskite TCOs, in which carrier doping and structural modification can be more flexible than those conventional ones made of binary oxides. Most studied perovskite oxides in this context are doped $SrTiO_3$ and $KTaO_3$, in which μ

soars up to 32,667 $cm^2V^{-1}s^{-1}$ for $SrTiO_3$ and 23,000 $cm^2V^{-1}s^{-1}$ for $KTaO_3$ at temperatures ~2 K (*17, 66*). This large μ was achieved by the high dielectric constants (ε_{STO} = ~20,000 and ε_{KTO} = ~4,500) at low temperatures, which helps reduce the ionic dopant scattering due to high dielectric screening. However, these perovskite oxides generally showed much lower μ (~1− 30 $cm^2V^{-1}s^{-1}$) (*66, 67*) than those doped binary oxides at room temperature, which has hindered practical device applications.

1.2 Transparent perovskite barium stannate : $BaSnO_3$

The alkaline-earth stannates with the chemical formula $ASnO_3$ (*A* = Ca, Sr, or Ba) are another perovskite oxides that have brought recent attentions. With systematic increase of the A-site effective ionic radius (r_A) from Ca^{2+} (100 pm) to Sr^{2+} (118 pm) to Ba^{2+} (135 pm) (*68*), the structure changes from the distorted perovskite structure with Pnma ($CaSnO_3$ and $SrSnO_3$) to $Pm\bar{3}m$ ($BaSnO_3$) (*69*) (Fig 1.3(b)). At the same time, their Goldschmidt tolerance factor defined by $(r_A + r_O)/\sqrt{2}(r_B + r_O)$ systemically increases from 0.927 to 0.961 to 1.018 with systematic reduction of the optical band gap (E_g) from 4.4 eV to 4.0 eV to 3.0 eV, respectively (*70, 71*). Although many novel physical properties await further attentions toward this series of $ASnO_3$, the author mainly focuses on $BaSnO_3$ in the dissertation.

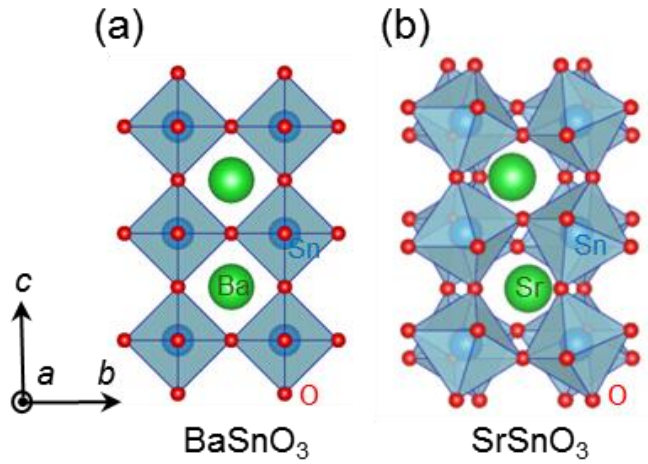

Figure 1.3 Crystal structures of (a) $BaSnO_3$ and (b) $SrSnO_3$ having the cubic and the orthorhombic perovskites, respectively.

The $BaSnO_3$ is a transparent, wide-band-gap semiconductor with the E_g = ~3.1 eV and forms a structure close to the ideal cubic perovskite (*71*). Its structure is characterized as a three-dimensional framework of corner-sharing SnO_6 octahedra, in which the Sn-O-Sn bonding angle is close to 180 ◦ and thus the tolerance factor is close to 1 (Fig 1.3(a)). This bonding feature allows one to achieve enhanced electron hopping between neighboring Sn sites, constituting a physical origin for resulting in the conduction band with large dispersion. Figure 1.2(b) presents the electronic band structure of $BaSnO_3$ as calculated by density functional theory (DFT) calculations with local density approximation (LDA) functional, exhibiting considerably dispersive conduction band, mainly composed of Sn 5s states (*40*). Similar band calculation results can also be found from the earlier works by Singh et al. in 1991 (*72*) and Mizoguchi et al. in 2004 (*71*). It is worth noting that such large dispersion and wide band gap is a common property of both $BaSnO_3$ and In_2O_3 although they have completely different crystal structures and electronic states in the conduction band. Accordingly, Mizoguchi et al. firstly pointed out that $BaSnO_3$ with large dispersion could be potentially a good TCOs (*71*). However, the formerly reported μ in the

thin films and poly-crystals of electron-doped BaSnO3 was relatively low, being less than 1 $cm^2V^{-1}s^{-1}$, and the conductivity reached 250 $S{\cdot}cm^{-1}$ at most (*73*-*75*). It is likely that those earlier specimens were subjects to severe extra-scattering, possibly from off stoichiometry, poor crystallinity, or grain boundaries. Therefore, the growth of high quality single crystals of doped $BaSnO_3$ has been highly demanding to understand their intrinsic physical properties.

With motivations of searching for an alternative TCOs and finding out intrinsic physical properties of the doped $BaSnO_3$, we have undertaken systematic efforts of growing single crystals and high quality thin films of $BaSnO_3$, $(Ba,La)SnO_3$ (BLSO), and $Ba(Sn,Sb)O_3$ (BSSO) since 2009. With these efforts, we have discovered that BLSO single crystals produced unusually high μ up to 320 $cm^2V^{-1}s^{-1}$ at room temperature and optical transparency with enhanced E_g ($\geq$ 3.1 eV) (*25*, *40*). At room temperature, the value of μ = 320 $cm^2V^{-1}s^{-1}$ was the highest among the perovskite oxides in a degenerate semiconductor regime. Moreover, we found stable electrical properties of BLSO, i.e., less than 2 % changes of conductivity under air atmosphere at high temperatures of 530 ^oC (*25*). Therefore, the doped $BaSnO_3$ system can potentially overcome the problems caused by the thermal instability of oxygen in the oxide electronic devices (*76*). More importantly, the new perovskite stannates with both high μ and stable electrical properties could be combined with other perovskite materials with diverse physical properties, and thus realize "all-perovskite" oxide electronic devices having exotic physical properties of constituent materials or having unexpected novel quantum phenomena at the hetero-interface at ambient temperatures. In the following Chapter 2, the author will introduce the effort to growth high crystalline insulating $BaSnO_3$(001) substrates by use of flux methods with additive chemical of $KClO_4$.

Chapter 2 Experimental methods

2.1 Single crystal growth of insulating $BaSnO_3$

Polycrystalline $BaSnO_3$ powders were first synthesized and was used as the seed material for $BaSnO_3$ single crystal growth. High purity $BaCO_3$ and SnO_2 powders were weighed in stoichiometric ratio. The mixture of powders was finely ground and pressed into a pellet. The first calcination was done at 1250 ℃ for 8 hours and after an intermediate grinding, the pellet was sintered at 1350 ℃ for 20 hours. X-ray diffraction patterns indicated that the polycrystalline sample is a single phase $BaSnO_3$. For the growth of single crystals, polycrystalline $BaSnO_3$ powders and a mixture of CuO and Cu_2O flux with an additional compound $KClO_4$ were put into a Pt crucible with a molar ratio of $BaSnO_3$: CuO : Cu_2O : $KClO_4$ = 1 : 22.4 : 27.6 : y ($0.0 \leq y \leq 3.0$). It was fired in air up to 1230 ℃ and then slowly cooled to 1070 ℃. We could grow highly insulating $BaSnO_3$ single crystals by using mixed CuO and Cu_2O powders as a main flux with a molar ratio of CuO:Cu_2O = 39:61. In the given molar ratio, the CuO+Cu_2O flux forms an eutectic melting point at 1090 ^oC (*77*), which is lower than the melting temperature of Cu_2O flux only (1230 ^oC) by 140 ^oC. Hence, the temperature window of the crystal growth has been widened, possibly explaining why crystal sizes have increased overall (~3 × 3 mm^2). We also found that the best molar ratio of (CuO+Cu_2O) : $BaSnO_3$ for growing single crystals is ~50 : 1. $KClO_4$ has been used before as an oxidizer during the solid state synthesis under high pressure (*78, 79*). It was thus expected that $KClO_4$ could either provide additional oxygen to reduce V_O or potassium ions (K^+) as acceptors to compensate the n-type carriers by V_O in the $BaSnO_3$ crystals. Based on this motivation, the molar ratio of $KClO_4$ was systematically varied to determine the optimal condition for obtaining the most insulating transport properties; the best molar ratio of $BaSnO_3$: CuO +Cu_2O : $KClO_4$ turned out to be 1 : 50 : 2.

The EPMA study on $BaSnO_3$ crystals revealed that they contained detectable amount of K impurities (~1.4×10^{19} cm^{-3}) (*80*), indicating that electron carriers were partially reduced by compensation of hole carriers from K.

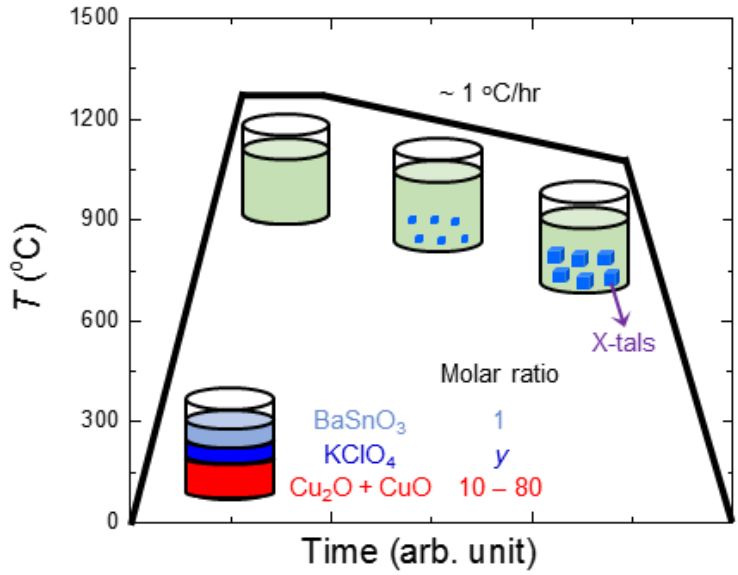

Figure 2.1 The growth of insulating $BaSnO_3$ single crystals.

2.2 Preparation for terrace-structure of $BaSnO_3$(001) substrates

Grown $BaSnO_3$ and $BaSnO_{3-\delta}$ single crystals were chemically- and mechanically-polished to have an atomically flat surface along the *c*-plane by using a polishing machine (Allied High Tech Products, Inc.) in company with polishing cloths and colloidal silica suspensions. We investigated out-of-plane miscut angle by measuring the ω-scan (ϕ scan) of the (002) peaks using X-ray diffractometer (Empyrean, PANalytical). The polished $BaSnO_3$(001) and $BaSnO_{3-\delta}$(001) substrates were cleaned by using micro-organic soap,

acetone, ethanol, and isopropanol. The cleaned substrates were agitated in deionized water for 10 sec. Thermal annealing was carried out in a resistive heating furnace using an alumina tube at temperatures between 1000 and 1300 ^{o}C for a duration of 5-100 min in 1 atm O_2 flow of 10 ml/min. The heating rate used was 600 ^{o}C/h. At the end of the heating period, the substrate was cooled to room temperature at a rate of 600 ^{o}C/h in the furnace. Surface morphology was studied by atomic force microscopy (AFM) (NX10, Park Systems) in ambient atmosphere at room temperature after the substrate was taken out from the tube furnace. In order to examine the surface termination, angle-dependent X-ray photoelectron spectroscopy (XPS) was performed using Al-Kα (1486.7 eV). As electron doping of the substrates was necessary for preventing the charging effects in the XPS measurements, conducting $BaSnO_{3-\delta}$(001) substrates were measured.

2.3 Thin film growth of doped $BaSnO_3$ by pulsed laser deposition

BLSO thin films (90 nm) were deposited by pulsed laser deposition with a KrF excimer laser (λ = 248 nm) with a laser fluence of ~1.0 J·cm^{-2}, using BLSO (x =0.00, 0.005, 0.01, 0.02, and 0.04) targets. Figure 2.2 shows our pulsed laser deposition setup since early 2014. Insulating $BaSnO_3$(001) substrates grown with $KClO_4$ (y=2.0) were used and the deposition was made in an O_2 pressure of 100 mTorr at 790 ℃.

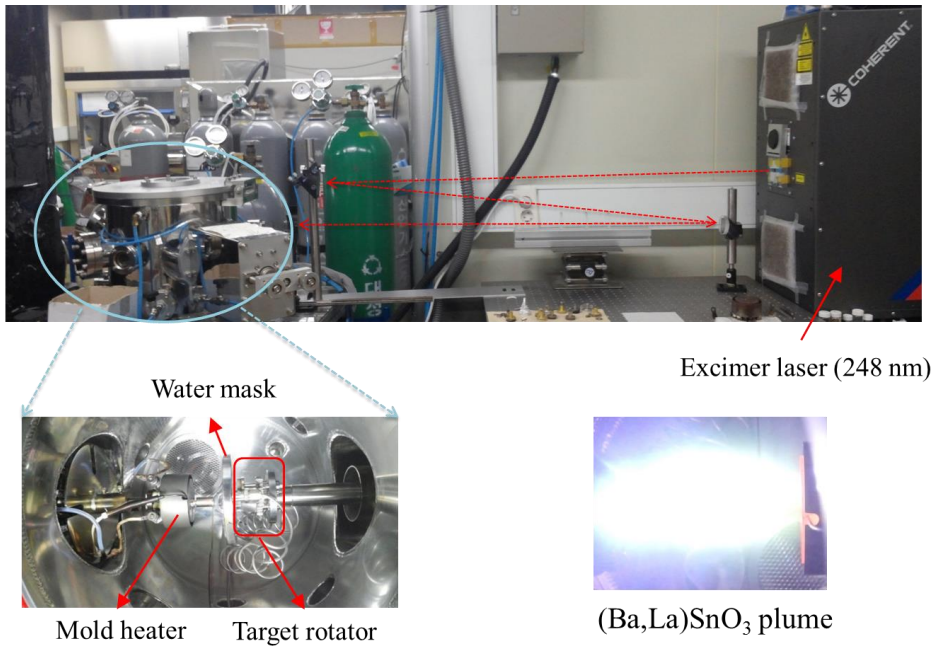

Figure 2.2 Pulsed laser deposition setup since early 2014.

2.4 Measurements of structural properties

We investigated structural properties of $BaSnO_3$ crystals and BLSO/$BaSnO_3$(001) films using high-power X-ray diffractometers (Empyrean, PANalytical and AXS D8, Bruker). The former was used for θ–2θ scans and rocking curves (ω-scans), while the latter was used for rocking curves and reciprocal space mapping (RSM). We confirmed that the rocking curves obtained from the Empyrean in a channel-reducing mode provide the same results from the AXS D8 in an open detector mode. To estimate actual La-doping levels in the grown film, we performed electron-probe microanalysis (EPMA) with spatial resolution of several micrometers. Surface morphology was studied by atomic force microscopy (AFM) (NX10, Park Systems). Transmission electron microscopy (TEM) (JEM-3000F, JEOL) experiment was performed for investigation of local structural properties of BLSO/$BaSnO_3$(001).

2.5 Measurements of electrical properties

Electric transport properties of $BaSnO_{3-\delta}$ single crystals were measured in a closed-cycle cryostat (Displex, Sumitomo Heavy Industries), in the temperature region of 10–300 K. For the highly insulating samples, the resistance was measured by a two-probe scheme while the rest were measured by a four-probe scheme. To measure the AC Hall effect measurement, the single crystals were cut and polished into a thin rectangular bar. The measurement was done in a physical property measurement system (PPMS^{TM} Quantum Design) by applying a magnetic field up to 9 T. To measure the Hall effects of BLSO thin films at room temperature, we employed the Van der Pauw method in a magnetic field of 5200 Gauss. Temperature-dependent Hall effect of BLSO/$BaSnO_3$(001) films was measured by the conventional five-wire configuration from 2 to 300 K in a magnetic field up to 9 T in a physical property measurement system (PPMS^{TM}, Quantum Design). For the electrodes, we deposited Sn-doped In_2O_3 (10% Sn) films in an O_2 pressure of 10 mTorr at 300 ℃ using the PLD technique with a metal shadow mask.

2.6 Thin-film field-effect transistors

After depositing a $BaSnO_3$ film (90 nm) on a $BaSnO_3$(001) substrate by the PLD technique as an active channel, we defined the source and drain electrodes using the metal shadow mask. The Sn-doped In_2O_3 (10% Sn) films were deposited with a thickness of 20 – 30 nm to be used as the source and the drain electrodes by the PLD in an O_2 pressure of 10 mTorr at 300 ℃, and Ti and Au layers were deposited by the thermal evaporator at room temperature. Subsequently, we deposited an amorphous Al_2O_3 (a-Al_2O_3) layer (50 nm thick) as a gate insulator using the atomic layer deposition system (D150, Lucida). The a-Al_2O_3 was deposited under the 50 sccm N_2 flow at 220 ℃ with TMA (trimethylaluminum) and H_2O sources. ε_r of a-Al_2O_3 films was measured at ~8, which is comparable to the

reported values. For the gate electrode, we used the Au layer (50 nm) deposited by the thermal evaporator with a metal shadow mask. *I-V* measurements were performed on a probe station using a semiconductor parameter analyzer (KE4200, Keithley instruments) at room temperature. The channel length (L) and gate width (W) were 150 (50) μm and 440 (200) μm, respectively, corresponding to a width-to-length ratio of 1 : 0.34 (0.25). Since many of reported L/W values in the demonstration of transistors were within 0.2 – 0.5, we thus tried to put the L/W value within this limit. We have indeed tried to change L/W values within 0.2 – 0.5 (at least 20 devices) to find more or less the same FET characteristics but the selected ones showed the best performance in terms of μ_{FE}.

2.7 Measurements of Hall effect at high temperatures

A four-probe measurement with Au contacts on $SrTiO_3$(001) substrate was also performed at 565 ^oC under O_2 and Ar atmosphere to check whether electrical conductivity σ relaxation of the BLSO film is related to that of the $SrTiO_3$(001) substrate or not. The author has set up for the Hall effect measurements at high temperatures, in which a small tube furnace combined with an electrical measurement probe and a gas flowing system is inserted between the magnetic pole of an electromagnet (V-3900, Varian). The Hall effect experiments could be carried out continuously at constant temperatures of 470 and 530 ^oC for more than 16 hours under the same O_2 or Ar atmosphere. Before the Hall effect measurements, the BLSO film was annealed under O_2 or Ar atmosphere for 16 hours to get an equilibrium state. The five-wire configuration was employed in a magnetic field (H) up to 0.45 T. The maximum time for sweeping H from -0.45 to 0.45 T took about 7 min. Therefore, the Hall data could be obtained reliably only when the effect of H on the longitudinal (V_{xx}) and transverse (V_{xy}) electrical resistivity is much larger than that of different gas environments during the 7 min. It was also important to minimize the extrinsic

sources of causing the time-dependent variation during the Hall effect measurements, for example, temperature stability of the furnace. After starting a new gas environment, V_{xx} of the BLSO film during the 7 min showed a rather large change of 0.5-1.5 % before 1 hour, making it difficult to get reliable Hall data. On the other hand, V_{xx} variation during the 7 min became less than ~0.1% after 1 hour, from which reliable Hall data could be obtained.

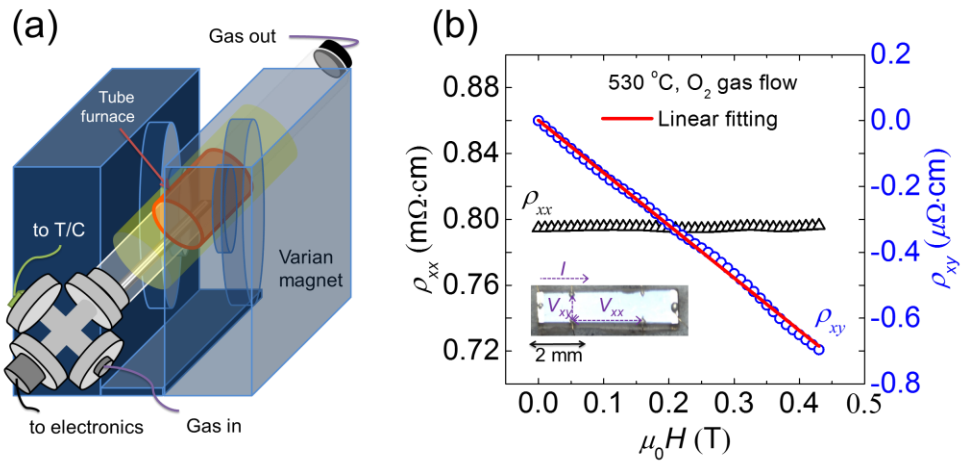

Figure 2.3 Schematic drawings of the experimental set-up for the Hall effect measurements, in which a tube furnace having an electrical measurement probe and a gas flowing system inside is inserted between the gap of an electromagnet. (b) The field-dependent ρ_{xx} (open triangles) and ρ_{xy} (open circles) of the BLSO film at 530 °C under O_2 atmosphere. The inset shows the prepared BLSO film with electrodes.

Figures 2.3(a) and (b) shows an example of V_{xx} and V_{xy} of the BLSO film at 530 °C under O_2 atmosphere. Transverse voltages (V_{xy}) measured at a positive H are subtracted from those at a negative H to determine V_{xy} while longitudinal voltages (V_{xx}) are added to extract the V_{xx} accurately. We note that after the gas exchange, the time lag for observing the σ change was usually close to or less than 3 min in our experiments. We thus expect that the time for changing gas atmosphere in the vicinity of the sample should be approximately 3 min.

Chapter 3 Properties of insulating $BaSnO_{3-\delta}$(001) single crystals

3.1 Overview

It was recently found that La-doped $BaSnO_3$ with the cubic perovskite structure, (Ba,La)SnO_3 (BLSO) single crystals, becomes n-type TOSs and TCOs with high μ (320 $cm^2V^{-1}s^{-1}$) (*25*, *40*), wide band gap (> 3.1 eV), and excellent thermal stability (*25*, *76*). One of next necessary steps for applications is to grow high-quality thin films that exhibit high μ as in the single crystals even in a low doping regime. Until recently, most of reported BLSO films were grown on $SrTiO_3$(001) substrates (BLSO/$SrTiO_3$), of which lattice constant (~3.905 Å) has a large mismatch of +5.40 % with that of $BaSnO_3$(001) (~4.116 Å). As a result, lots of threading dislocations were found to exist in BLSO/$SrTiO_3$ (*40*) (*81*). Naturally, the μ value was limited to ~40 – 60 $cm^2V^{-1}s^{-1}$ at high carrier concentrations (n) (> 2×10^{20} cm^{-3}) and was smaller than 30 $cm^2V^{-1}s^{-1}$ in a low n regime (< 7×10^{19} cm^{-3}). This is in sharp contrast with the behavior of single crystals exhibiting a nearly carrier-independent μ of ~300 $cm^2V^{-1}s^{-1}$ (*40*).

Finding a suitable substrate to grow BLSO thin films remains as one of major challenges. An ideal substrate would be the insulating $BaSnO_3$ single crystal itself, as its lattice constant matches well with those of BLSO within 0.08 % (*82*). However, it was found that $BaSnO_3$ single crystals grown by the Cu_2O flux usually became oxygen deficient to produce n-type carriers of ~10^{19} cm^{-3} (*82*). Moreover, the crystals grown by the PbO-based flux contained considerable amount of Pb impurities to reduce intrinsic mobilitiy (*83*). Alternative efforts to grow $BaSnO_3$ single crystals with an optical mirror furnace have so far failed due to high evaporation and decomposition of constituent elements.

In this chapter, the author will introduce the successful growth of highly insulating $BaSnO_3$ single crystals with lateral areas close to ~3 × 3 mm^2. In addition, the author will show the evidences of the reduced free carriers in $BaSnO_3$ single crystals based on the optical transmittance, Raman shifts, and Hall effsects. Also, the possible mechanisms of the free carrier reduction will be described.

3.2 Structural properties

Figure 3.1 shows the $BaSnO_3$ single crystals grown in variation of $KClO_4$ molar ratio ($BaSnO_3$: CuO+Cu_2O : $KClO_4$ = 1 : 50 : *y*, *y* = 0, 0.5, 0.6, 1.0, 1.5, 2.0, and 3.0). It was clearly seen that the color of $BaSnO_3$ single crystals became more transparent by putting more $KClO_4$. The x-ray powder diffraction clearly indicated that $BaSnO_3$ single crystals had a single phase of the cubic perovskite structure without detectable impurity phases regardless of the presence of $KClO_4$ in the flux as shown in Fig. 3.2(a). By executing Rietveld refinement on the acquired data, the lattice constants were extracted to be identically $a = b = c = 4.116$ Å .

Figure 3.1 The photograph of the grown crystals with a different *y* (0.0 – 3.0) in the flux. Although the crystals are mostly transparent, its color at the surface systematically changed from bluish to yellowish tone with the increase of the *y*.

X-ray θ–2θ scan on the flat surface of the grown $BaSnO_3$(y=2.0) exhibited only (00l) peaks with the out-of-plane lattice constant (c) of ~4.116 Å, confirming good alignment of the {001} plane (Fig. 3.2(b)). The inset of Fig. 3.2(b) shows the rocking curve measured at the 2θ angle of (002) Bragg peak of $BaSnO_3$(y=2.0). Upon fitting with the pseudo-Voigt function, quite a small, full-width-at-half-maximum (FWHM) of 0.022° was obtained, proving high degree of crystallinity.

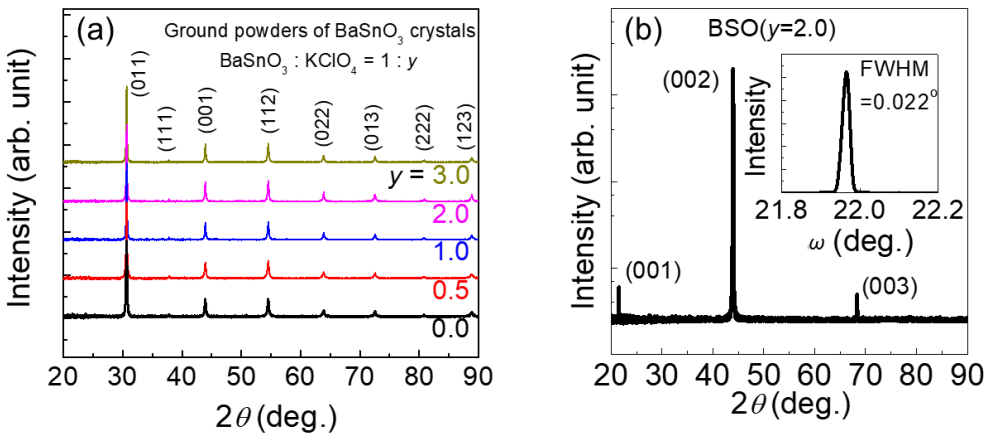

Figure 3.2 (a) X-ray θ-2θ scan results of ground powders of $BaSnO_3$ (y=0.0, 0.5, 1.0, 2.0, and 3.0) single crystals grown by the flux method, which uses a mixture of cupric oxides and $KClO_4$ as a flux with a molar ratio of $BaSnO_3$: CuO : Cu_2O : $KClO_4$ is 1 : 22.4 : 27.6 : y ($0.0 \leq y \leq 3.0$). (b) The X-ray θ-2θ profile of the $BaSnO_3$(y=2.0). The inset shows the rocking curve of the (002) peak.

3.3 Electrical properties

A dramatic change in the electrical transport properties appeared by the addition of $KClO_4$. The electrical transport result was plotted in Fig. 3.3 for the case of different molar ratio of $KClO_4$ to $BaSnO_3$. There were two groups by their electrical tendency, $BaSnO_3$ crystals with y = 0, 0.5, and 0.6 showed a degenerately doped semiconducting behavior and others with y = 0.75, 1.0, 2.0, and 3.0 showed an insulating behavior. Between y = 0.6 and y

= 0.75, the room temperature resistivity differs by an order of 11. A comparable change was observed in the case of $SrTiO_{3-\delta}$ which went through heat treatment under low oxygen partial pressure (*84*). The resistivity changed about an order of 11 at room temperature. Thus, in comparison with previous reports, the grown insulating $BaSnO_3$ single crystals showed superior insulating behavior enough to use an insulating substrate.

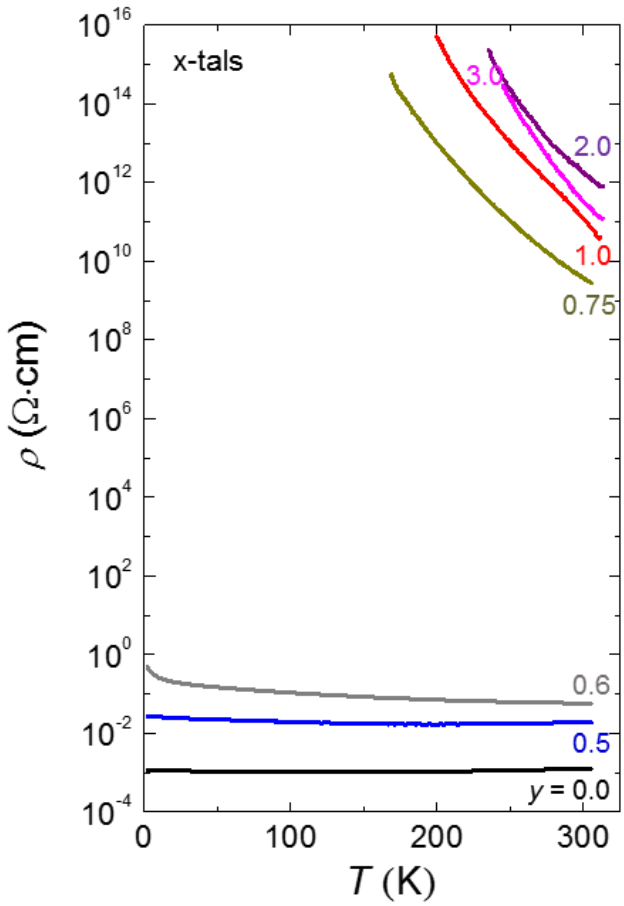

Figure 3.3 Temperature-dependent electrical resistivity ρ of the grown $BaSnO_3$ single crystals. The $BaSnO_3$ crystals with y = 0.0, 0.5, and 0.6 exhibited a degenerately doped semiconducting (or metallic) behavior while those with y = 0.75, 1.0, 2.0, and 3.0 exhibited an insulating behavior. Between y = 0.6 and 0.75, the room temperature ρ differs by 5×10^{10}, indicating there is a percolative transition.

3.4 Optical properties

From the near-IR to UV transmission results, we extracted the absorption coefficient by using the Kramers-Kronig constrained variational dielectric fitting. Figure 3.4 shows the resultant absorption coefficient *vs.* wavenumber plot of the $BaSnO_3$ single crystals (y = 0 and 1.5). The absorption in y = 0 occurs in a wide range below 10000 cm^{-1}, indicating the presence of free carriers. Meanwhile, y = 1.5 single crystals do not show any significant absorption in the same region which means the carrier concentration have been significantly reduced.

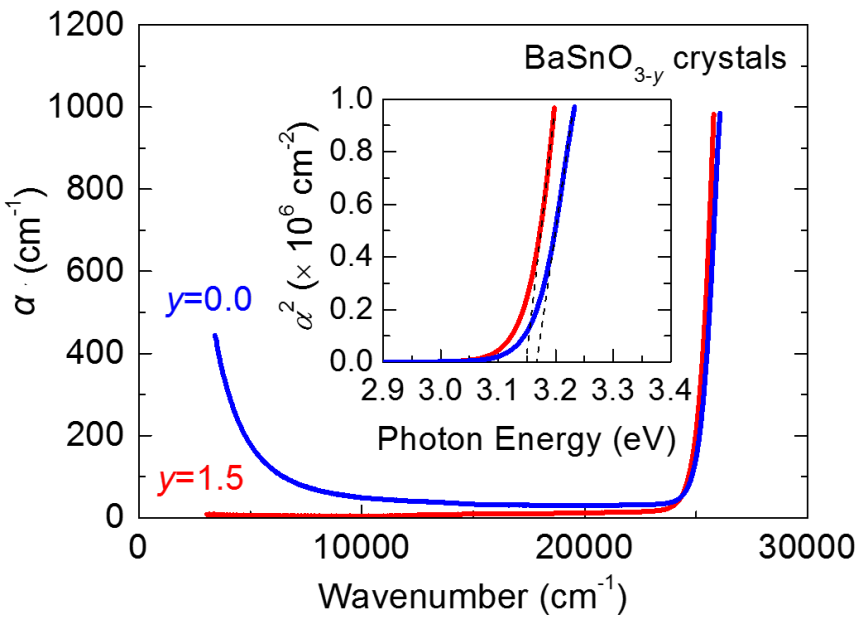

Figure 3.4 Absorption coefficient versus wavenumber in room temperature. The inset shows α^2 versus photon energy to extract the optical band gap.

At the visible light and UV region, we can extract the optical band gap. Even though band calculation suggests that $BaSnO_3$ has an indirect band gap, due to the optical selection rule, direct band gap nature is more strongly observed. From the α^2 *vs.* photon energy plot

in the inset of Fig. 3.4, the direct optical gap was extracted by applying a linear extrapolation. The direct optical gap of $y = 0$ and $y = 1.5$ crystals were estimated to be 3.17 eV and 3.15 eV, respectively. Since the $BaSnO_3$($y = 0$) crystals has a carrier concentration of ~10^{19} cm^{-3} and shows a metallic resistivity curve, the energy difference of 20 meV can be explained by Burstein-Moss shift. $\Delta E = h^2(3n/\pi)^{2/3}/(8m^*)$, where ΔE was the difference between the Fermi level and the conduction band minimum and m^* presented the electron effective mass. According to our results of ΔE *vs.* n in $(Ba,La)SnO_{3-\delta}$ and $BaSnO_3$ single crystals (*82*), the energy shift of ~20 meV corresponded to n = ~10^{19} cm^{-3}. Therefore, the optical transmission results indicated that n was effectively reduced in $BaSnO_3$ by the addition of $KClO_4$ during crystal growth.

3.5 Origin of conductivity variations

Initially, we presumed that the insulating behavior of $BaSnO_3$ single crystals with $y >$ 0.6 attributed to the reduced V_O. However, it was not decisive yet because we cannot rule out the carrier compensation scenario. The EPMA result revealed that the $BaSnO_3$ single crystals contained detectable amount of K impurities as shown in Fig. 3.5. When the K impurities present at the Ba-site, they can act as acceptor impurities because their ionic valence is K^{1+}. In the case of y=2.0, the calculated K ratio at Ba-site is ~ 0.1 mol%, i.e., the density of K impurities is ~1.4×10^{19} cm^{-3}. This density of K impurities is almost comparable to the carrier density of $BaSnO_3$ single crystal with $y = 0.0$, indicating that the reduction of electron carriers also originated from the carrier compensation by K impurities.

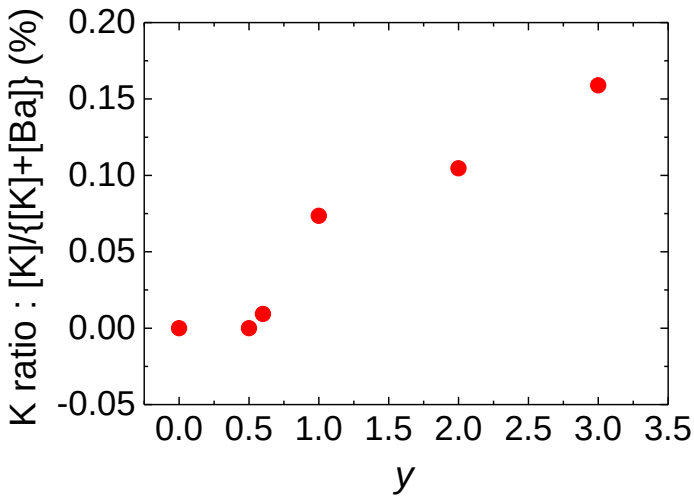

Figure 3.5 The molar ratio of K impurities in $BaSnO_3$ single crystals.

To investigate further, we performed the Hall effects of the some $BaSnO_3$ single crystals at room temperature. Figure 3.6 shows the μ *vs.* n of the $BaSnO_3$ single crystals (y = 0, 0.5, and 0.6). We observed that n slightly decreased as as y increasing while μ decreased clearly. If n only decreased while μ did not decrease, we concluded that the reduced n might originate mainly from the reduced oxygen vacnacies. However, the decreased μ indicated that there existed additional carrier scattering sources by putting more $KClO_4$. According to the EPMA results, we attributed the additional carrier scattering sources to the increased density of K impurities. This interpretation indicated again that we could not neglect the carrier compensation senario by K impurities when we consider the origin of the insulating $BaSnO_3$ single crystals.

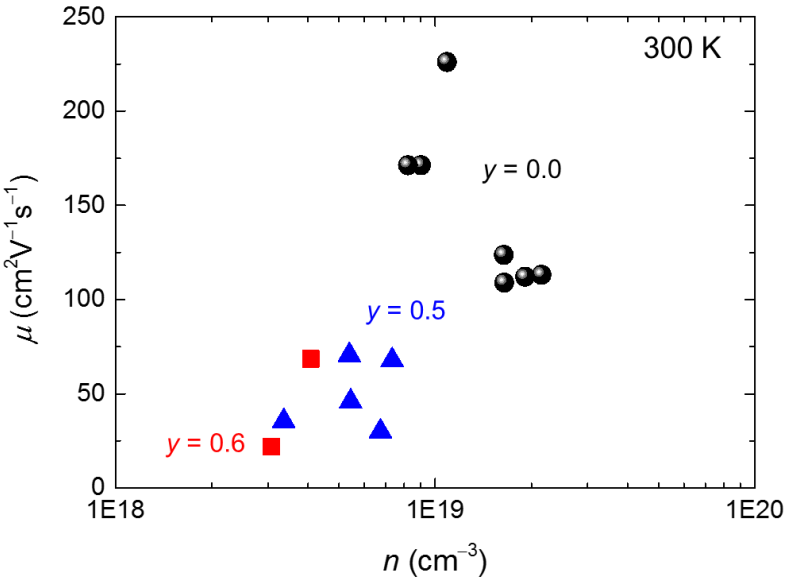

Figure 3.6 μ versus n of $BaSnO_{3-\delta}$ single crystals at room temperatures.

We find that carrier doping in $BaSnO_3$ produces significant local lattice distortion as evidenced by Raman spectroscopy. Figure 3.7 shows the Raman spectra of metallic $BaSnO_3$ (y = 0.0 – 0.6) and highly insulating $BaSnO_3$ (y = 0.67 – 0.75) singe crystals. All the single crystals turned out to show very similar X-ray scattering profiles. We verified from the refinement that all the scattering data could be well fitted by the cubic perovskite structure. In an ideal cubic perovskite, the first order Raman modes should be absent by symmetry. Consistently, we found almost no Raman active mode in the highly insulating $BaSnO_3$ single crystal except a small intensity at 833 cm^{-1}, which might be a local vibration mode related to intrinsic defects, e.g., cation vacancies. In sharp contrast, metallic $BaSnO_3$ (y = 0.0 – 0.6) single crystals with n ~≥ 1.0×10^{19} cm^{-3}, respectively, exhibited quite strong Raman modes at ~138 cm^{-1}, ~250 – 350 cm^{-1}, and ~615 – 650 cm^{-1}. Moreover, Raman spectra of $BaSnO_3$ (y = 0.0 – 0.5) single crystals are quite similar. This result implies the presence of electron carriers in the $BaSnO_3$ system produces local lattice distortion, which

possibly breaks the cubic symmetry locally. One possible scenario is that occupation of the antibonding state via electron doping can induce the expansion of the Sn-O bond length, presumably involving the breathing mode distortion. This expansion in the bond length will likely induce reduction of the Sn-O-Sn bonding angle from an ideal 180 °, which then results in local symmetry lowering toward the orthorhombic structure. The main modes observed in the Raman spectra in Fig. 3.7 are likely to be stretching (~615 – 650 cm^{-1}), bending (~250 – 350 cm^{-1}) and external (~138 cm^{-1}) phonon modes expected of SnO_6 octahedra in the lower crystal symmetry than cubic structure, i.e., the orthorhombic or tetragonal symmetry (*85*, *86*). Our results naturally imply that electron-phonon coupling in doped-$BaSnO_3$ can be significantly large.

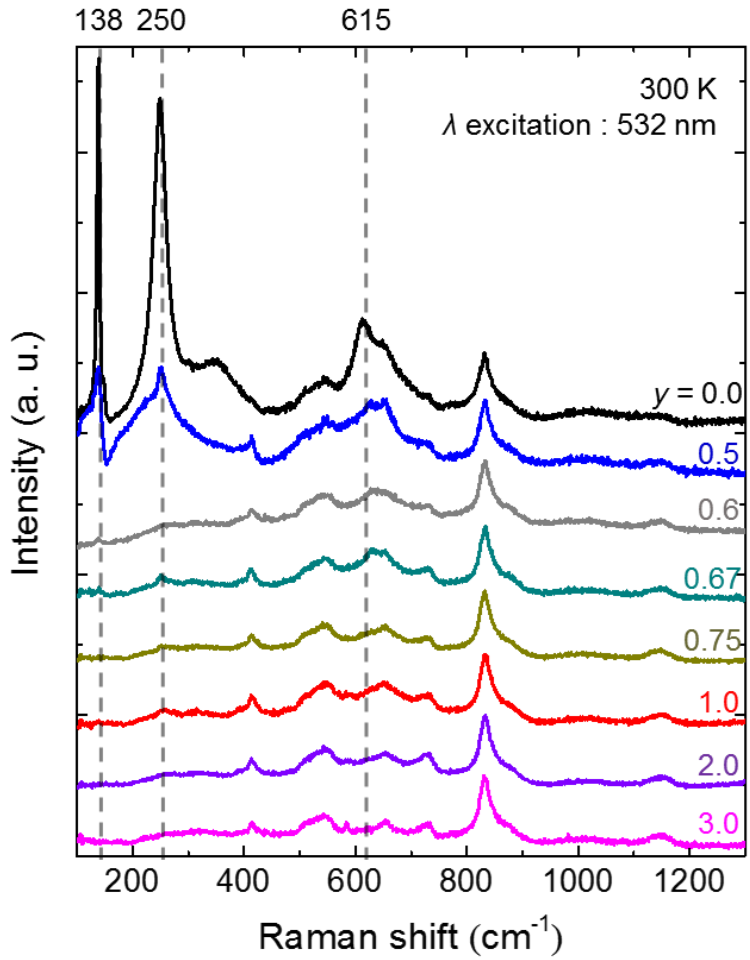

Figure 3.7 Raman spectra of $BaSnO_3$ (y = 0.0 – 3.0) single crystals, providing evidence that the presence of electron carriers produces local lattice distortions, thereby locally breaking the cubic symmetry

Chapter 4 Achieving highest electron mobility in epitaxial (Ba,La)SnO_3 films grown by pulsed laser deposition

In this chapter, the author will introduce the successful growth of epitaxial BLSO films on highly insulating $BaSnO_3$(001) substrates [BLSO/$BaSnO_3$(001)] by the PLD method. The μ at room temperature was as high as 102 $cm^2V^{-1}s^{-1}$ at n = 1.0 × 10^{20} cm^{-3}. Recent efforts to grow insulating substrates and films grown by molecular beam epitaxy (MBE) will be summarized. In addition, the author will discuss the operation of field effect transistor based on $BaSnO_3$ channel layer on $BaSnO_3$(001) substrates.

4.1 Free carrier scatterings and mobilities in degenerate semiconductors

As this chapter is focused on the mobility behavior due to the ionized dopants (e.g., V_O or La^{3+} dopants to Ba^{2+} site), the author will briefly explain free carrier scatterings mainly due to the ionzied impurity scatterings. In a semiconductor under the influence of external forces, transport coefficients can be derived from the Boltzmann transport equation using the relaxation time approximation. An applied electric field or temperature is effective on the electrons to change the distribution function of electrons from its equilibrium condition. The Fermi-Dirac distribution function can describe the distribution of electrons in a semiconductor under equilibrium conditions. However, the electron distribution function may change from the equilibrium distribution function under the influenec of external fields, e.g., electric field or magnetic field.

Using the relaxation time approximtion, an analytical expression for the Boltzmann transport equation can be derived. It is assumed that all the collision processes are elastic and could be treated in terms of a relaxation time in a relaxation time approximation. This apporoximation could be allowded to obatin analytical expressions for different transport coefficients. In order to understand physical insights concerning the collision terms and the validity of the relaxation time approximation, various scattering mechanisms associated with the collision term in the Boltzmann equation have been discussed with several important scattering mechanisms, e.g., acoustic phonon and optical phonon scatterings, ionized impurity scattering, and neutral impurity scattering (*87*).

As the charge carriers could be scatterd by several defects, i.e., ionized impurities, phonons, and dislocations, the scattering mechanisms could determine the transport properties of semiconductors. In general, the electrical conductivity of an n-type semiconductor can be described in terms of the electron mobility and electron concentration by

$$\sigma = nq\mu, \qquad \text{Equation 4.1}$$

where *n, q, and* μ represent the electron concentration, the electronic charge, and the electron mobility. μ can be defined by

$$\mu = \frac{q\langle\tau\rangle}{m^*}, \qquad \text{Equation 4.2}$$

where $<\tau>$ is the average relaxation time. Thus, μ is proportional to the average relaxation time, which is directly related to the scattering mechanisms.

Based on the relaxation time approximation (*87*), one obtains

$$\left.\frac{\partial f}{\partial t}\right|_{c} = -\frac{f - f_0}{\tau}, \qquad \text{Equation 4.3}$$

where f and f_0 represent the nonequilibrium distribution function and the equilibrium Fermi-Dirac distribution function. For the eleastic scattering case, Equation 4.3 can be defined by

$$-\left.\frac{\partial f_{k'}}{\partial t}\right|_{c} = \sum_{k'}\left[P_{kk'} f_{k'}\left(1 - f_k\right) - P_{k'k} f_k\left(1 - f_{k'}\right)\right], \qquad \text{Equation 4.4}$$

where $P_{kk'}$ and $P_{k'k}$ represent the rate of transition probability from the final state k' to the initial state k and the rate of transition probability from the k-state to the k'-state. k' and k are the electron distribution function in the k'-state and the elctron distribution function in the k-state. The net transition rates from the k- to the k' state assummed over all the final states k' is expressed in the right-hand side of Equation 4.4.

As the qauntum states in the band can be treted as a quasicontinumm, it is possible to replace the summation in Equation 4.4 by an integral, which is given by

$$\begin{aligned} -\left.\frac{\partial f_{k'}}{\partial t}\right|_{c} &= \frac{N\Omega}{\left(2\pi\right)^3}\int\left[P_{kk'} f_{k'}\left(1 - f_k\right) - P_{k'k} f_k\left(1 - f_{k'}\right)\right]d^3k' \\ &= \frac{N\Omega}{\left(2\pi\right)^3}\int P_{kk'}\left(f_{k'} - f_k\right)d^3k' \end{aligned}, \qquad \text{Equation 4.5}$$

where N and Ω are the total number of unit cells and the volume of the unit cell. Note that $P_{kk'}$ is assumed equal to $P_{k'k}$. In order to analytically solve Equation 4.5, one can use the small-pertutbation, resultung in the nonequilibrium distribution function $f(k,r)$ could be expressed in terms of the equilibrium distribution function f_k^0 and a first-order perturbing function, which is given by

$$\begin{aligned} f_k &= f_k^0 + f_k^1 + \cdots \\ f_{k'} &= f_{k'}^0 + f_{k'}^1 + \cdots \end{aligned} . \qquad \text{Equation 4.6}$$

If the scattering is elastic, Equation 4.5 can be simplified to

$$-\left.\frac{\partial f_{k'}}{\partial t}\right|_c = \frac{f_{k'}^1}{\tau} = \frac{N\Omega}{(2\pi)^3}\int P_{kk'}\left(f_{k'}^1 - f_k^1\right)d^3k' . \qquad \text{Equation 4.7}$$

Therefore, one can get the inverse relaxation time, which can be written as

$$\frac{1}{\tau} = \frac{N\Omega}{(2\pi)^3}\int P_{kk'}\left(1 - \frac{f_k^1}{f_{k'}^1}\right)d^3k' . \qquad \text{Equation 4.8}$$

Under the isotropic scattering process, Equation 4.8 can be written as

$$\frac{1}{\tau} = \frac{N\Omega}{(2\pi)^3}\int P_{kk'}\left(1 - \cos\theta'\right)d^3k' , \qquad \text{Equation 4.9}$$

indicating that scattering rate only depends on the angle between *k*- and *k′*- states and the rate of transition probability. Thus, one can derive the relaxation time for a speific scattering process by determining the rate of transition probability and the differential scattering cross-section.

In order to derive the rate of transition probability $P_{kk'}$, one can start to use the one-electron time-independent Schrödinger equation, which can be written as

$$\begin{aligned} &H_0\phi_k(r) = E_k\phi_k(r), \\ &H_0 = -\frac{\hbar^2\nabla^2}{2m^*} + V(r), \\ &\phi_k(r) = u_k(r)\mathrm{e}^{ikr} \end{aligned}, \qquad \text{Equation 4.10}$$

where H_0, $\phi_k(r)$, and $u_k(r)$ are the unperturbed Hamiltonian, the initial unperturbed electron wave function, and the Bloch function. The slightly perturbed Hamiltonian can be written as

$$H = H_0 + H', \qquad \text{Equation 4.11}$$

where H_0 and H' are the unperturbed Hamiltonian and the first-order correction. Moreover, under the perturbation, the time-dependent Schrödinger equation can be written as

$$\begin{aligned} &H\psi_k(r,t) = -i\hbar\frac{\partial\psi_k(r,t)}{\partial t} \\ &\psi_k(r,t) = \sum_k a_k(t)\mathrm{e}^{-iE_kt/\hbar}\phi_k(r) \end{aligned}, \qquad \text{Equation 4.12}$$

where $a_k(t)$ and $\phi_k(r)$ are the time-dependent amplitude function and the unperturbed electron wave function. Based on the time-depndent perturbation theory, the amplitude function can be used to express the transition probability per unit time from the k- to the k'-state, which is given by

$$P_{kk'}(t) = \frac{\left|a_{k'}(t)\right|^2}{t}. \qquad \text{Equation 4.13}$$

Based on the orthogonal properties of electron wave functions and some calculations to Equation 4.12, the rate of transition probability of Equation 4.13 can be written as

$$P_{kk'}(t) = \frac{\left|a_{k'}(t)\right|^2}{t} = \frac{2\pi}{\hbar}\left|H_{kk'}\right|^2 \delta\left(E_{k'} - E_k\right), \quad \text{with } H_{kk'} = \left\langle k'\middle|H'\middle|k\right\rangle = \frac{1}{(N\Omega)}\int_{N\Omega} \phi_{k'}^* H' \phi_k d^3r \quad \text{Equation 4.14}$$

where $\delta(E_{k'}-E_k)$ and $H_{kk'}$ are the Dirac delta function and the matrix element. It is noted that above matrix element will be finite if the Fermi golden rule is satisfied (*88*).

Now consider the relaxation time τ, which will be simplified by use of a differential scattering cross-section $\sigma(\theta',\phi')$. Baed on the isotropic scattering process, a differential scattering cross-section can be written as

$$\sigma\left(\theta',\phi'\right) = \frac{\frac{N\Omega}{(2\pi)^3} P_{kk'} \frac{d^3k'}{d\omega}}{\frac{v_k}{N\Omega}} = \frac{(N\Omega)^2 P_{kk'} d^3k'}{(2\pi)^3 v_k \sin\theta' d\theta' d\phi'} \quad \text{Equation 4.15}$$

where v_k, $N\Omega$, and $d\omega$ are the initial particle velocity, the volume of the crystal, and the solid angle between the incident wave vector and the scattered wave vector. Under iotropic elastic scattering, by substrituting Equation 4.14 into Equation 4.15, a differential scattering cross-section can be given by

$$\sigma\left(\theta'\right) = \frac{(N\Omega)^2 k'^2 \left|H_{kk'}\right|^2}{\left(2\pi\hbar v_{k'}\right)^2}. \quad \text{Equation 4.16}$$

For the isotropic elastic scattering process, the toal scattering crosse-section (σ_T) can be expressed by

$$\sigma_{\mathrm{T}} = 2\pi\int_0^{\pi}\sigma(\theta')(1-\cos\theta')\sin\theta' d\theta' \,. \qquad \text{Equation 4.17}$$

As the scattering rate τ^1 can be written as

$$\frac{1}{\tau} = N_{\mathrm{T}}\sigma_{\mathrm{T}}v_{\mathrm{th}} \,. \qquad \text{Equation 4.18}$$

where, N_{T} and v_{th} are the density of total scattering center and the mean thermal velocity, one can use Equation 4.17 and Equation 4.18 to derive the scattering rates and carrier mobilities, which will be affected by ionized impurities, the opitcal and acoustic phonons, neutral impurities, and dislocations.

Now consider scattering of electrons by ionized donor impurities. As it could be an elastic scattering, one can utilize the relaxation time approximation given by Equation 4.18. First, the potential of the inozed donor impurities can be approximated by

$$V(r) = \frac{qZ}{4\pi\varepsilon_0\varepsilon_{\mathrm{r}}r} \,, \qquad \text{Equation 4.19}$$

where Z is the charge number of ionized dopants (i.e., Z = +1 for La^{3+} and Z = +2 for V_O). As there is Coulomb screening effect due to electrons from the donor impurities, it is essential to use screening Coulomb potential for deriving the mobility from the ionized impurity scattering, which can be expressed by

$$V'(r) = \frac{qZ\,\mathrm{e}^{-r/\lambda_D}}{4\pi\varepsilon_0\varepsilon_{\mathrm{r}}r}, \qquad \lambda_D = \sqrt{\frac{\varepsilon_0\varepsilon_{\mathrm{r}}k_B T}{q^2 n_0}} \,. \qquad \text{Equation 4.20}$$

where λ_D is the Debye screen length.

To derive the matix element for ionized impurity scattering, the Brooks-Herring (B-H) model (*89*) will be used. The perturbing Hamiltonian from the screening Coulomb potential can be written as

$$H' = qV'(r) = \frac{q^2 Z\, \mathrm{e}^{-r/\lambda_D}}{4\pi\varepsilon_0\varepsilon_r r}\,. \qquad \text{Equation 4.21}$$

By use of Bloch wave functions, which can be written as

$$\phi_k(r) = \frac{1}{\sqrt{N\Omega}} u_k(r)\mathrm{e}^{ik\cdot r}, \qquad \text{Equation 4.22}$$

and Equation 4.21, the matrix element in Equation 4.14 can be expressed by

$$\begin{aligned} H_{kk'} &= \frac{1}{N\Omega}\int \mathrm{e}^{-ik'\cdot r}\left|\frac{q^2 Z\, \mathrm{e}^{-r/\lambda_D}}{4\pi\varepsilon_0\varepsilon_r r}\right|\mathrm{e}^{ik\cdot r}\, d^3 r \\ &= \frac{q^2 Z\lambda_D^2}{N\Omega\varepsilon_0\varepsilon_r\left(1+K^2\lambda_D^2\right)} \end{aligned}, \qquad \text{Equation 4.23}$$

where d^3r is $2\pi r^2 \sin\theta r\, d\theta r\, dr$ and K is the reciprocal lattice vector, can be expressed by

$$K = k' - k = 2|k|\sin\left(\frac{\theta'}{2}\right). \qquad \text{Equation 4.24}$$

By inserting Equation 4.23 into Equation 4.16, the differential scattering cross-section can be written as

$$\sigma(\theta') = \frac{\left(q^2 m^* Z \lambda_D^2\right)^2}{\left(2\pi\hbar^2 \varepsilon_0 \varepsilon_r\right)^2 \left(1 + K^2 \lambda_D^2\right)^2} = \frac{4Z^2 \lambda_D^4}{a_B^2 \left(1 + K^2 \lambda_D^2\right)^2}, \qquad \text{Equation 4.25}$$
$$a_B = \frac{4\pi\varepsilon_0 \varepsilon_r \hbar^2}{m^* q^2}$$

where a_B is the Bohr radius for the ground state of the impurity atom. The scattering rate for the ionized impurity scattering is obtained by substituting Equation 4.25 into Equation 4.18, which can be expressed by

$$\frac{1}{\tau_I} = 2\pi N_I v \int_0^\pi \frac{4\lambda_D^4 Z^2 (1 - \cos\theta') \sin\theta' d\theta'}{a_B^2 \left[1 + 4\lambda_D^4 k^2 \sin^2(\theta'/2)\right]^2}$$
$$= 2\pi N_I v \left(\frac{\lambda_D^4 Z^2}{a_B^2}\right)\left(\frac{1}{k\lambda_D}\right)^4 F_{ii}(\xi_d), \qquad \text{Equation 4.26}$$
$$\text{with } \xi_d = 2|k|\lambda_D$$

where F_{ii} is the screening function which can be written as

$$F_{ii}(\xi_d) = \ln(1 + \xi_d) - \frac{\xi_d}{1 + \xi_d}, \qquad \text{Equation 4.27}$$

Equation 4.26 is known as the Brooks-Herring formula for ionized impurity scattering. By using the relation of $E=h^2k^2/(8\pi^2m^*)$, the scattering rate will be given by

$$\frac{1}{\tau_I} = 2\pi N_I \sqrt{\frac{2E}{m^*}} \left(\frac{q^2 Z}{4\pi\varepsilon_0 \varepsilon_r E}\right)^2 F_{ii}(\xi_d) = \frac{Z^2 q^4 N_I F_{ii}(\xi_d)}{16\pi \left(2m^*\right)^{1/2} \left(\varepsilon_0 \varepsilon_r\right)^2 E^{3/2}}. \qquad \text{Equation 4.28}$$

This equation indicates that the relaxation time is proportional to $E^{3/2}$ and the temperature dependence is quite small. Based on the Maxwell-Boltzmann statics, the average relaxation can be expressed by

$$\langle \tau \rangle = \frac{\int_0^\infty \tau E^{3/2} \mathrm{e}^{-E/k_B T}\, dE}{\int_0^\infty E^{3/2} \mathrm{e}^{-E/k_B T}\, dE}. \qquad \text{Equation 4.29}$$

Thus, one can obtain the electron mobility limited by the ionzed impurity scattering can be written as

$$\mu_I = \frac{q\langle \tau_I \rangle}{m^*} = \frac{64\sqrt{\pi}\varepsilon_0^2 \varepsilon_r^2 (2k_B T)^{3/2}}{N_I q^3 \sqrt{m^*} Z^2 F_{ii}(\xi_d)}, \qquad \text{Equation 4.30}$$

indicating that the the electron mobility governed by the ionized impurity in the non-degenerate semiconductor is proprotional to $T^{3/2}$.

On the other hand, in order to understand the ionized-impurity scattering in the degenerate semiconductors, Thomas-Fermi approximation should be considered (*88*), assuming the constant chemical potential in the system. If one use a prabolic band and the screened Coulomb potential, the scattering rate will be given by

$$\begin{aligned} \frac{1}{\tau_1} &= 2\pi N_I v F \left(\frac{\pi m^* q^2 Z}{\varepsilon_0 \varepsilon_r h^2 |k_F|^2} \right)^2 F_{ii}(\xi_d) \\ &= \frac{Z^2 q^4 N_I F_{ii}(\xi_d)}{16\pi} (2m^*)^{1/2} (\varepsilon_0 \varepsilon_r)^2 E_F^{3/2} \end{aligned}, \qquad \text{Equation 4.31}$$

where v_F and E_F are the Fermi velocity and Fermi level. Thus the electron mobility governed by the ionized impurity scattering in the degenerate semiconductors can be written as

$$\mu_I = \frac{q\langle\tau_I\rangle}{m^*} = \frac{3\varepsilon_0^2\varepsilon_r^2 h^3 n}{m^* Z^2 q^3 N_I F_{ii}(\xi_d)}, \qquad \text{Equation 4.32}$$

indicating the temperatire-independent electron moblity in the degenerate semiconductors (*30, 90*). To derive the mobilities from other defects, e.g., the neutral impurities, dislocations, acoustical and optical phonon scatterings, the readears can refer to the following references (*87, 91*).

4.2 Structural properties of (Ba,La)SnO_3/$BaSnO_3$(001) films

Using the grown single crystals as a substrate in combination with fine polishing, we could grow epitaxial BLSO films on $BaSnO_3$(001) substrates (BLSO/ $BaSnO_3$) to find enhanced μ in a broad doping range ($6.8 \times 10^{19} \leq n \leq 5.3 \times 10^{20}$ cm^{-3}) at room temperature as compared with those grown on $SrTiO_3$(001) substrates. Figures 4.1(a) and (b) show AFM images of BLSO/ $BaSnO_3$ (x=0.01 and 0.04) thin films. Their maximum height difference and rms roughness were found to be about ~0.9 nm and ~0.24 – 0.27 nm, respectively, demonstrating that smooth films could be grown on $BaSnO_3$(001) substrates. The θ–2θ scans of BLSO/$BaSnO_3$ (x = 0.00, 0.01 and 0.04) (Fig. 4.1(c)) showed that they were grown along (00l) directions without undesired phases. The inset shows expanded 2θ profiles around (002) Bragg reflection of the films, showing systematic shifts toward lower angles as x is increased. This observation implies that the out-of-plane lattice constant in x = 0.00 and 0.01 films, which is close to that of $BaSnO_3$(001) substrates, is expanded as x is increased from 0.00 and 0.01 to 0.04. Figure 4.1(d) shows rocking curves measured at the center of (002) Bragg peaks of three films (x = 0.00, 0.01, and 0.04). We find that the rocking curves of BSO/$BaSnO_3$ and BLSO/$BaSnO_3$ (x=0.01) films are screened by the

contribution of substrates or exhibit only a shoulder-like feature, respectively, making it difficult to obtain FWHM of those films. However, the rocking curve of the BLSO (x=0.04) film is well separated from that of substrates so that FWHM could be obtained to be as small as 0.029 °, confirming the good crystallinity. In comparison, we recall in previous reports that FWHMs in the ω-scans of BLSO films grown on $SrTiO_3$(001) or MgO(001) were 0.09 – 1.0 ° (*25, 73, 75*). Those results clearly indicate that thin BLSO films grown on the $BaSnO_3$ substrates have better crystallinity than those grown on $SrTiO_3$(001) or MgO(001).

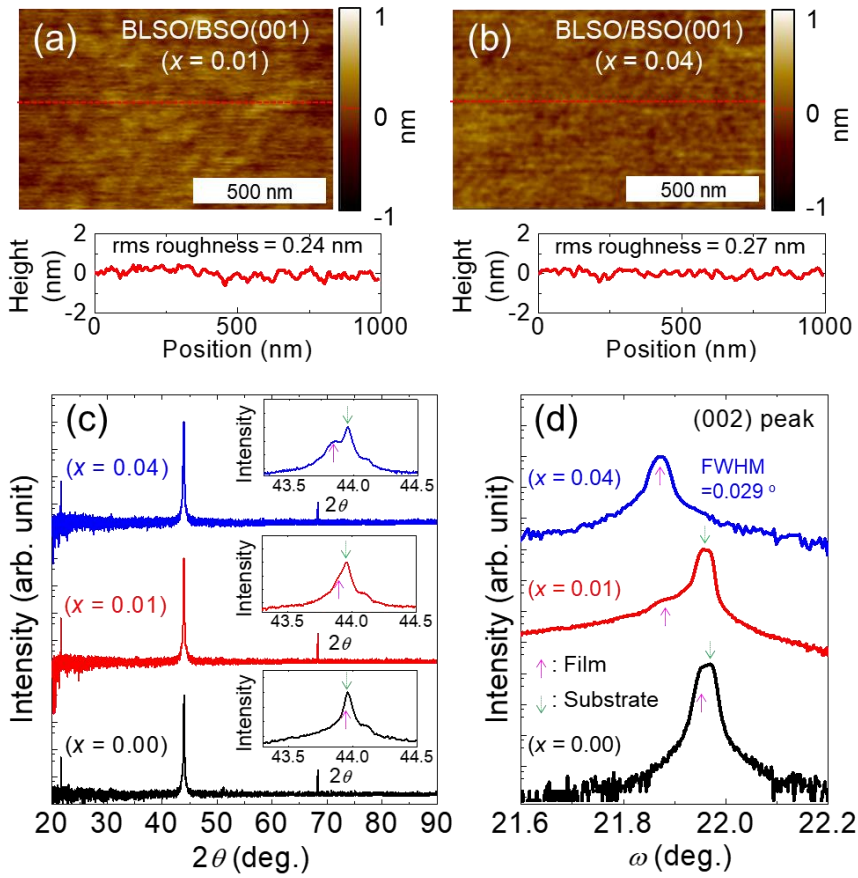

Figure 4.1 (a) and (b) show the surface morphology and heights of the $Ba_{1-x}La_xSnO_3$ (x = 0.01 and 0.04) films, respectively. Bottom panels show the height profiles along the dotted solid lines. (c) The θ-2θ scan results of the $Ba_{1-x}La_xSnO_3$ films. The inset shows the θ-2θ scan near (002) peaks. Film peaks are indicated with the solid arrows, while the peaks related with the $BaSnO_3$ substrate are shown as dotted arrows. (d) The rocking curves measured at the (002) peaks of the films.

To better understand structural evolutions with La doping, we investigated X-ray RSM. Figure 4.2(a) displays (103) reflection of the $BaSnO_3$(001) substrate, forming only one spot in the (Q_x, Q_z) plane. Calculations of in-plane lattice constant (a) and c from the spot position resulted in a nearly same value of 4.116 Å, being consistent with the cubic symmetry of $BaSnO_3$(001) substrates. Figure 4.2(b) shows RSM of the BLSO/$BaSnO_3$

(x=0.04), revealing that the Q_x of the film spot is nearly same as that of the $BaSnO_3$(001) substrate while the Q_z of the film spot is clearly smaller than that of the $BaSnO_3$(001) substrate. From this, it is concluded that the BLSO (x=0.04) film has a = ~4.116 Å, almost same as the substrate, while c = 4.126 Å of the film is increased by + 0.24 % as compared with that of the substrate. This implies that the in-plane of the BLSO (x=0.04) film is subject to compressive strain to have the same a value with the substrate while its c-axis is expanded than that of the substrate to meet the Poisson relation. Note that the BLSO (x = 0.03 and 0.04) polycrystals are known to have generally larger lattice constants (4.1175 – 4.1181 Å) than that of undoped one (4.1151 – 4.1160 Å), according to the literatures (*40, 69*) (*83*). On the other hand, nearly one spot could be identified in the RSM of the BLSO (x=0.01) film (Fig. 4.2(c)), implying that films with low $x \leq 0.01$ have almost same lattice constants with $BaSnO_3$(001) substrates along both in-plane and out-of-plane directions. The present RSM results thus indicate that BLSO films grown on the $BaSnO_3$(001) substrates may have increasing compressive strain as the La doping level is increased. This can be understood because bulk BLSO shows the progressive increase of pseudo-cubic lattice constants with La doping as electron carriers fill up antibonding states of Sn 5*s* character (*40*).

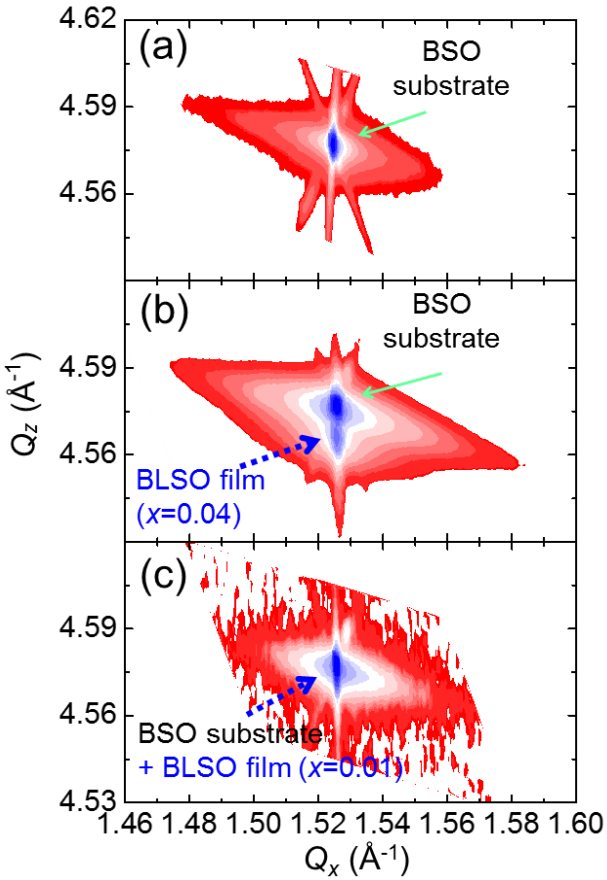

Figure 4.2 Reciprocal space maps of the (103) reflection for the (a) $BaSnO_3$(001) substrate, (b) $Ba_{0.96}La_{0.04}SnO_3/BaSnO_3$(001), and (c) $Ba_{0.99}La_{0.01}SnO_3/BaSnO_3$(001).

Until recently, most reported BLSO films were grown on $SrTiO_3$(001) substrates, whose a_c = 3.905 Å has a large misfit of 5.13 % relative to the lattice constant of $BaSnO_3$(001) (a_c = 4.116 Å). Figures 4.3(a) and (b) show low- and high-magnification cross-sectional transmission electron microscopy (TEM) images, respectively, at the film-substrate interface of $Ba_{0.995}La_{0.005}SnO_3$-$SrTiO_3$(001). Misfit dislocation arrays in the BLSO film with period = ~7.4 – 7.8 nm were found (*76*). These values correspond to the 19–20 layers of {101} planes in the $SrTiO_3$ substrate and to the 18–19 layers of the {101} planes in the BLSO film. Therefore, the main source for the dislocations should be the

$SrTiO_3$(001) substrate, which has a large lattice mismatch with $BaSnO_3$.

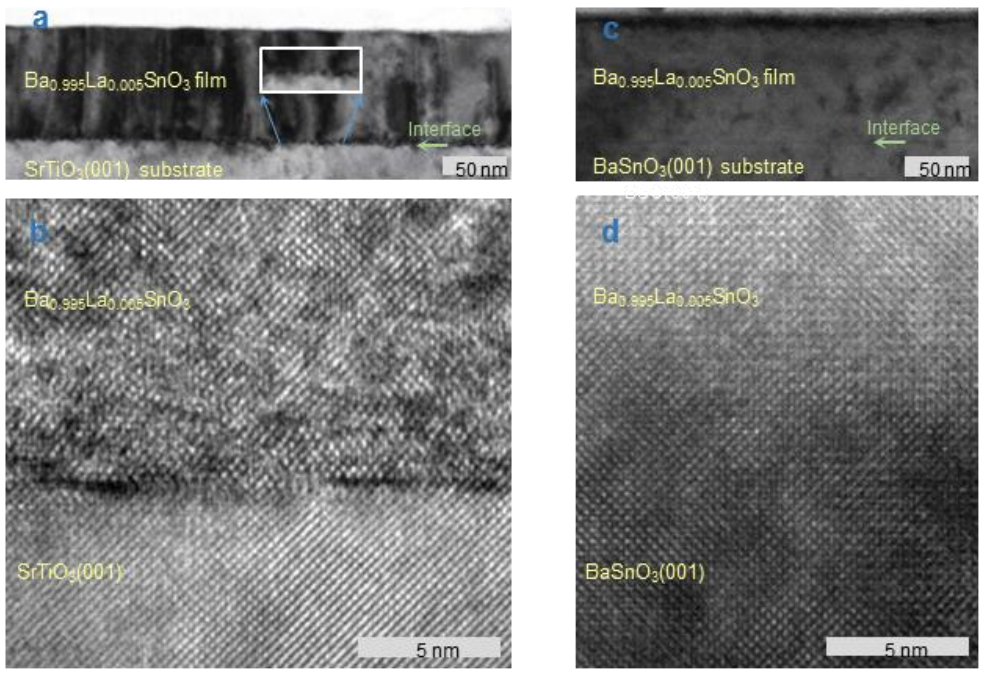

Figure 4.3 TEM images showing film-substrate interfaces. (a) and (b) are low- and high magnification cross-sectional TEM images, respectively, of the $Ba_{0.995}La_{0.005}SnO_3$-$SrTiO_3$(001) interface. (c) and (d) are images of the $Ba_{0.995}La_{0.005}SnO_3$-$BaSnO_3$(001)

Figures 4.3(c) and (d) show cross-sectional TEM images of the BLSO/$BaSnO_3$(001) (x=0.005). We could not find any dislocations or grain boundaries in a bright field image covering a wide area of film cross-section over ~100 × 500 nm^2 (Fig. 4.3(d)). The high-resolution image near the interface also demonstrates that the lattice periodicity of the BLSO film almost perfectly matches that of the $BaSnO_3$(001) substrate; twenty layers of (101) planes in the $BaSnO_3$(001) substrate have the same distance in the BLSO film. With such a good lattice match, we could not distinguish well even the interface between the substrate and the film, supporting that the high quality epitaxial BLSO films are realized on the $BaSnO_3$(001) substrate.

4.3 Electrical properties

Figures 4.4(a) and (b) summarize ρ and μ as a function of n at room temperature in BLSO/$BaSnO_3$ and reported BLSO/$SrTiO_3$(001) (*40*). Red, blue, orange, and magenta circles represent data points from BLSO/$BaSnO_3$(001) grown by sintered $Ba_{1-x}La_xSnO_3$ targets with x = 0.005, 0.01, 0.02, and 0.04, respectively. Although there exist scatterings in data points among films, the measured n (ρ) values of BLSO/$BaSnO_3$(001) are systematically increased (decreased) in proportional to the La-doping level in targets. Moreover, they are close to carrier numbers expected from those targets. An EPMA study on one of BLSO/$BaSnO_3$(001) (x=0.005) also showed that La dopants had small variation over the 10 different spots measured and the averaged value was $x = 0.0061 \pm 0.0011$, being close to the nominal doping level of the target. Figure 4.4(b) shows that the measured μ of BLSO/$BaSnO_3$(001) is ~75 $cm^2V^{-1}s^{-1}$ at a high n regime (~5.0×10^{20} cm^{-3}) and ~80–100 $cm^2V^{-1}s–^1$ in a low n regime ($\leq 1.0 \times 10^{20}$ cm^{-3}). The slightly increasing trend of μ with decrease of n is somewhat similar to the behavior observed in BLSO single crystals, in which ionic scattering due to La^{3+} ions became dominant scattering sources (*25*, *82*). In contrast, BLSO/$SrTiO_3$(001) showed clear μ decreases with the decrease of n due to strong carrier scatterings at grain boundaries and dislocations (*25*, *40*, *81*). Our observation implies that the μ of BLSO thin films on $BaSnO_3$(001) substrates are not dominated by scatterings from dislocations/grain boundaries. Therefore, the enhanced μ values and the nearly n-independent behavior of μ should represent merits of epitaxial BLSO films on $BaSnO_3$(001) substrates with much reduced structural defects without threading dislocations/grain boundaries.

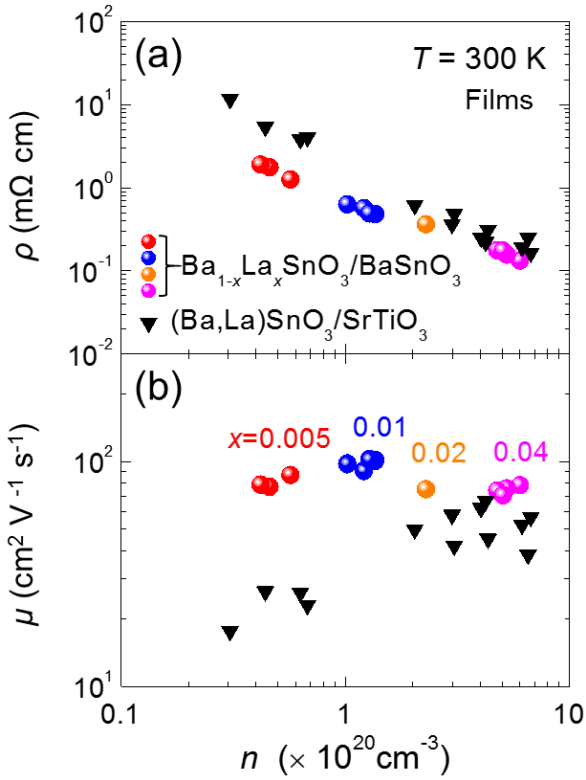

Figure 4.4 Electrical resistivity (ρ) and (b) electron mobility (μ) *vs.* carrier density (n) plots for $Ba_{1-x}La_xSnO_3/BaSnO_3$(001) films (circles).

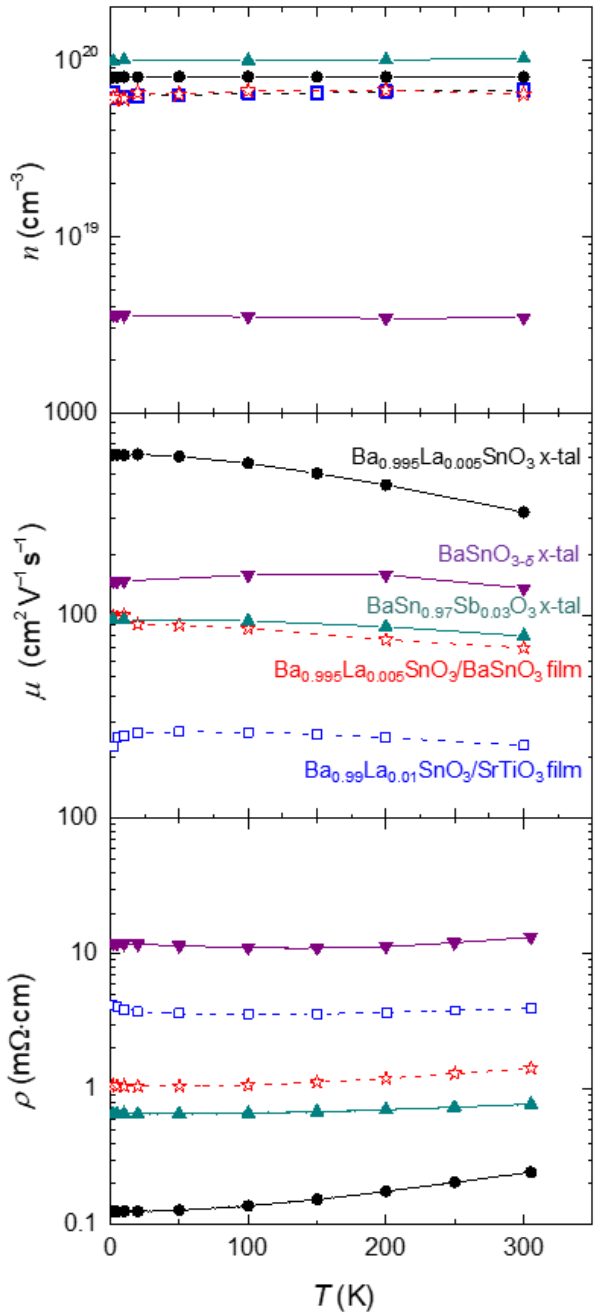

Figure 4.5 Temperature dependent electron carrier concentration n, electron mobility μ, and electrical resistivity ρ for selected $Ba_{0.995}La_{0.005}SnO_3$ (60), $BaSn_{0.097}Sb_{0.03}O_3$ (66), and $BaSnO_{3-\delta}$ (66) single crystals and $Ba_{0.995}La_{0.005}SnO_3/BaSnO_3$(001) and $Ba_{0.99}La_{0.01}SnO_3/SrTiO_3$(001) (60) thin films.

Figure 4.5 shows the temperature-dependent *n* (electron carrier density), μ (electron mobility), and ρ (electrical resistivity) to understand the electrical transport properties of $Ba_{0.995}La_{0.005}SnO_3$, $BaSn_{0.97}Sb_{0.03}O_3$, and $BaSnO_{3-\delta}$ single crystals as well as $Ba_{0.99}La_{0.01}SnO_3/SrTiO_3$(001) and $Ba_{0.995}La_{0.005}SnO_3/BaSnO_3$(001) thin films (*40, 82, 92*). First, all the *n* is almost temperature independent in those crystals and films. ρ in both crystals and films mostly increases with increase of temperature; this typical metallic behavior clearly supports that they remain in a degenerately doped semiconducting regime. ρ of the $Ba_{0.995}La_{0.005}SnO_3$ crystal decreases nearly by a factor of two upon being cooled from room temperature to 2 K due to the increase of μ by the same factor. The μ increase at low temperatures mainly originates from the reduction of the acoustic phonon scattering, indicating that the scattering rate due to acoustic phonons is approximately half of the total scattering rate at room temperature.

It should be noted that μ values in BLSO/$BaSnO_3$(001) correspond to the largest one among perovskite perovskite oxide films grown by PLD at room temperature . Furthermore, those μ values are comparable to or even larger than those of other familiar TOS films at a similar *n* regime (*93-95*). Yet, they are still three times smaller than the best-known values in BLSO single crystals (*25*). Moreover, the resistivity (residual-resistivity ratio) of the BLSO films on the $SrTiO_3$(001) and $BaSnO_3$(001) substrates are generally larger (smaller) than that of $Ba_{0.99}La_{0.01}SnO_3$ crystals, implying that there exist extra-scattering sources in the BLSO/$SrTiO_3$(001) and BLSO/$BaSnO_3$(001) films. Based on the extensive research outcome for growing high quality $SrTiO_3$ thin films (*96-98*), we attribute the extra-scattering sources to cation vacancies or cation site mixing in the BLSO/$BaSnO_3$(001) films (*92*) and to a large fraction of threading dislocations or grain boundaries in the BLSO/$SrTiO_3$(001) films (*40*). Therefore, it is worthwhile to investigate systematically the effect of point defects on the μ behavior of BLSO thin films in future studies.

4.4 Recent efforts to improve mobility in doped $BaSnO_3$ films

Researchers are currently attempting to grow thin films by using substrates with an a_c or pseudocubic lattice constant (a_{pc}) (*99*) close to that of $BaSnO_3$. In Fig. 4.6, we summarize the band gap versus a_c (or a_{pc}) of the cubic (or orthorhombic) perovskite materials that have been used or can be used potentially as substrates for growing $BaSnO_3$ films. Table 4.1 includes detailed data and references for Fig. 4.6.

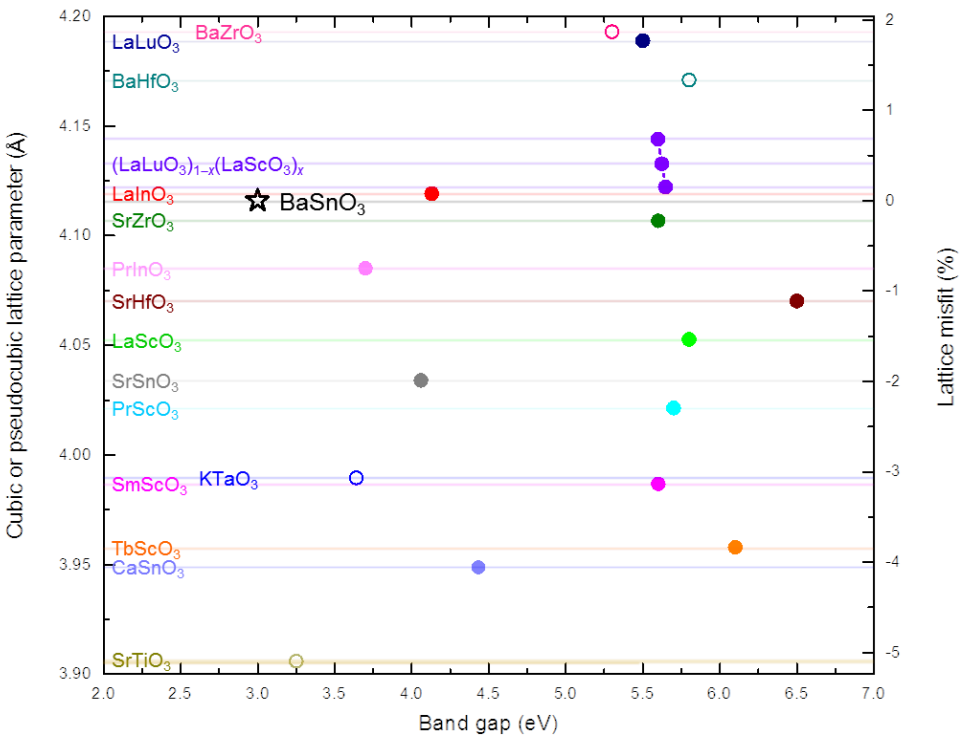

Figure 4.6 Band gap versus either a_c or a_{pc} (and lattice misfit with $BaSnO_3$) in cubic (*open*) or orthorhombic (*solid*) perovskites. Most of the band gap values are from experiments on optical gaps, whereas those of scandates are from first-principles calculations. Table 4.1 includes detailed data and references.

Table 4.1 Comparison of cubic or pseudo-cubic lattice parameters, lattice misfit to $BaSnO_3$, and band gap of the cubic or orthorhombic perovskite that have been used or can be used potentially as a substrate for growing the $BaSnO_3$ films.

	Cubic or Orthorhombic	**Orthorhombic**				**Cubic**	**Lattitce misfit to $BaSnO_3$ (%)**	**Band gap (eV)**	**References**
		Lattice parameters (Å)			Pseudo-cubic lattice parameters (Å)	Cubic lattice parameters (Å)			
		a	***b***	***c***	a_{pc}	a_c			
$SrTiO_3$	Cubic	-	-	-	-	3.905	-5.13	3.26	(*100*, *101*)
$aSnO_3$	Orthorhombic	5.5142	7.8816	5.6634	3.948	-	-4.08	4.44	(*70*, *102*)
$TbScO_3$	Orthorhombic	5.466	7.917	5.731	3.958	-	-3.84	6.10	(*103*, *104*)
$KTaO_3$	Cubic	-	-	-	-	3.990	-3.07	3.64	(*66*, *105*)
$SmScO_3$	Orthorhombic	5.527	7.965	5.758	3.987	-	-3.14	5.60	(*104*, *106*)
$PrScO_3$	Orthorhombic	5.608	8.025	5.780	4.021	-	-2.30	5.70	(*104*, *107*)
$SrSnO_3$	Orthorhombic	5.709	8.065	5.703	4.034	-	-1.99	4.00	(*70*, *108*)
$LaScO_3$	Orthorhombic	5.6803	8.0945	5.7907	4.053	-	-1.54	5.80	(*109*, *110*)
$SrHfO_3$	Orthorhombic	5.752	8.134	5.765	4.070	-	-1.11	6.50	(*111*, *112*)
$PrInO_3$	Orthorhombic	5.908	8.1538	5.6605	4.085	-	-0.75	3.70	(*113*)
$SrZrO_3$	Orthorhombic	5.800	8.205	5.822	4.107	-	-0.22	5.60	(*114*, *115*)
$BaSnO_3$	Cubic	-	-	-	-	4.116	0.00	3.00	(*40*, *101*)
$LaInO_3$	Orthorhombic	5.9414	8.2192	5.7249	4.119	-	0.08	5.00	(*116*)
$BaHfO_3$	Cubic	-	-	-	-	4.1710	1.34	5.80	(*117*, *118*)
$LaLuO_3$	Orthorhombic	5.8259	8.3804	6.0218	-	-	1.77	5.50	(*119*, *120*)
$BaZrO_3$	Cubic	-	-	-	-	4.1930	1.87	5.30	(*121*, *122*)

Figure 4.7 shows μ at room temperature as a function of n for electron-doped $BaSnO_3$. Several studies have improved crystallinity and μ of films by using substrates with reduced lattice misfits. Substrates with an orthorhombic structure include $SmScO_3(110)_O$, $TbScO_3(110)_O$, and $PrScO_3(110)O$. Here, the subscripted O refers to the orthorhombic index. For these structures, a_{pc} and lattice misfit compared with $BaSnO_3$ are as follows: $SmScO_3(110)_O$ (3.868 Å, −3.07 %), $TbScO_3(110)_O$ (3.958 Å, −3.84 %), and $PrScO_3(110)_O$ (4.021 Å, −2.30 %)) (Table 4.1). In 2014, Wadekar et al. (*123*) fabricated BLSO films on $SmScO_3(110)_O$ substrates by the PLD technique and found μ = ~10 $cm^2V^{-1}s^{-1}$. As an alternative idea to enhance μ, Park et al. (*124*) deposited a $BaSnO_3$ buffer (thickness t = 110 nm) on $SrTiO_3(001)$ substrate before growing BLSO films to find reduced threading dislocations and enhanced μ = ~80 $cm^2\ V^{-1}\ s^{-1}$ in the BLSO film. Shiogai et al. (*125*) also grew BLSO films grown on $(Ba,Sr)SnO_3$ buffer (t = ~200 nm)/$SrTiO_3(001)$, finding μ = 78 $cm^2\ V^{-1}\ s^{-1}$ at $n = 1.6 \times 10^{20}\ cm^{-3}$.

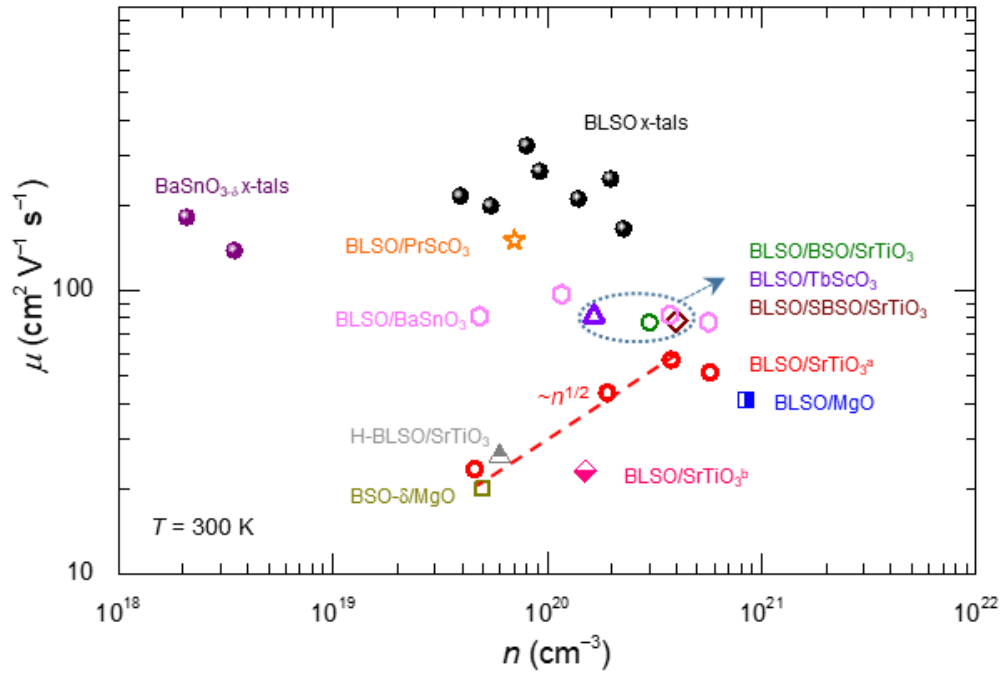

Figure 4.7 Summary of experimental μ data in thin films prepared by pulsed laser deposition [BLSO/$SrTiO_3$ (*40*, *81*), BLSO/$SmScO_3$ (*123*), BLSO/BSO/$SrTiO_3$ (*124*), BLSO/SBSO/$SrTiO_3$[a] (*125*), BLSO/$BaSnO_3$ (*92*), H-BLSO/$SrTiO_3$ (*126*), (Ba,Gd)SnO_3/$SrTiO_3$ (*127*), BLSO/MgO (*128*)], sputtering [$BaSnO_{3-\delta}$/MgO (*129*)], solution deposition [BLSO/$SrTiO_3$[b] (*130*)], and molecular beam epitaxy [BLSO/$PrScO_3$ (*18*), BLSO/$TbScO_3$ (*131*)] at room temperature. μ of BLSO/$SrTiO_3$[a] (*40*) closely follows the $n^{1/2}$ dependence (*red dashed line*). Abbreviations: μ, electron mobility; BLSO, (Ba,La)SnO_3; BSO, $BaSnO_3$; H-BLSO, hydrogen-treated BLSO; n, electron carrier concentration; SBSO, (Sr,Ba)SnO_3.

In addition to these known substrates, there are recent research efforts to find new substrate materials. Uecker et al. (*132*) recently synthesized large single crystals of $(LaLuO_3)_{1-x}(LaScO_3)_x$ with a_{pc} between 4.09 and 4.18 Å by the Czochralski method. The grown crystals had a length of approximately 75 mm and a diameter of 15 mm. We anticipate that new single crystals of $(LaLuO_3)_{1-x}(LaScO_3)_x$ for which a_c is near 4.116 Å could be useful for growing high-quality $BaSnO_3$ films. In another effort, our group

recently succeeded in growing large $LaInO_3$ single crystals by the optical floating-zone method (*116*). $LaInO_3$ forms an orthorhombic perovskite structure with the *Pnma* space group, and the cell parameters are a = 5.9414 Å , b = 8.2192 Å , and c = 5.7249 Å . Although $LaInO_3$ has an orthorhombic distortion, its a_{pc} = 4.119 Å is close to that of $BaSnO_3$. The length of the grown crystal is ~50 mm, and its diameter is ~7 mm. The main direct gap and ε_r are 4.13 eV and 23.7, respectively, demonstrating that the system is another transparent material with a rather high ε_r. Indeed, several theoretical and experimental studies show that $LaInO_3$ is a polar material at the atomic scale [due to sequential layers of $(LaO)^+$ and $(InO_2)^-$] and can thus induce two-dimensional electron gases (2DEGs) and electrical conductivity in a $LaInO_3$-$BaSnO_3$ heterostructure (*133*, *134*). Therefore, systematic studies of uniaxial or biaxial strain effects on the physical properties of $LaInO_3$ become necessary for designing and understanding possible 2DEGs behavior at the $LaInO_3$-$BaSnO_3$ heterointerface.

4.5 Attempting to realize homo-epitaxial $BaSnO_3$ thin film field-effect transistors

A key device in such transparent applications is a field-effect transistor (FET). In particular, to produce FETs with high performance, single crystalline films of TOSs have become essential because they can minimize the density of defects and dislocations. In this regard, thin film transistors (TFTs) based on single crystalline films have been fabricated (*135-139*) to provide a field-effect mobility (μ_{FE}) as high as ~80, ~70, and ~9 $cm^2V^{-1}s^{-1}$ in the $InGaO_3(ZnO)_5$ (*135*), ZnO (*136*), and In_2O_3 (*137*) channels, respectively. Moreover, μ_{FE} in a TFT based on $SrTiO_3$ reached only ~3 $cm^2V^{-1}s^{-1}$ at room temperature even though a single crystalline film was used as an active channel (*140-142*). Therefore, the low μ_{FE} remains as one of the main hurdles to overcome in the utilization of the perovskite-based

TFTs.

Recently, TFTs based on BLSO channel with μ_{FE} = ~18 and ~90 $cm^2V^{-1}s^{-1}$ were reported (*124, 143*). However, those TFTs have used $SrTiO_3$(001) substrates and a thick $BaSnO_3$ buffer layers, due to the lack of a suitable substrate with good lattice matching property. By use of insulating $BaSnO_3$(001) substrates, we have demonstrated a successful operation of a TFT, in which the homo-epitaxial $BaSnO_3$ film on the $BaSnO_3$(001) substrate becomes an active channel (BSO-TFT/BSO(001)).

Figures 4.8(a) and (b) show a schematic drawing of our TFT structure and a top-view image of the device (TFT1) under a polarization microscopy, respectively. Figure 4.8(e) and (f) show the output (source-to-drain current *vs*. source-to-drain voltage, I_{DS} *vs*. V_{DS}) and transfer (source-to-drain current *vs*. source-to-gate voltage, I_{DS} *vs*. V_{GS}) characteristics of the TFT1, respectively. From the output characteristics, we found that I_{DS} increased with V_{DS} increase at a positive V_{GS}, indicating that the channel was n-type and *n* was generated by a positive V_{GS}. TFT1 exhibited ohmic properties at a low V_{DS} regime and current saturation at a high V_{DS} regime. This observation shows that the operation of the TFT1 follows the typical FET behavior and that the Fermi level in the $BaSnO_3$ channel is controlled by V_{GS} and V_{DS}. The saturation current (I_{DS_Sat}) in the standard FET is predicted from the following equation (*144*):

$$I_{DS\_Sat} \cong \frac{\mu c_{ox} w}{2L}(V_{GS} - V_T)^2 \qquad \text{Equation 4.33}$$

Here, c_{ox} is a gate capacitance per unit area and V_T is a threshold voltage. We extracted V_T from a linear fit in the $I_{DS}^{0.5}$ *vs*. V_{GS} plot to find V_T = 1.52 V. This value shows that TFT1 operates in an enhancement mode. The positive value of V_T indicates that the Fermi level in the $BaSnO_3$ channel is located below the energy level of the conduction band minimum.

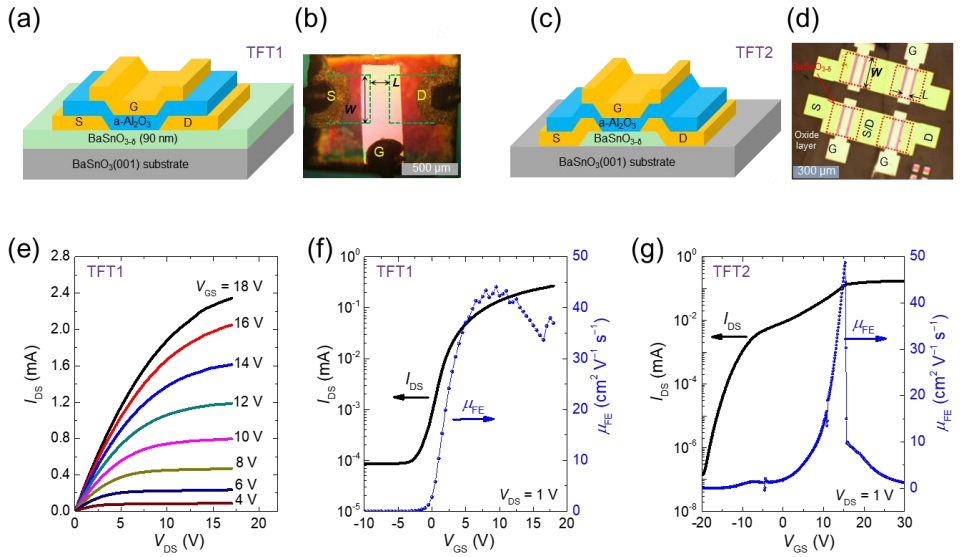

Figure 4.8 (a) Schematic device structures for the homo-epitaxial thin-film field-effect transistor grown on $BaSnO_3$(001) substrate with a top-gated metal-insulator-semiconductor configuration (TFT1). (b) A top-viewed picture of TFT1 under a polarization microscope. (c) A schematic device structure and (d) a top-viewed picture showing four BSO-TFT channels under a polarization microscope, which was fabricated by use of the Si stencil masks (TFT2). The channel length and the width of the device were 50 and 200 μm, respectively. (e) Output (I_{DS} *vs*. V_{DS}) and (f) transfer (I_{DS} *vs*. V_{GS}) characteristics of TFT1. (g) A transfer characteristic of TFT2 in (d).

The transfer characteristics show that the off-current was on the order of 100 nA and the on-to-off current ratio and subthreshold swing (S) were ~3 × 10^3 and 1.67 V/dec, respectively. In the off-state, the conductivity of the $BaSnO_3$ channel was found to be ~4.0 × 10^{-3} S cm^{-1} and n = ~2.6 × 10^{14} cm^{-3}, as estimated from μ = ~100 $cm^2V^{-1}s^{-1}$ of the BLSO films. This implies that a single-crystalline $BaSnO_3$ film with n < 10^{17} cm^{-3} is realized without the counter-doping of acceptors. From the transfer characteristics in Fig. 4.8(f), the μ_{FE} can be extracted based on the following equation (*144*):

$$\mu_{FE} \cong \frac{dI_{DS}}{dV_{GS}} \frac{L}{wc_{ox}V_{DS}} \qquad \text{Equation 4.34}$$

The calculated μ_{FE} in TFT1 was as high as ~45.0 $cm^2V^{-1}s^{-1}$, which is much larger than the typical μ_{FE} values (< 3 $cm^2V^{-1}s^{-1}$) reported in other TFTs based on the perovskite materials (*140-142*).

On the other hand, the relatively low on-to-off current ratio in TFT1 was mainly caused by the large off-current, coming from the exposure of large area (typically, 1 × 1 mm^2) of the $BaSnO_3$ film layer to the source/drain electrode although the growth condition for the gate oxide has been optimized. In order to reduce the off-current coming from the ill-defined channel area, we adopted micro-patterning technology to fabricate Si stencil masks, which allows us to reduce the $BaSnO_3$ film area. Figures 4.8(c) and (d) show a schematic drawing and a top-view image of the BSO-TFT/BSO(001) fabricated by the Si stencil masks (TFT2), respectively. The channel length and the width of the device are 50 and 200 μm, respectively. Figure 4.8(g) summarizes a transfer characteristic, I_{GS} *vs.* V_{Gs}, and μ_{FE} of TFT2. The on-to-off current ratio was indeed increased up to 1.2 × 10^6 while the μ_{FE} and the *S* were 48.7 $cm^2V^{-1}s^{-1}$ and 1.55 V/dec, respectively. For comparison, we also measured the μ_{FE} of the BSO-TFT on the $SrTiO_3$(001) substrate (BSO-TFT/STO(001)) and found only ~5 $cm^2V^{-1}s^{-1}$ (not shown). Moreover, the reported BLSO-TFT/STO(001) using a thick BSO buffer layer exhibited μ_{FE} of ~17.8 $cm^2V^{-1}s^{-1}$ (*124*), indicating that the homo-epitaxial $BaSnO_3$ channel is superior to those thin films grown on the $SrTiO_3$(001) substrates with the same a-Al_2O_3 gate oxide.

On the other hand, our μ_{FE} (*S*) are still lower (higher) than a recently reported μ_{FE} = ~90 $cm^2V^{-1}s^{-1}$ (*S* = 0.65 V/dec) of BLSO-TFT/STO(001) with a thick $BaSnO_3$ buffer layer and a new gate insulator $LaInO_3$ with high dielectric constant ε_r of ~39 (*143*). The relatively

low μ_{FE} and high *S* value of our TFT1 and TFT2 could be attributed to the interface charge traps between the channel and the gate oxide, indicating that μ_{FE} and *S* could be improved further. However, it should be noted that the obtained μ_{FE} = 48.7 $cm^2V^{-1}s^{-1}$, albeit without employing the gate oxide with high dielectric constant, is still quite high. This value is already comparable to those of the well-known TFTs based on the transparent binary oxide; for example, μ_{FE} was ~40 $cm^2V^{-1}s^{-1}$ in the ZnO-based TFT (*139*), in which a similar top-gate TFT was fabricated with an a-Al_2O_3 gate insulator. We also postulate that the electrical performance of the BSO-TFT can be further improved similar to the cases of the ZnO-based TFTs, in which various efforts, e.g., tuning the material property and the use of gate oxides with high dielectric constant have resulted the increase of μ_{FE} (*135*, *143*). Therefore, our work clearly demonstrates that fabricating homo-epitaxial films by use of the $BaSnO_3$ substrates could be a good pathway toward realizing new high-speed, multi-functional transparent devices based on the perovskite stannates.

Chapter 5 Stable electrical properties of (Ba,La)SnO_3 films

5.1 Overview

The thermal instability of oxygen is among the most intriguing of the physical properties that have become major bottlenecks in the device applications of oxide thin films. For example, many oxides are often subject to severe degradation due to thermal instability of oxygen. Moreover, in perovskite titanates, whether there is oxygen deficiency at the interface remains controversial in spite of much ongoing research on their 2DEG behavior (*145, 146*). Furthermore, in oxide-based resistive memory devices, the thermal stability of oxygen at the interface and/or their reaction with hydrogen and water fundamentally govern the electrical transport behavior of these devices under electric field (*147, 148*). The diffusion coefficient of oxygen is closely associated with its thermal stability, particularly above room temperature. On the other hand, it is rather difficult to find proper instrumentations to extract the diffusion coefficient of oxygen; several methods include secondary ion mass spectroscopy, thermo-gravimetric analysis, and electrical conductivity (σ) relaxation (*149-155*). In particular, the last method corresponds to an indirect but simple way of extracting the chemical diffusion coefficient of oxygen (D_O) from the measurement of σ relaxation in a specimen at high temperatures when V_O are created (or annihilated) inside the sample in low (or high) oxygen partial pressure ($P(O_2)$). It is based on the assumption that one V_O provides two electron carriers in oxides, and then the variation of $\sigma = ne\mu$ should directly reflect the change of V_O (*156-158*). The method has been often employed in thin films due to their relatively short relaxation times involved in the diffusion process and rather large variation of σ (*159-161*).

On the other hand, in some of donor-doped perovskite titanates, it is known that V_O is created only at low $P(O_2)$ condition to give rise to electron carriers while at high $P(O_2)$ condition, cation vacancies (V_C) become predominant to compensate donor-type dopants (*162-164*). Thus, the σ relaxation measurements could be also affected by the diffusion process of V_C inside a specimen rather than by only that of oxygen. In a previous σ relaxation measurements on BLSO/$SrTiO_3$(001) films, the diffusion process was assumed to occur by oxygen predominantly at 530 ºC, and the value of D_O was roughly estimated to be ~10^{-15} cm^2s^{-1} (Figs. 5.1(a) and (b)) (*25*). It is yet to be confirmed whether the diffusion process of V_C could be negligible in BLSO/$SrTiO_3$(001) films at 530 ºC. On the other hand, BLSO/$SrTiO_3$(001) films showed lots of TDs due to the large lattice mismatch between the substrate and the film, and resulted in much smaller μ coming from the extra carrier-scattering in the TDs (*25, 81*). As a result, the electron carriers were always less-activated than the expected value, indicating the charge-trapping effect in the TDs is significant. Accordingly, D_O extracted from the σ measurements was uncertain whether it truly reflects the *n*-change inside the BLSO grains or it is more affected by the μ- and *n*-variation due to the presence of TDs. Therefore, it is necessary to investigate *n* and μ separately for accurate extraction of D_O values. Furthermore, understanding the transport properties and diffusion processes of BLSO/$SrTiO_3$(001) film will provide useful guidelines for future device applications based on $BaSnO_3$ and BLSO films.

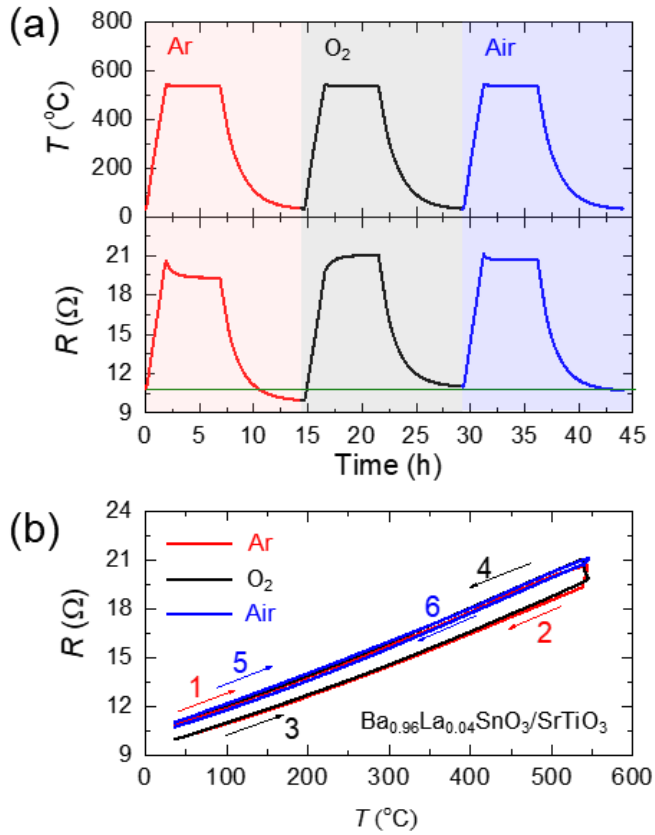

Figure 5.1 (a) Temperature *T* and gas atmosphere were varied according to the profile in the top panel. The resultant resistance (*R*) variation of a $Ba_{0.96}La_{0.04}SnO_3/SrTiO_3$(001) film is plotted in the bottom panel. (b) *R* decreased (increased) by approximately 8 % (9.5 %) under Ar (O_2) atmosphere in 5 h at 530 ◦C, whereas it changed by only approximately 1.7 % in air. The numbers (1 through 6), along with their corresponding arrows, denote the sequence of measurements under Ar (1, 2), O_2 (3, 4), and air (5, 6) atmospheres.

In this chapter, the author will introduce the investigation of time-dependent Hall effect of the BLSO/ $SrTiO_3$(001) film under O_2 (or Ar) atmosphere at high temperatures around 500 °C. We obtained the time-dependent *n* and μ separately, and found out that the change of *n* is a main cause of the σ variation. Moreover, we found that the time-dependent *n* curves under O_2 or Ar atmosphere exhibited two relaxation times, indicating that two

different kinds of oxygen transport possibly occur in the BLSO/$SrTiO_3$(001) film.

5.2 Hall effect of (Ba,La)SnO_3/$SrTiO_3$(001) films at high temperatures

Figure 5.2 summaries the time-dependent variations of electrical properties i.e., n, μ, and σ of the BLSO film at 530 °C under O_2 or Ar atmosphere. The initial values n_0, μ_0, and σ_0 at t = 0 were used to normalize each data; n_0, μ_0, and σ_0 were 4.35 (4.30) × 10^{20} cm^{-3}, 21.17 (20.97) $cm^2V^{-1}s^{-1}$, and 1.47 (1.44) × 10^3 $S{\cdot}cm^{-1}$ at 470 (530) °C, respectively. It is noteworthy that n values of BLSO film is about 76 % of n expected from the $Ba_{0.96}La_{0.04}SnO_3$ polycrystalline target; fully activated electron carriers should result in n = 5.73 × 10^{20} cm^{-3}. Moreover, measured μ of BLSO film is much lower than that of BLSO single crystals. Those reduced n and μ values are likely to originate from the large number of charge traps and scattering centers, possibly with higher La^{3+} ion concentration, that could be located in the grain boundaries and threading dislocations (*25, 81*).

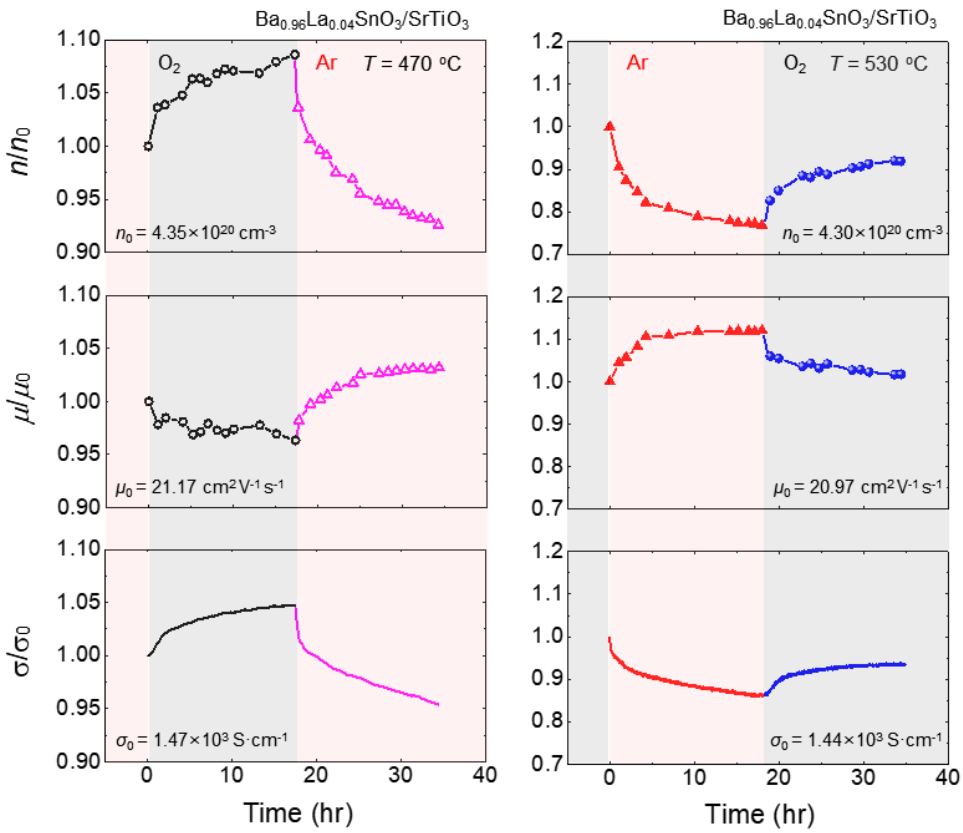

Figure 5.2 Time-dependent n, μ, and σ of the BLSO/$SrTiO_3$(001) film at 470 °C and 530 °C under O_2 or Ar atmosphere. The time-dependent n, μ, and σ data are normalized by the initial values (n_0, μ_0, and σ_0) (t = 0). Values of n_0, μ_0, and σ_0 are represented at the bottom-left corner of each graph.

Because the BLSO film has n-type carriers as confirmed by the Hall effect study, the increasing (or decreasing) behavior of n under Ar (or O_2) atmosphere implies the increase (or decrease) of the n-type carriers. This is seemingly consistent with the general wisdom that the reducing (or oxidizing) atmosphere generates (or fills-up) V_O present in the BLSO film. More importantly, the increasing behavior of μ under O_2 atmosphere implies the decrease of the scattering sources (e.g., V_O) rather than increase (e.g., V_C). In donor-doped perovskite titanates particularly at high temperatures more than 1000 °C, it is known that V_C are predominantly created at high $P(O_2)$ conditions to compensate donor-type dopants (*162*,

164, 165). In the present case of rather low temperature environment of ~500 °C, however, the observation of increased μ under O_2 atmosphere supports that the reduction of V_O is dominant over the creation of V_C even at high $P(O_2)$ condition. Therefore, we argue that equilibration kinetics in BLSO at such relatively low temperatures close to 500 °C should be mainly controlled by V_O rather than V_C in both reducing and oxidizing atmosphere. Main findings in Fig. 5.2 can be thus summarized as followings. First, the change of σ/σ_0 was mainly determined by that of n/n_0 while the variation of μ was not negligible in the BLSO film. Second, there exist fast and slow time scales that directly reflect the variation of n/n_0. Third, the variation of n is dominantly controlled by the change of V_O. Although we cannot completely rule out the possibility of creating a small amount of V_C, V_O seem to play a major role in resulting in the σ variation at a rather low temperature of ~500 °C.

5.3 Substrate effects on the electrical properties of (Ba,La)SnO_3 films

In order to check the effect of the $SrTiO_3$(001) substrate on the electrical transport properties of BLSO film, we also measured the time-dependent σ of the same $SrTiO_3$(001) substrate at 565 °C under O_2 and Ar atmosphere as summarized in Fig. 5.3. The overall σ value of $SrTiO_3$(001) ($1 \times 10^{-4} - 7 \times 10^{-4}$ S·cm^{-1}) is more than 10^7 times lower than that of BLSO film at 530 °C. As a result, electrical conductance of $SrTiO_3$(001) substrate (500 μm thick) turns out to be more than 350 times lower than that of BLSO film (60 nm thick). After annealing the $SrTiO_3$(001) substrate for 12 hours under O_2 atmosphere, the gas atmosphere was changed from Ar to O_2. Then, σ showed a fast increase during the initial 30 min. After the 30 min, σ kept increasing slightly. In contrast, when the gas atmosphere was changed from O_2 to Ar, σ decreased with a fast response in an hour and kept decreasing slightly after the initial 1 hour. Those time-dependent σ variations of $SrTiO_3$(001) substrate

are consistent with the previous results (*166-168*), but are completely opposite from those of BLSO film. This opposite behavior of σ relaxation and much insulating properties of the $SrTiO_3$(001) substrate rules out a possibility that the Hall effect behavior of BLSO film might be influenced by any change in the $SrTiO_3$(001) substrate.

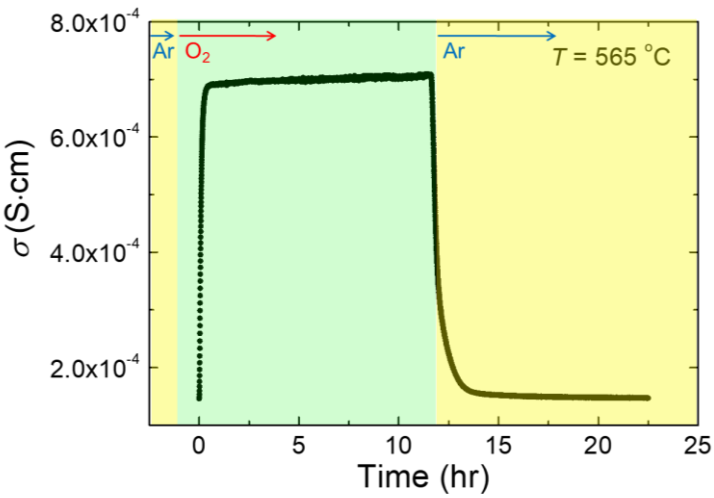

Figure 5.3 Electrical conductivity relaxation of the $SrTiO_3$(001) substrate at 565 ^oC under O_2 and Ar atmosphere.

5.4 Scattering analysis

Figure 5.4 shows the μ vs n curve obtained from the Hall data in Fig. 5.2. The closed triangles (closed circles) and open triangles (open circles) represent μ *vs.* n data for O_2 (Ar) atmosphere at 530 and 470 ^oC, respectively. It is clearly observed that μ is overall decreased when n is increased. Under the O_2 atmosphere, V_O will be reduced to result in the decrease of the n-type carrier numbers and then the carrier scattering is supposed to decrease as the ionized impurities are reduced to result in the increment of μ. This is an expected behavior in the limit of ionized impurity scattering.

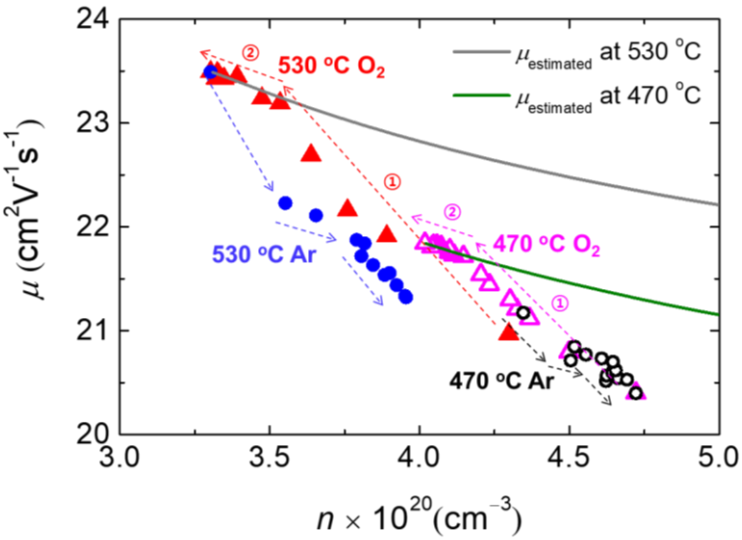

Figure 5.4 μ vs n curves of the BLSO/SrTiO$_3$(001) film extracted from the data in Fig. 5.2. Triangles (circles) represent O_2 (Ar) atmosphere and closed (open) symbols represent the measurement temperature of 530 (470) ^{o}C. Gray (green) line shows the estimated μ curve at 530 ^{o}C (470 ^{o}C). Arrows and each step indicate the time evolution sequence of the $\mu(n)$ data. Time interval between each symbol roughly corresponds to 1-2 hours.

On the other hand, it is known in the BLSO film that carrier scattering occurs mostly in the TDs although carrier scattering due to ionized impurities still exists (*25, 40, 81*). As dominant ionized impurities, La^{3+} ions and V_O should be considered. According to the Matthiessen's rule, μ of the BLSO film can be expressed as

$$\frac{1}{\mu} = \frac{1}{\mu_{\text{ii\_La}}} + \frac{1}{\mu_{\text{ii\_Vo}}} + \frac{1}{\mu_{\text{TD}}} + \frac{1}{\mu_{\text{other}}}, \qquad \text{Equation 5.1}$$

where $\mu_{\text{ii\_La}}$, $\mu_{\text{ii\_Vo}}$, and μ_{TD} represent the μ contributions from La dopants, V_O, and TDs, respectively. Here, μ_{other} is governed by all remaining scattering sources, such as phonons and other unexpected defects. For degenerate semiconductors, μ_{ii} can be expressed as (*30, 90*),

$$\mu_{ii} = \frac{3(\varepsilon_r \varepsilon_0)^2 h^3}{Z^2 m^* e^3} \frac{n}{N_i} \frac{1}{F_{ii}(\xi)}, \qquad \text{Equation 5.2}$$

with

$$F_{ii}(\xi) = \ln(1+\xi) - \frac{\xi}{1+\xi}, \qquad \text{Equation 5.3}$$

and

$$\xi = (3\pi^2)^{1/3} \frac{\varepsilon_r \varepsilon_0 h^2 n^{1/3}}{m^* e^2}, \qquad \text{Equation 5.4}$$

where ε_r of $BaSnO_3$ is ~20 (*169*) and m^* of $BaSnO_3$ is ~0.2 – 0.6m_0 (*40, 133, 170-174*). Considering that n of the BLSO film should be the sum of concentrations of the La dopant (n_{La}=N_{La}) and V_O (n_{Vo}= 2N_{Vo}), Equation 5.1 can be rewritten as

$$\frac{1}{\mu} = \left(\frac{3(\varepsilon_r \varepsilon_0)^2 h^3}{m^* e^3} \frac{n_{La} + n_{Vo}}{n_{La}} \frac{1}{F_{ii}(\xi)} \right)^{-1} + \left(\frac{3(\varepsilon_r \varepsilon_0)^2 h^3}{4m^* e^3} \frac{n_{La} + n_{Vo}}{n_{Vo}/2} \frac{1}{F_{ii}(\xi)} \right)^{-1} + \frac{1}{\mu_{TD}} + \frac{1}{\mu_{other}}. \qquad \text{Equation 5.5}$$

We can estimate μ from the ionized impurity scattering with Equation 5.5. Two solid lines in Fig. 5.4show the estimated μ curves at 470 and 530 ^oC, respectively. In order to obtain the estimated μ curves, we assumed that in the final stage after the O_2 annealing for 16 hours, n_{Vo} becomes almost negligible and μ approaches the experimental value [by adjusting ($1/\mu_{TD}$ + $1/\mu_{other}$) as a constant]. The estimated lines well explain the slow variation of μ near the step 2 under O_2 atmosphere, suggesting that the slow relaxation should be related to the reduced V_O located inside the BLSO grains.

On the other hand, the fast relaxation causing the μ-variation during the initial

annealing sequence (step 1) under O_2 atmosphere is much steeper than the estimated solid lines near the step 2. This indicates that there is another source to change the carrier scattering and concentrations considerably. One tempting scenario to explain the initial fast increment of μ might be due to the diffusion process along TDs or grain boundaries (*156, 161*). In the TEM results of the BLSO/$SrTiO_3$(001) film (Fig. 4.3(a)), TDs have indeed been observed as a main feature of the local structure. Moreover, in some of oxide materials, say $YBa_2Cu_3O_{7-\delta}$, the fast relaxation of σ was sometimes associated with the fast in-plane diffusion via the dislocation regions (*175*). However, there exists a conflicting result that diffusion along the dislocations might not be fast enough (*176*), which is obviously inconsistent with the above scenario. In the present film, as densities of TDs calculated from AFM images are typically less than 10^{11} cm^{-2} (*81*), which corresponds to < 10^{17} cm^{-3} for 60 nm thickness, the influence of TDs on the *n* relaxation might not be significant enough to cause such a large and fast increase of Δn = ~10^{20} cm^{-3} as observed in Fig. 5.4 (step 1 at 530 ^{o}C). Moreover, BLSO has the cubic perovskite structure so that D_O would be quite isotropic in contrast to the case of $YBa_2Cu_3O_{7-\delta}$.

5.5 Oxygen diffusion in (Ba,La)SnO_3 film

It is generally known in thin films that overall oxygen transport is controlled by two steps, i.e., the bulk diffusion and the oxygen reaction kinetics at the gas-film interface. Oxygen surface activation can then compensate V_O at surfaces, resulting in the *n* variation and the reduced scattering centers. In the SnO_2 nanowires and polycrystals (*177, 178*), the two relaxation times have been similarly observed due to the existence of oxygen reaction kinetics at the surface regions as well as subsequent diffusion into the grains. The former was attributed to the existence of depleted layer due to the fast electron transfer to the adsorbed oxygen on the surface, resulting in initial abrupt increase of electrical resistance.

In analogy with the case of SnO_2, we postulate that the BLSO film, which likely terminates in the SnO_2 layer, might have similar reaction kinetics due to the adsorbed oxygen at the surface, possibly causing the fast variation of μ and n in Fig. 5.4. For Ar atmosphere, it seems that the slow μ variation is located in the middle of the steeply increasing sequence to result in apparent three different regions. This observation indicates that complex interplay between gas reaction kinetics and bulk diffusion processes coexists in the Ar atmosphere.

As we have determined the variation of n reflecting the density of V_O inside the BLSO grains, time-dependence of n could be an ideal parameter to investigate time-dependent oxygen diffusion process in the BLSO film. In order to fit time-dependent n curves, rather than comparing the discrete experimental $n(t)$ data points in Fig. 5.2, we first calculated time-dependent n curve (n_{cal}) to add up more data points especially in the first 1 hour after changing the gas atmosphere. Figures 5.5(a) and (b) show n_{cal} curves under Ar and O_2 atmospheres at 470 (thick black lines) and 530 ^oC (thick blue lines). For this, we interpolated finite μ data in Fig. 5.2 to obtain smooth μ curves (μ_{fit}) by a polynomial fit. Using the interpolated σ data from the rather continuous experimental σ data in Fig. 5.2, we calculated $n_{cal} = \sigma/(e\mu_{fit})$. We also confirmed that the extracted n_{cal} curves well matched with the discrete n data points in Fig. 5.2. It is noteworthy that n_{cal} relaxation curves do not reach an equilibrium point. Those unsaturated relaxation curves even in the film indicate that the oxygen diffusion into the BLSO grains occurs quite slowly. Such an unsaturated behavior has also been observed in the σ relaxation of the SnO_2 nanowires with increasing thickness (*179*), supporting that the slow bulk diffusion process can cause apparently unsaturated n relaxation.

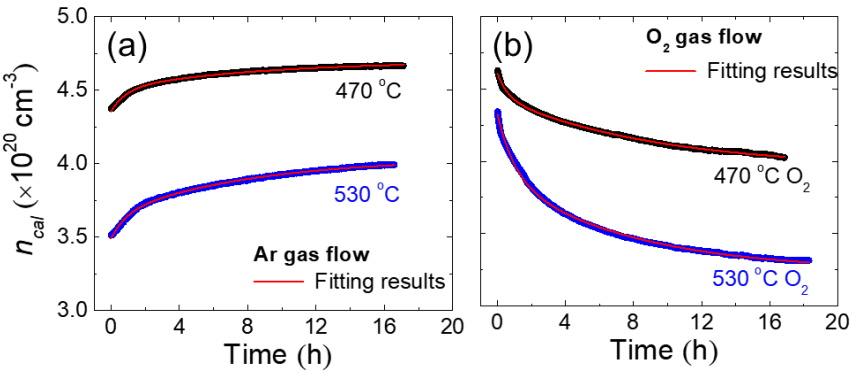

Figure 5.5 Time-dependent $n_{cal} = \sigma/(e\mu_{fit})$ and the fitting results (thin red solid lines) under (a) Ar atmosphere and (b) O_2 atmosphere. Thick black and blue solid lines correspond to n_{cal} data at 470 °C and 530 °C, respectively. Fitting results with the two exponentially decaying functions well explain the experimental data.

Related to this, our efforts to fit $n_{cal}(t)$ curve with a single exponential decay produced large discrepancy, supporting that there clearly exist another time constants in the exponentially decaying $n_{cal}(t)$ curves (*161*). To achieve a good fit of the experimental curves, we should fit the $n_{cal}(t)$ curves at least with the two exponentially decaying functions with two different τ, which we term τ_1 and τ_2, respectively (*161*, *175*). Figures 5.5(a) and (b) show that the fitted curves (thin red lines) are well matched with the $n_{cal}(t)$ curves in all the conditions used, i.e., under O_2 and Ar atmospheres and at 470 and 530 °C. The fitting results again support that the two steps of oxygen transport could exist in the BLSO film. Because short τ_1 is mainly associated with the fast surface reaction kinetics, only the long τ_2 should be linked to the intrinsic chemical diffusion time inside BLSO grains.

To extract the D_O value in the BLSO grains based on the above fit, we first note that the diffusion inside the BLSO grains mostly occurs along the *c*-axis (*161*). Even if the diffusion along the *ab*-plane occurs via the TDs, the related relaxation time due to the in-

plane diffusion will be similar to that along the *c*-axis because the diffusion coefficient is expected to be isotropic in the cubic perovskite and a typical distance of ~50 nm between TDs is comparable to the film thickness of 60 nm. We can then consider one-dimensional diffusion equation that presents a single exponential time constant due to the diffusion inside homogeneous grains along the *c*-axis (*161, 180, 181*). From the determined τ_2, it is straightforward to extract D_O by the relationship $\tau_2 = d_f^2/(\pi^2 D_O)$. Table I summarizes the resultant τ_1, τ_2, and D_O of BLSO/STO(001) film. The obtained D_O at 470 and 530 ºC under Ar (O_2) atmosphere are 1.17×10^{-16} (1.10×10^{-16}) cm^2s^{-1} and 1.24×10^{-16} (1.31×10^{-16}) cm^2s^{-1}, respectively. The different gas atmosphere appears to yield similar τ_2 and D_O values, implying that oxygen in- and out-diffusion processes in the BLSO grains have similar τ_2 and D_O values at ~500 ºC. Obtained D_O values are one order lower than that obtained by previous σ relaxations (*25*). Most importantly, D_O values turn out to be much lower than those of the perovskite oxides such as $SrTiO_3$, $BaTiO_3$, and $LaCoO_3$, in which the global values of diffusion coefficient of oxygen from chemical and tracer diffusion are in the range of 10^{-10}, 10^{-11}, and 10^{-11} cm^2s^{-1} at a similar temperature region, respectively (*182-185*). The low value of D_O of BLSO at around 500 ºC constitutes a solid evidence for why the electrical properties of BLSO films are stable up to 530 ºC.

Table 5.1 All fitted relaxation time constants (τ_1 and τ_2) and chemical diffusion coefficient of oxygen (D_O) values of BLSO/$SrTiO_3$(001) film.

	τ_1 (s)	τ_2 (s)	D (cm^2s^{-1})
470 ℃ Ar	3099	31253	1.17×10^{-16}
470 ℃ O_2	2185	33175	1.10×10^{-16}
530 ℃ O_2	3657	27843	1.31×10^{-16}
530 ℃ Ar	3164	29485	1.24×10^{-16}

Chapter 6 Atomically flat SnO_2-terminated $BaSnO_3$(001) substrates

6.1 Overview

Although there exits currently worldwide research activities to increase electron mobility in doped $BaSnO_3$ films through defect minimization (*18, 92, 131*), heterostructure-engineering could provide yet another promising route to realize high electron mobility at ambient temperature via achieving oxide based 2DEGs. Several theoretical predictions have recently proposed that the $BaSnO_3$ system as a channel material could be a great candidate to generate 2DEGs (*133, 186, 187*). In contrast to such ample theoretical predictions, the experimental activity on possible 2DEGs in the $BaSnO_3$ system is in a still nascent stage (*101, 134*). To control the interfacial properties in the $BaSnO_3$-based heterostructure, it is essential to secure a proper substrate with a good lattice match. For this, it will be useful to realize a $BaSnO_3$(001) substrate with an atomically flat surface with a termination of single oxide layer. However, surfaces of most ABO_3(001) substrate as obtained by cleaving, cutting, or polishing resulted in a mixed nature with coexisting domains with AO- and BO_2-termination (*188, 189*). These chemically mixed termination can be turned into atomically flat, single oxide terminating surface with step-terrace structures by performing solution etching and/or thermal annealing (*190*).

In this chapter, the author will introduce successful realization of atomically flat, nearly single oxide terminating surfaces of $BaSnO_3$(001) substrates by employing a short deionized water leaching and applying proper thermal annealing conditions. The effects of substrate miscut angles on the step bunching and kinked step behaviors will be also discussed. From the Ba^{2+} and Sn^{4+} signals in the 3*d* core-level spectra in combination with

atomic force microsocpy, we demonstrated that the top most surface of $BaSnO_3$(001) substrates is nearly composed of the SnO_2-terminating terraces with a single unit step between neighboring terraces.

6.2 Surface reconstruction by thermal annealing

Figure 6.1(a) shows transparent $BaSnO_3$(001) and $BaSnO_{3-\delta}$(001) substrates grown by the flux method. In contrast to the $BaSnO_{3-\delta}$(001) substrate showing metallic resistivity of 1 mΩ·cm, $BaSnO_3$(001) substrate exhibited superior insulating behavior of ~10^{12} mΩ·cm (*92*). The crystal miscut angles are known to be crucial parameters to produce a terrace nanostructure on the surface (*191*), In order to obtain well-defined topography of terraces and parallel steps, we polished sample surface by considering two miscut angles, i.e., out-of-plane miscut angle α = atan(H/W) and in-plane miscut angle φ, where H and W are height and width of terrace, respectively. Figures 6.1(c) and (d) display schematically the two miscut angles of α and φ. During the polishing procedure, α and φ were carefully controlled by tilting the single crystals to result in the variation of α from 0.05 to 1.0 ^{o} and the variation of φ from 0 to 45 ^{o}. After the etching and thermal treatment, we found that the change of α from 0.1-1.0 ^{o} resulted in the variation of one terrace width from 230 to 23 nm range. Moreover, between the two close terraces with the same termination type, a step with one unit cell (u.c.) height, i.e. 0.4116 nm, was formed (see below).

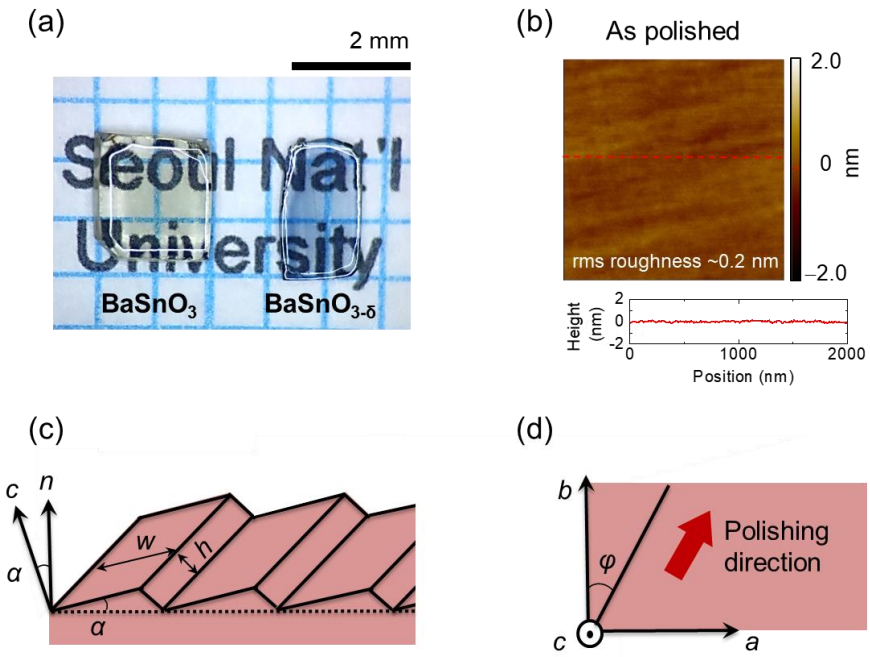

Figure 6.1 (a) Polished (001) and $BaSnO_{3-\delta}$(001) single crystals grown by the CuO/Cu_2O flux method. (b) Surface morphology and height profile of the polished $BaSnO_3$(001) substrate. The height profile is taken along the dotted solid line. (c) Schematic of a substrate with miscut angles. The out-of-plane miscut angle α is atan(H/W). L and W are the terrace width and step height, respectively. (d) Top view of a surface where the steps show an in-plane miscut angle φ with respect to the b axis of the cubic perovskite structure.

The AFM study of an as-polished $BaSnO_3$(001) substrate resulted in a maximum height difference of 0.5 nm and root-mean-square (rms) roughness of ~0.2 nm (Fig. 6.1(b)). Because the rms roughness of commercial $SrTiO_3$(001) substrates is typically around 0.1 nm, the rms roughness of ~0.2 nm in the as-polished surface seemed reasonably small enough before being chemical etching and heat treatment. In addition, the polished $BaSnO_{3-\delta}$(001) substrate showed almost similar surface morphology with an rms roughness ~0.2 nm (not shown here).

Figure 6.2 illustrates how the top most surface of the $BaSnO_3$(001) substrate exhibits

progressive transformation in the surface texture by thermal annealing. In general, the chemical control of top most surface termination can be realized by electronic reconstruction, changes in stoichiometry, or combination of both electronic and atomic reconstructions. For this, one usually applies several processes such as acidic solution etching, thermal annealing, or both acidic solution etching and thermal annealing (*191*). In our case, after cleaning the as-polished surface, the substrates were agitated in deionized water for 10 sec for achieving weak surface etching. Then, we annealed the substrates in the tube furnace. No change in the surface morphology occurred in the thermal annealing process below 1100 ^{o}C as compared with the as-polished surface. Upon annealing at 1100 ^{o}C for 10 min in an O_2 flow atmosphere, however, a small corrugation starts to appear in the surface of $BaSnO_3$(001) substrate (Fig. 6.2(a)). This indicates that the thermal annealing at 1100 ^{o}C produces electronic and atomic reconstructions. At this stage, it is likely that the top most surface is still composed of mixed-chemical terminations, i.e., both SnO_2 and BaO terminations.

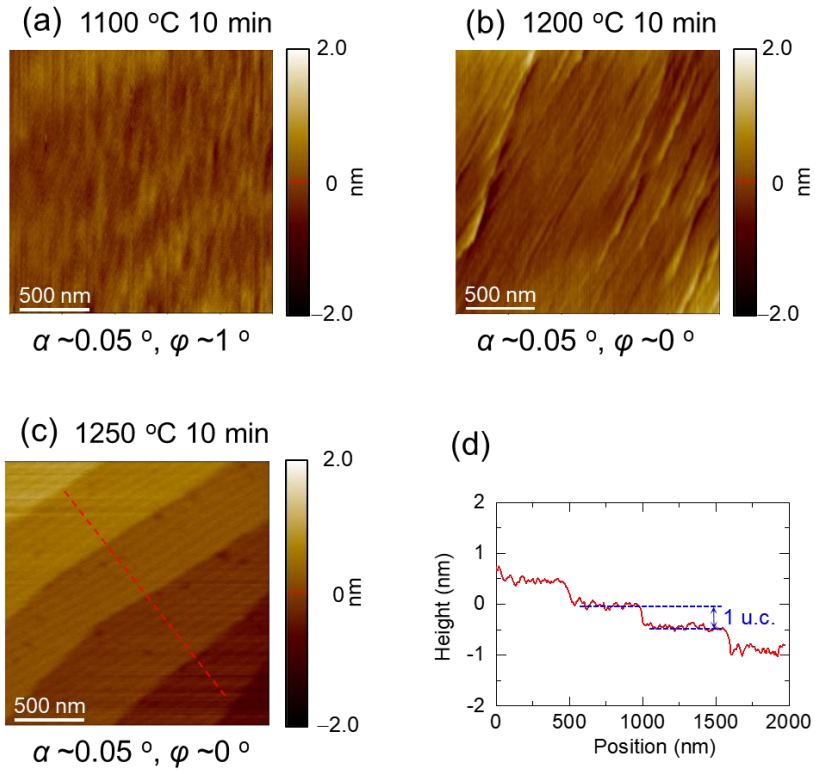

Figure 6.2 Surface morphology studies of $BaSnO_3$(100) substrates after the process of soaking in deionized water followed by thermal annealing. AFM topographic images after thermal annealing at (a) 1100 °C, (b) 1200 °C, and (c) 1250 °C for 10 min in O_2 flowing atmosphere with a flow rate of 10 ml/min. (d) The corresponding topographic profiles along the dotted line shown in (c).

When the $BaSnO_3$(001) substrate was annealed at 1200 °C for 10 min in O_2 flow, the surface shows the formation of partially aligned, stripe-like patterns, which might develop further into step edges (Fig. 6.2(b)). However, even if we increase the annealing time up to 2 hours at 1200 °C, the surface diffusion was not high enough to induce further noticeable morphological changes. Therefore, annealing condition was then adjusted into 1250 °C for 10 min in an O_2 flow condition, which finally produced atomically flat and wide terrace regions as seen in Fig. 6.2(c). The resultant mean-terrace-width is about 500 nm wide and

each step has one u.c. in height (~0.4116 nm) with straight ledges. We found that this kind of wide terrace was formed when the miscut angle α was adjusted to be less than 0.1 ° before polishing. The small miscut angle of α was also confirmed by the X-ray ω-scan. As a result, the rms roughness within a terrace did not exceed 1 Å. The line profile measured along the dotted line, shown in Fig. 6.2(c), exhibits only single unit cell steps of $BaSnO_3$ within the AFM resolution (Fig. 6.2(d)). This result has been reproduced in many equally treated $BaSnO_3$(001) as well as $BaSnO_{3-\delta}$(001) substrates. This observation also supports that the top most surface layer is terminated with one kind of chemical layers such as BaO or SnO_2.

6.3 Step bunching & kinked steps

In order to study the dependence of the surface morphology variation with respect to α, $BaSnO_3$(001) substrates having relatively large values of α were investigated after the same heat treatment, i.e., 1250 °C for 10 min in an O_2 flow condition. Figure 6.3(a) shows AFM image of the $BaSnO_3$(001) substrate with α = ~0.7 ° and φ = ~0 °, displaying a characteristic feature that the terrace width growth is delimited by having crossed facets between neighboring step edges. The average terrace width turns out to be ~250 nm and the height profiles reveal ~4-8 u.c. high steps in the step edges (Fig. 6.3(c)), which is in agreement with the miscut angle extracted by the X-ray ω-scan. This step-bunching formation is consistent with those observed in $SrTiO_3$(001) (*192*) and Si(113) (*193*) substrates with α values close to 0.2 ° and 1.7 °, respectively. Furthermore, in order to check the effect of φ, $BaSnO_3$(001) substrates having large φ were investigated too. Figure 6.3(b) presents the surface morphology of $BaSnO_3$(001) substrate with α = ~0.2 ° and φ = ~45 °, in which significant step-edge meandering and sharp triangular shape domains are found. The presence of such triangular shaped domains can be associated with the large value of φ. A

similar morphological feature has been also reported in the $SrTiO_3$(001) substrates prepared with such high values of 35 º and 6 º (*192*, *194*).

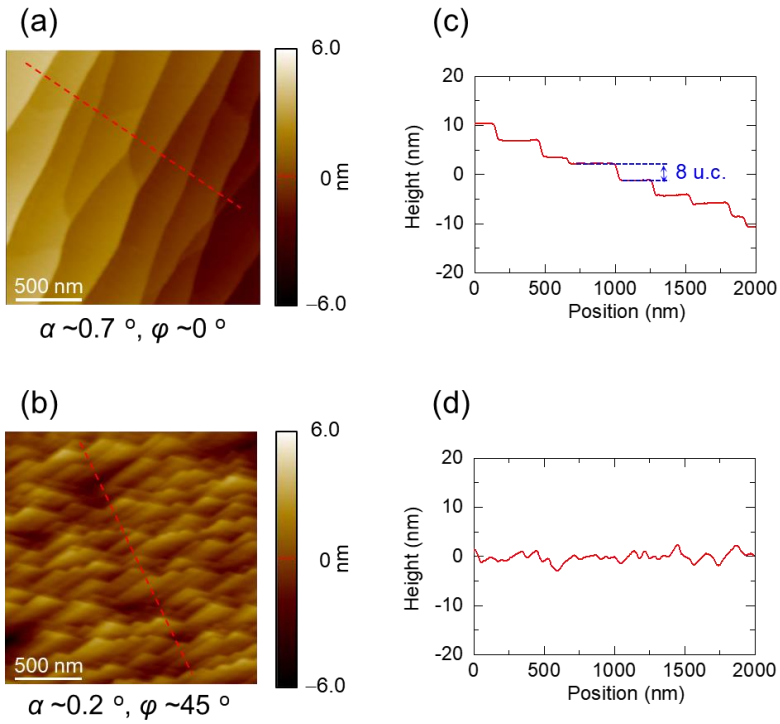

Figure 6.3 AFM topographic images of $BaSnO_3$(001) substrates with (a) large in-plane miscut angle (α ~0.7 º) and (b) large out-of-plane miscut angle (φ ~45 º) treated at 1250 ºC for 10 min in O_2 atmophere. (c) and (d) The corresponding height-profiles along the dotted lines shown in (a) and (b).

6.4 Surface termination of $BaSnO_{3-\delta}$(001) substrate

In order to determine the surface termination layer, the XPS was used to characterize $BaSnO_{3-\delta}$(001) surface, which has formed a large terrace width ~ 500 nm and one u.c. high step edges, similar to the case shown in Fig. 6.3(c). In particular, the XPS measurements were performed at various photoemission angles θ with respect to the surface normal (Fig.

6.4(a)). Figures 6.4(b) and (c), the core-level spectra are presented in the vicinity of Ba3*d* and Sn3*d* states measured at various θ. First of all, when θ increases from 0 to 70 °, it is expected that the surface contribution to the spectra should increase considerably (*195*, *196*). In other words, by going to larger θ, the effective electron escape depth described as $\lambda_{eff} = \lambda\cos\theta$ (λ : mean free path of escaping electrons) should decrease (see Fig. 6.4(a)) so that photoelectron intensities of both Ba3*d* and Sn3*d* states are expected to decrease.

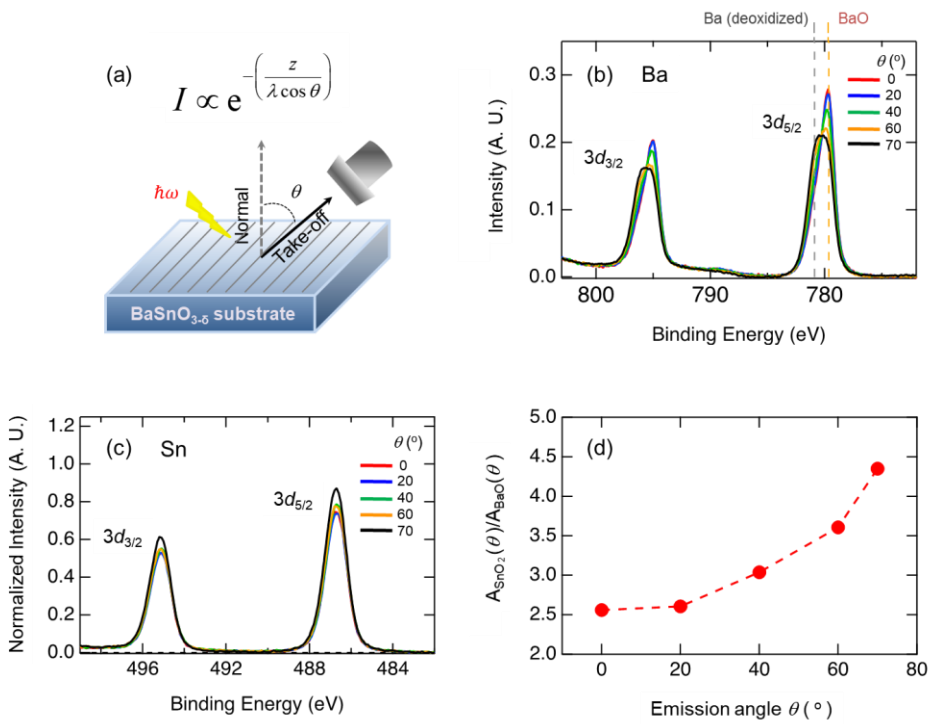

Figure 6.4 (a) A schematic plot illustrating the angle-dependent X-ray photoemission spectroscopy. Spectral intensity I is proportional to $\exp(-z/(\lambda\cos\theta))$, where z, λ, and θ correspond to the depth of atoms, the mean free path of escaping electrons, and the emission angle, respectively. Photoemission spectra of (b) Ba3*d* and (c) Sn3*d* states of $BaSnO_{3-\delta}$(001) substrates with various θ. (d) The area ratio of the $3d_{5/2}$ states of SnO_2 and BaO at each θ.

In Fig. 6.4(b), the spectra of Ba3*d* core-levels measured at various θ are displayed.

First, the spectra of Ba3*d* normalized with the total area after subtracting backgrounds show the change of spectral weight. The spectra exhibit $d_{5/2}$ and $d_{3/2}$ white lines due to the large spin-orbit splitting of a core hole. The spectral intensity is systematically reduced at higher θ as expected above. The low binding peak at $3d_{5/2}$ white lines is attributed to BaO (*197*) while the high binding peak is known to be deoxidized Ba (*198*) as well established in the core level spectra of $BaTiO_3$ (*199*, *200*). As can be seen in Fig. 6.4(b), upon θ being increased, the intensity of BaO peak (779.65 eV) decreases whereas that of deoxidized Ba peak (780.9 eV) increases. Because the spectrum using the high take-off angle is more surface sensitive, this information suggests that the deoxidized Ba atoms remain on the top-most surface. In other words, although 2×2 μm^2 surface morphology in the AFM image doesn't show any evidence of other residual particles except single-layer termination, there seem to exist a small amount of deoxidized Ba-like particles in the surface region. The residual deoxidized Ba might have formed possibly due to the Ba diffusion from the surface and/or inside bulk. Those deoxidized Ba-like particles could be reduced further in future works by optimizing etching and annealing conditions.

In order to understand what is the termination layer in the surface of $BaSnO_{3-\delta}$(001) substrates showing wide terraces and a single atomic step-edge, the core level spectra of Sn3*d* was also measured at the same time at each θ. Figure 6.4(c) displays the core level spectra of Sn3*d* after subtracting backgrounds, which could be well fitted by a pair of Voigt peaks where the Gaussian and Lorentzian broadening was fixed for each spectrum. A similar expression can be also used to describe the BaO spectra. The binding energy E_b for $Sn3d_{5/2}$ is 486.66 eV. In order to emphasize the relative intensity change depending on θ, the spectra are normalized with the spectral area of BaO (A_{BaO}), which is indeed the area of the Lorentzian peak located at E_b = 779.65 eV. As can be seen in Fig. 6.4(c), with increase of θ, the intensity of Sn3*d* spectra monotonically increases without any change of the spectral line shape.

To quantify the increase of the relative intensity, the ratio ($A_{SnO2}(\theta)/A_{BaO}(\theta)$) between the integrated areas of SnO_2 $A_{SnO2}(\theta)$ and of $A_{BaO}(\theta)$ is calculated at each θ in the case of $3d_{5/2}$ states, as displayed in Fig. 6.4(d). It is clearly seen that the ratio of $A_{SnO2}(\theta)/A_{BaO}(\theta)$ increases significantly at higher θ values, i.e., in the more surface sensitive regime. Since the mean free path of escaping electrons, of which kinetic energy is 700 eV (Ba3*d*) or 1000 eV (Sn3*d*), is ~10 Å, the intensity of top layer atoms increases exponentially. Therefore, it is concluded that the measured spectra verify that the termination surface layer mostly consists of SnO_2 rather than BaO. A similar analysis of angle-dependent XPS measurements has been reported also for the ZnO(0001) and $SrTiO_3$(001) substrates (*195*, *201*). Our works thus clearly show that the atomically flat surfaces in both $BaSnO_3$(001) and $BaSnO_{3-\delta}$(001) are terminated mostly with SnO_2 layers albeit having small residual deoxidized Ba-like particles. These substrates therefore could become useful platforms for developing $BaSnO_3$-based heterostructure in combination with other wide band gap oxides and for investigating possible realization of 2DEGs as predicted by recent theoretical works.

Chapter 7 Toward two-dimensional electron gases based on $BaSnO_3$(001) substrates

7.1 Overview

From the viewpoint of both fundamental physics and new device applications, one of the most exciting developments in oxide semiconductors can be the realization of 2DEGs at heterointerfaces. Such oxide interfaces can be a platform for observing a plethora of emergent and novel electronic states that have not been observed in any of the constituent materials. An archetypal example is the 2DEG realized at the interface of two band insulators, the $LaAlO_3/SrTiO_3$ heterointerface (*202*). On the other hand, the mechanism behind still seems to remain unclear (*203*). The reason for the lack of a definite consensus is closely associated with the characteristic of $SrTiO_3$ that can easily deviate from the oxygen stoichiometry (*182, 183, 204*). The study of 2DEGs at the heterointerface of the $BaSnO_3$ layer with a polar oxide could be useful as $BaSnO_3$ shows the thermal stability of oxygen with a low diffusion coefficient of oxygen (*76*). Moreover, $BaSnO_3$ has the same cubic perovskite structure as $SrTiO_3$, which could allow more chances for the growth of hetero-epitaxial films with other perovskite materials. Therefore, $BaSnO_3$ could be another exciting platform to realize the 2DEG at the heterointerfaces formed with other insulators.

7.2 Theoretical predictions for two-dimensional electron gases at heterointerfaces

Although there were earlier theoretical discussions on the possible 2DEGs at the heterojunction of $BaSnO_3$ with $KTaO_3$ or $LaAlO_3$ and $KTaO_3$ or $KNbO_3$ by Bjaalie et al. (*186*) and Fan et al., (*187*), respectively. It is in 2016 that Krishnaswamy et al. proposed

two major strategies in detail for the realization of 2DEGs in the $BaSnO_3$ system, i.e., a polar discontinuity and a modulation doping (*133*). One key requirement in the both strategies is to find an oxide material with higher conduction band minimum than $BaSnO_3$ in order to confine well electron carriers in the $BaSnO_3$ layer. Under this condition, free electrons will readily spill over into and remain in the $BaSnO_3$ layer. As the two strategies are quite important for future researches, we here explain more on the calculation results by Krishnaswamy et al. and the physics related.

Out of the two main strategies, doping due to a polar discontinuity is particularly appealing, as it is a form of "remote doping" without the direct introduction of dopants or chemical disorder. For the polar discontinuity doping, like the polar mechanism invoked for the $LaAlO_3/SrTiO_3$(001) system (*202*), a thin film of an $A^{3+}B^{3+}(O^{2-})_3$ polar oxide with relatively good lattice match, such as $LaInO_3$, on the SnO_2-terminated (001) surface of a $BaSnO_3$ single crystal (nonpolar oxide) could lead to the formation of 2DEGs (Fig. 7.1(a)). As long as the band offset of the polar material is high enough not to spill over the carriers at the interface, the maximum 2D carrier density $n_{2D,max}$ expected at the interface should be 0.5 electron/(in-plane unit cell), which corresponds to $n_{2D,max} = 2.9 \times 10^{14}$ cm^{-2}.

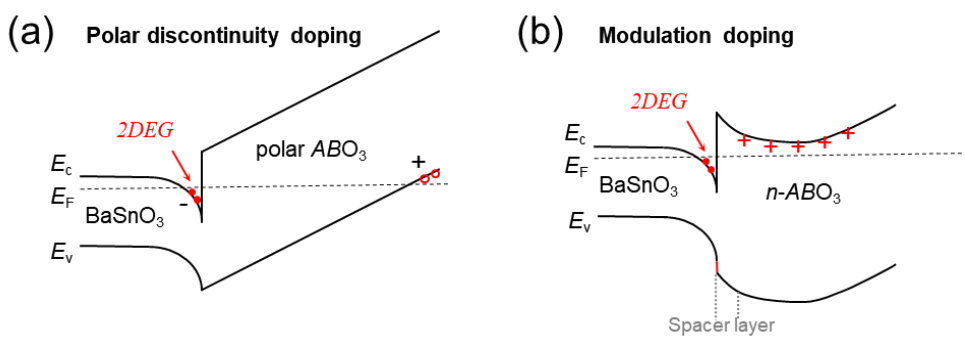

Figure 7.1 (a) A band diagram depicting polar discontinuity doping between a nonpolar $BaSnO_3$ and a polar ABO_3. (b) A band diagram describing modulation doping at a nonpolar heterointerface.

In a modulation doping as depicted in Fig. 7.1(b), dopants are introduced in a barrier material whose conduction band minimum is located higher than that of $BaSnO_3$. Electrons from the dopants can transfer from the barrier material into the $BaSnO_3$ layer to form 2DEGs at the interface. An insulating spacer layer should be grown to enhance the separation between electrons and ionized donors. These 2DEGs are then separated from the dopants and therefore less prone to impurity scattering (*205, 206*). The most viable dopant profile could be a delta doping, where the dopants are introduced as a sheet in the barrier material at a distance *d* away from the interface (*207, 208*). Krishnaswamy et al. indeed calculated the n_{2D} as a function of dopant sheet concentrations based on the band offsets of barrier materials ($SrTiO_3$, $LaInO_3$, $KTaO_3$) (*133*). The maximum confined carrier density $n_{2D,max}$ has generally increased as the conduction band offsets (CBOs) of those materials increases.

Figure 7.2 replots the calculation results of Krishnaswamy et al. (*133*), summarizing the theoretically used CBOs of the barrier materials and the resultant $n_{2D,max}$ induced in the $BaSnO_3$ layer. Moreover, a_c, a_{pc}, and lattice misfits of the barrier materials to $BaSnO_3$ are also plotted. All the $n_{2D,max}$ was extracted from the n_{2D} *vs*. CBO plot (Fig. 5 in (*133*)). Note that the CBOs used in the calculations were generally larger than those from the experimental results (Fig. 7.3**)** because the calculation employed a smaller band gap = 2.4 eV of $BaSnO_3$ from the HSE06 hybrid functional while the experimental E_g is ~3.0 eV. In turn, the predicted $n_{2D,max}$ can overestimate the real experimental data.

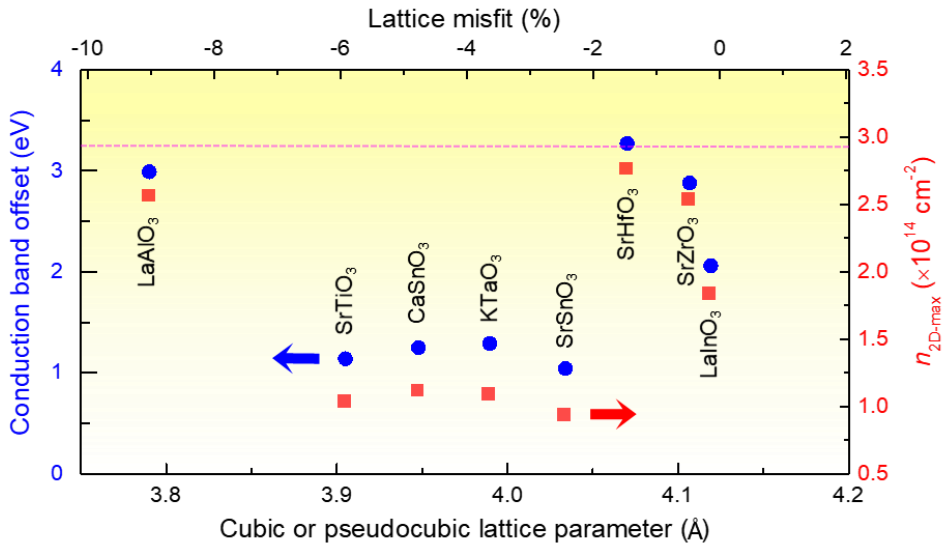

Figure 7.2 On the basis of the theoretical results of Schrödinger-Poisson simulations in Reference (*133*), the conduction band offsets (*blue circles*) and $n_{2D,max}$ (*red squares*) between $BaSnO_3$ and other ABO_3 barrier materials are replotted as a function of cubic or pseudocubic lattice parameters. The dashed magenta line indicates the $n_{2D,ideal}$, where all the electrons provided by polar discontinuity doping (0.5 electrons per in-plane unit cell) are confined in $BaSnO_3$.

7.3 Experimental situation

Whereas there are ample predictions from theory, the related experimental activity is still nascent. A necessary step is to grow a heteroepitaxial film in which $BaSnO_3$ works as a channel material and the other joint material as a barrier material. For this purpose, the candidate barrier material should have (i) a higher conduction band minimum than does $BaSnO_3$ and (ii) a good lattice match with $BaSnO_3$. Experiments should be undertaken to determine the CBOs between $BaSnO_3$ and the candidate materials. The use of accurate E_g or CBOs can provide more accurate estimation of n_{2D} at the interface.

Chambers et al. (*101*) recently reported, using photoemission spectroscopy, that the

conduction band minimums of $SrTiO_3$ and $LaAlO_3$ are higher than the conduction band minimum of $BaSnO_3$ by 0.42 and 3.72 eV, respectively. These authors thus discussed the possibility of 2DEGs at the $SrTiO_3/BaSnO_3$ interface by modulation doping or at the $LaAlO_3/BaSnO_3$ interface by polar discontinuity doping. In addition to this research, it is worthwhile to list promising candidate materials on the basis of their band alignments. Figure 7.3 presents the summary of experimental information on the band alignments of candidate materials to provide some guidance for future research. For details on how Fig. 7.3 was generated, please refer to Chapter 7.4..

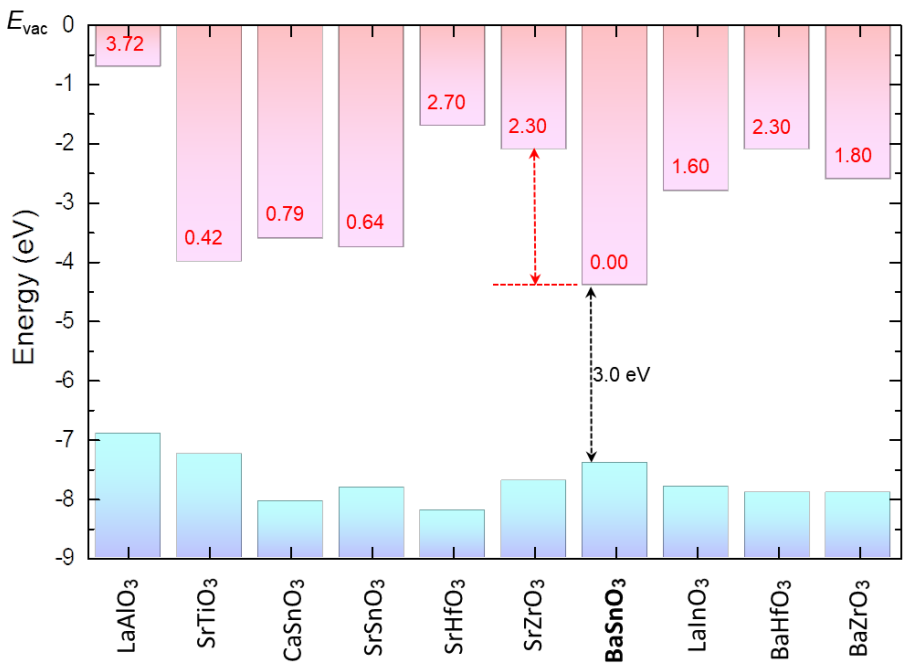

Figure 7.3 Summary of band alignments of various perovskite oxides, including $BaSnO_3$, as extracted from the available experimental data. The numbers reported in red are the conduction band offsets between $BaSnO_3$ and various perovskite oxides and reflect the position of the conduction band minimum.

In 2016, Kim et al. (*134*) reported a significant increase in conductivity after $LaInO_3$ films were grown on top of BLSO films (0.1% < La < 0.5%), which in turn were grown on a $BaSnO_3$ buffer (110 nm)/$SrTiO_3$(001) substrate. In contrast, there was no increase in the case of undoped films. The authors claimed that the conductivity increase is due to the formation of a conducting interface by polar discontinuity doping at the $LaInO_3$-BLSO interface and that such an increase can occur only when the E_F of $BaSnO_3$ increases due to (low) La doping. However, the dislocations in the low-La-doped $BaSnO_3$ film may have decreased the original E_F to make the film p-type. Therefore, whether the 2DEG actually formed at the polar interface between insulating $BaSnO_3$ and $LaInO_3$ awaits more extensive exploration.

To summarize the experimental situation, the growth of large-area and homogeneous thin films without dislocations or defects by the use of, e.g., MBE with a proper substrate like $BaSnO_3$ will be necessary for elucidating the interfacial physics in the $BaSnO_3$-based heterostructure. For this, it will be useful to utilize a $BaSnO_3$(001) substrate with an atomically flat surface and a terrace-step structure. As we have succeeded in obtaining such a structure at the surface of a highly insulating $BaSnO_3$(001) substrate, it will allow researchers to realize 2DEGs at the interfaces of $BaSnO_3$ layers in perovskite stannates.

7.4 How to determine band alignment in Fig. 7.3

In order to summarize experimental band alignment of $BaSnO_3$ and candidate materials for a reference for future researches, we first note that the known electron affinity of $SrTiO_3$ (4.0 eV) (*209*) was used to determine its conduction band minimum with respect to the vacuum level. Chambers et al. indeed determined accurately the valence band offsets (VBO) of $SrTiO_3$ and $LaAlO_3$ with respect to $BaSnO_3$ (*101*). They then estimated the CBOs of $SrTiO_3$ and $LaAlO_3$ with respect to $BaSnO_3$ in combination with the known E_g of $SrTiO_3$

and $LaAlO_3$. In Fig. 7.3, we used the known information as it is to plot the band alignments of $SrTiO_3$, $LaAlO_3$, and $BaSnO_3$.

To determine the band alignment of $SrZrO_3$, the VBO between $SrTiO_3$ and $SrZrO_3$ as measured by photoelectron spectroscopy and the known E_g (5.6) of $SrZrO_3$ (*115*) was used. For the cases of $SrSnO_3$ and $CaSnO_3$, we first noticed that Dorenbos et al. provided the band alignments of $SrSnO_3$, $CaSnO_3$, and $BaSnO_3$ as estimated by the chemical shift model and the experimental reflection, luminescence and absorption spectra (*210*). However, the proposed E_g of the three compounds were overestimating the more accurate experimental values determined by optical transmission measurements by 0.5 – 0.75 eV. Therefore, we only adopted the VBOs and CBOs of $SrSnO_3$ and $CaSnO_3$ with respect to $BaSnO_3$ from the results by Dorenbos et al. to draw the band alignments of $SrSnO_3$ and $CaSnO_3$ in Fig. 7.3. For the band alignment of $LaInO_3$, we used recent reports by Kim et al, in which the CBO of $LaInO_3$ was determined by the estimation of a tunneling barrier in the *I-V* measurements (*134*). The VBO of $LaInO_3$ was determined by the E_g of 5.0 eV as reported by Kim et al. It should be reiterated that the reported E_g = 5.0 eV in the $LaInO_3$ film is clearly different from that of the single crystal (E_g = 4.3 eV) (*116*), presumably due to the strain effect from the substrate. Therefore, the E_g and/or dielectric properties of a $LaInO_3$ thin film should be investigated for each substrate material employed in the film growth for, e.g., accurate determination of n_{2D} in Fig. 7.3.

For drawing band alignments of $SrHfO_3$, $BaHfO_3$, and $BaZrO_3$, we first used the experimental fact that $SrTiO_3$ has almost the same electron affinity with Si (*211*). The VBO between $SrHfO_3$ and Si was indeed determined by the photoelectron spectroscopy (*112*). We used the VBO of $SrHfO_3$ with respect to Si and its known E_g to draw the band alignment of $SrHfO_3$ in Fig. 7.3. Similarly, the VBOs among $SrHfO_3$, $BaHfO_3$, and $BaZrO_3$ were determined by XPS and X-ray absorption spectroscopy (*118*). We used the VBOs of

the three materials and the E_g to draw the band alignments of $BaHfO_3$, and $BaZrO_3$ (*118*, *122*).

7.5 Structural and dielectric properties of epitaxial $LaInO_3$ films

In order to study polar oxide interface between SnO_2-terminated $BaSnO_3$(001) and another ABO_3 material, the author chosen $LaInO_3$ as a polar barrier material due to its similar lattice constants (~4.120 Å) (*116*). As structural and dielectric properties of epitaxial $LaInO_3$ films have been rarely reported, the author will first present the epitaxial growth of $LaInO_3$ films and its structural properties. $LaInO_3$ films were deposited on TiO_2-terminated $SrTiO_3$(001) and SnO_2-terminated $BaSnO_3$(001) substrates by pulsed laser deposition with a KrF excimer laser (λ = 248 nm) with a laser fluence of ~1.0 J cm^{-2} using $LaInO_3$ polycrystalline target. The deposition was made in an O_2 pressure of 100 mTorr at 790 ^oC.

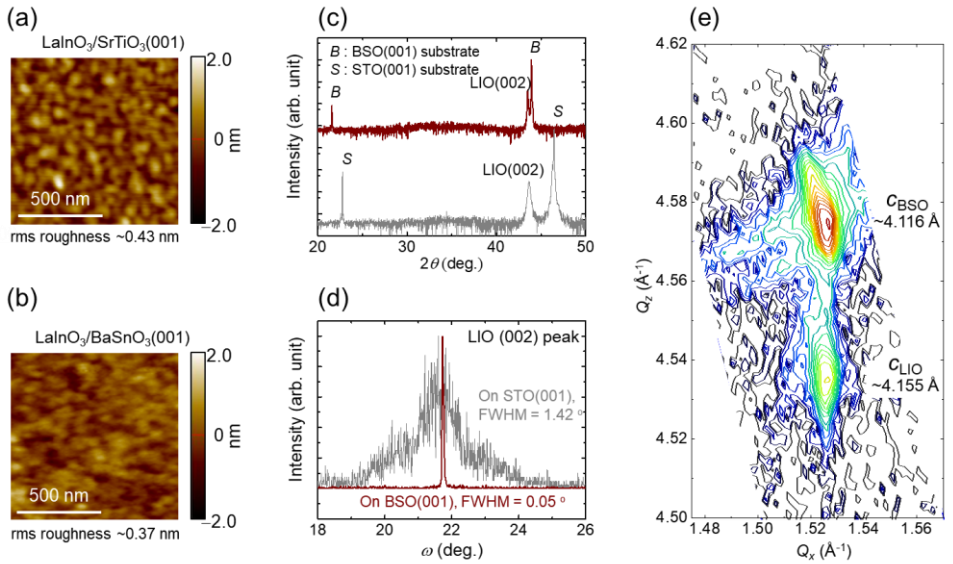

Figure 7.4 Surface morphology of 90 nm thick $LaInO_3$ films grown on (a) $SrTiO_3(001)$ and (b) $BaSnO_3(001)$ substrates. (c) X-ray θ-2θ scan results of $LaInO_3/SrTiO_3(001)$ and $LaInO_3/BaSnO_3(001)$ films. (d) The rocking curves measured at the 2θ angle of (002) Bragg peak of $LaInO_3$ films grown on $SrTiO_3(001)$ (grey) and $BaSnO_3(001)$ (red) substrates. (e) Reciprocal space maps of the (103) reflection for the $LaInO_3/BaSnO_3(001)$ films.

Figures 7.4(a) and (b) show AFM topography of 90 nm thick $LaInO_3/SrTiO_3(001)$ and $LaInO_3/BaSnO_3(001)$ films. Their maximum height difference and rms roughness were found to be about 2.0 nm and 0.37-0.43 nm, respectively, demonstrating that smooth films could be grown on $SrTiO_3(001)$ and $BaSnO_3(001)$ substrates. The X-ray θ-2θ scans of $LaInO_3/BaSnO_3(001)$ and $LaInO_3/SrTiO_3(001)$ showed that $LaInO_3$ films were grown along (00*l*) directions without undesired phases (Fig. 7.4(c)). Figure 7.4(d) shows the rocking curve measured at the 2θ angle of (002) Bragg peak of $LaInO_3$ films grown on $BaSnO_3(001)$ and $SrTiO_3(001)$ substrates. Upon fitting with the pseudo-Voigt function, FWHM of 0.05 ° and 1.42 ° were obtained, respectively. These results prove high crystallinity of $LaInO_3$ films grown on $BaSnO_3(001)$ substrates owing to its lattice matching properties. Figure 7.4(d) shows RSM of the $LaInO_3/BaSnO_3(001)$, showing that

the Q_x of $LaInO_3$ is nearly same as that of $BaSnO_3$, while the Q_z of $LaInO_3$ spot is clearly smaller than that of $BaSnO_3$. From this, it is estimated that $LaInO_3$ film has a of 4.116 Å, while c = 4.155 Å of the film is increased by +0.95 % as compared with that of $BaSnO_3$(001) substrate. This implies that the in-plane of $LaInO_3$ film is subject to compressive strain to have the similar a value with $BaSnO_3$(001) substrate, while its c-axis is expanded than that of the substrate.

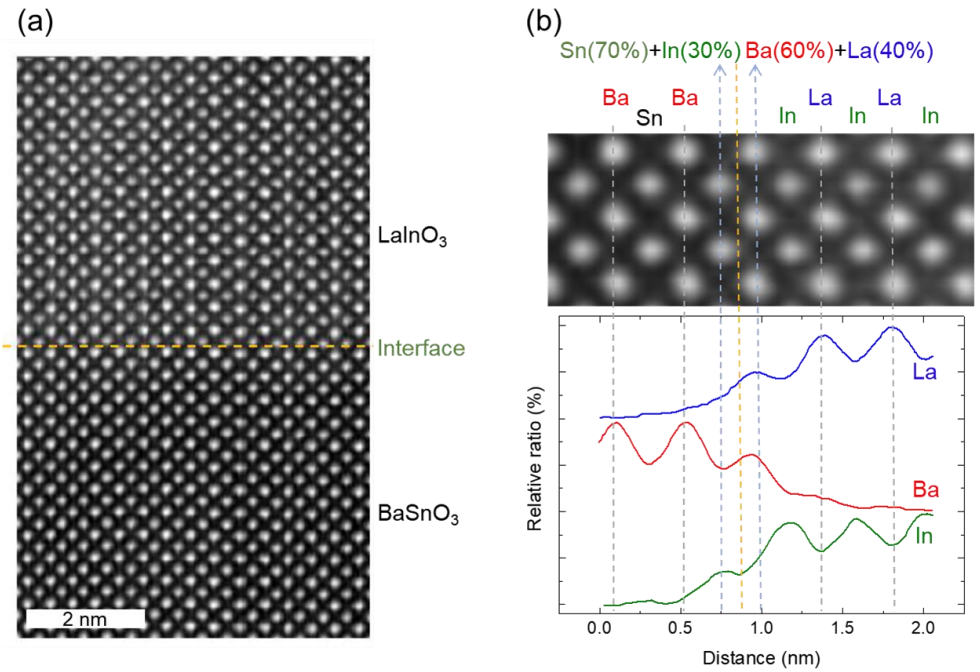

Figure 7.5 (a) An HAADF-STEM (high-angle annular dark-field-scanning transmission electron microscopy) image at the interface of $LaInO_3/BaSnO_3$(001) films. Ba, Sn, La, and In ions are brightest. (b) EELS (electron energy loss spectroscopy) profiles for chemical analysis at the interface of $LaInO_3/BaSnO_3$(001) films. Dotted orange line will be likely an interface between lanthanum oxide and tin oxide. (e) Reciprocal space maps of the (103) reflection for the $LaInO_3/BaSnO_3$ (001) films.

In order to invesitage the local structural properties, the TEM measurements were performed. Figure 7.5(a) shows a HAADF-STEM image of $LaInO_3/BaSnO_3(001)$, indicating that there are no dislocations or grain boundaries. With such a good lattice match between $LaInO_3$ and $BaSnO_3$, the interface couldn't be distinguished well, supporting that the high quality epitaxial $LaInO_3$ film are realized on the $BaSnO_3(001)$ substrate. To understand the interface terminations, we examined the interfaces with atomic-resolution electron energy loss spectroscopy (EELS) performed in a scanning transmission electron microscope (STEM), as shown in Fig. 7.5(b). We find intermixing layer of ~1 u.c. at the $LaInO_3/BaSnO_3(001)$ interface indicating that the $LaInO_3/BaSnO_3(001)$ interface is more abrupt than $LaAlO_3/SrTiO_3$ interface (*212*). The origin of intermixing between Ba and La and Sn and In could be understood from the low formation energies of La_{Ba} and In_{Sn} (*173*, *213*).

In order to understand dielectric properties of epitaxial $LaInO_3$ films, we measured 40 nm-thick $LaInO_3$ dielectric layer which was sandwiched between $(Ba,La)SnO_3$ contacts with an area of 100×100 μm^2. Figure 7.6(a) shows measured ε_r and $\tan\delta$. First, the decrease of ε_r and the increase of $\tan\delta$ at high frequency range could be understood by interface charge traps. Second, at low frequency range, ε_r of $LaInO_3$ films grown on $SrTiO_3(001)$ and $BaSnO_3(001)$ substrates is 24 and ~24-27, respectively. These values are similar as ε_r of ~23-24 reported for $LaInO_3$ single crystals (*116*). It is noted that ε_r of 24-27 is cleary smaller thant that of 38.7 reported for an epitaxial $LaInO_3$ film grown on $(Ba,La)SnO_3/SrTiO_3(001)$ (*143*).

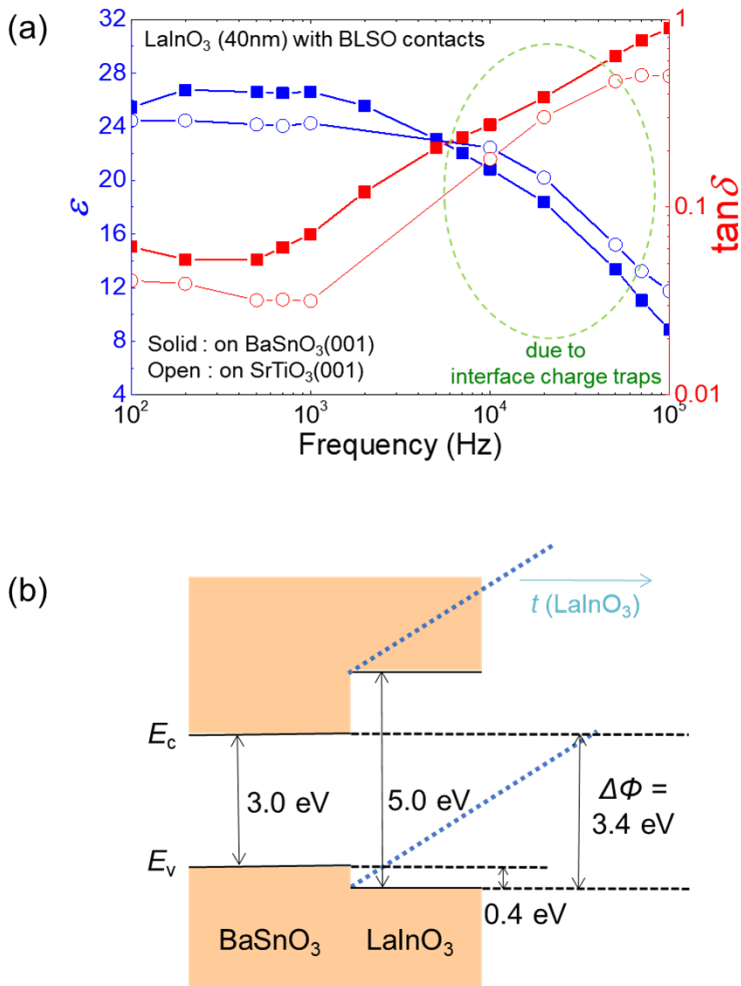

Figure 7.6 (a) Frequency dependent-dielectric constant (ε_r) (left) and dissipation (right) of 90nm thick $LaInO_3$ films between (Ba,La)SnO_3 contacts on $BaSnO_3$(001) (solid symbols) and $SrTiO_3$(001) (open symbols) substrates. (b) The schematic of the band alignment between $BaSnO_3$ and $LaInO_3$. $\Delta\phi$ is potential build-up to induce the electronic reconstruction.

The exact value of ε_r could be utilized to estimate the critical thickness (t_c) for the metal-insulator transiton of $LaInO_3/BaSnO_3(001)$ heterostructure. In the case of $LaAlO_3/SrTiO_3(001)$, the linear decrease of formation energy of surface V_O with increase of $LaAlO_3$ thickness could expalin the t_c for the metal-insulator transition (*146, 214*). The intrinsic doping mechanism for $LaInO_3/BaSnO_3(001)$ might be explained by the polarization of $LaInO_3$. $LaInO_3$ may have a formal polarization $P_{LIO} = 0.5e/S = 0.472$ C m^{-2} (S = in-plane unit cell of the interface), whereas in nonpolar $BaSnO_3$, $P_{BSO} = 0$, resulting in an appearance of an built-in polar electric field $E_{LIO} = P_{LIO}/(\varepsilon_0\varepsilon_{r,LIO})$, where ε_0 and $\varepsilon_{r,LIO}$ are the vacuum permittivity and dielectric constant of $LaInO_3$, respectively. E_{LIO} might bend the electronic bands as shown in Fig. 7.6(b). t_c can be written as $\Delta\phi/E_{LIO} = \varepsilon_0\varepsilon_{r,LIO}$ $\Delta\phi/(eP_{LIO})$ which predicts an t_c of ~3.6 u.c.. Note that $\Delta\phi$ is the energy difference between valence band maximum of $LaInO_3$ and conduction band minimum of $BaSnO_3$ as shown in Fig. 7.6(b). At a thickness of t_c, the valence bands of $LaInO_3$ at the surface could reach the conduction bands of $BaSnO_3$ at the interface, resulting in metallic interface. Above t_c, electrons can be transffered continuously from the surface to the interface.

In order to check the electronic properties at the $LaInO_3/BaSnO_3(001)$ interface, we grew 6 u.c. of $LaInO_3$ films on SnO_2-terminated $BaSnO_3(001)$ substrates by PLD method, which is expected to be similar to the n-type interface of 2DEGs. Figure 7.7 shows the surface morphology before and after deposition of $LaInO_3$ layers. The surface is atomically flat and terminated with one single termination before deposition while an atomically well defined single terminated step-terrace structure is conserved even after growth. Subsequently, the transport property was examined by four-probe measurements with a distance between electrodes of ~1 mm. However, the grown sample was highly insulating at room temperature when the silver epoxy was used on the surface and the interface. It is worthwhile to investigate the effect of donor doping, i.e., La^{3+} ion on Ba^{2+} site or V_O, controlling the Fermi level. In addition, layer by layer growth by laser MBE or various

contact method, i.e., wire bonding or e-beam lithography after Ar ion milling, could be effective for realization of 2DEGs.

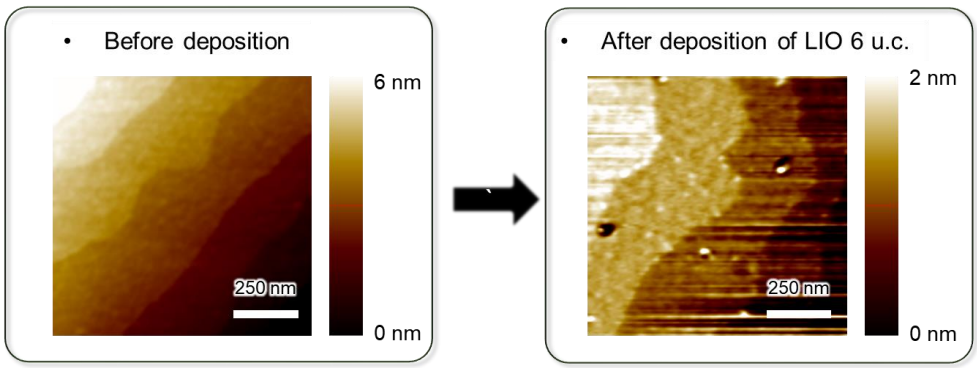

Figure 7.7 Surface morphology of SnO_2-terminated $BaSnO_3$(001) substrate (left) and 6 unit cell of $LaInO_3$ grown on SnO_2-terminated $BaSnO_3$(001) substrate (right). The step-and-terrace structure is clearly visible before and after deposition of $LaInO_3$ 6 u.c..

7.6 Outlook for 2DEGs at $ABO_3/BaSnO_3$(001) interfaces

Various potential applications await researcher's attentions. Figure 7.8 plots the expected μ behavior of the electron-doped $BaSnO_3$ system with available experimental data at 2 K as a function of carrier density n. The expected μ was calculated from the ionized impurity scattering model in a degenerate doping regime and plotted as a dashed violet line. The $ABO_3/BaSnO_3$ interfaces can hold 2DEGs by either modulation or polar discontinuity doping, thereby paving the way for the investigation of quantum phenomena. First of all, number of phonons at such a low temperature will be naturally reduced, resulting in almost zero phonon scattering. Then, one can investigate the μ in a low n region less than 10^{18} cm^{-3}. According to the ionized impurity scattering model, μ can increase with decrease of n due to the decreased number of scattering centers. In this regime, one can pursue to observe the quantum Hall effect in the 2 DEG system at the $ABO_3/BaSnO_3$ heterostructures. Moreover,

the quantum oscillation could be observed to allow the understanding fundamental properties of the 2DEG system as in the $LaAlO_3/SrTiO_3$ heterostructures (*206, 208, 215*). Therefore, by employing the modulation or polar discontinuity doping, the fascinating phenomena of quantum oscillation and quantum Hall effects await for discoveries in the $BaSnO_3$ system.

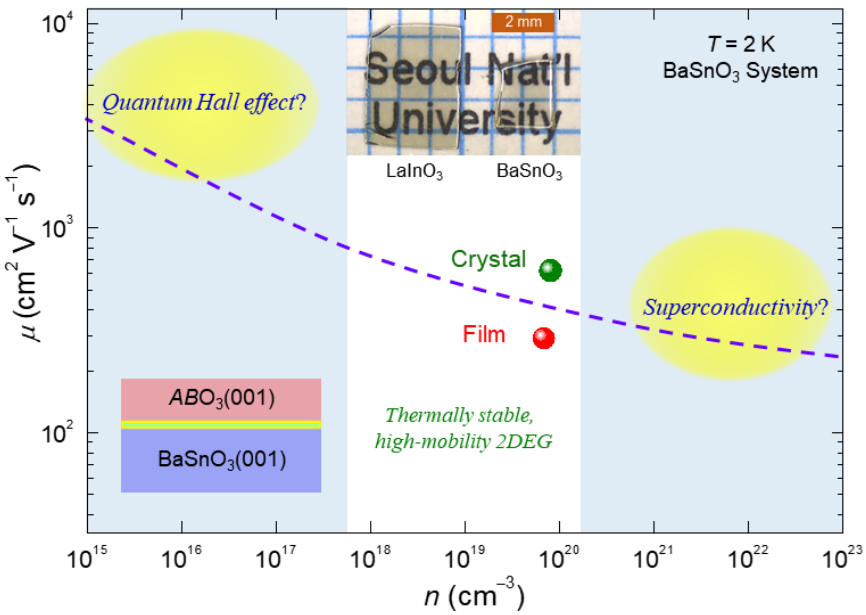

Figure 7.8 Expected electron mobility μ behavior and anticipated physical phenomena of the doped $BaSnO_3$ system at low temperatures. The dashed line represents the predicted μ from ionic dopant scattering; μ can increase more in a nondegenerate regime. The solid green and red circles indicate the best currently available experimental data for $(Ba,La)SnO_3$ single crystals and thin films, respectively. Two-dimensional electron gases formed at the heterointerface between $BaSnO_3$ and other ABO_3 materials may exhibit fascinating quantum phenomena such as the quantum Hall effect and superconductivity in low- and high-doping regimes, respectively. To illustrate the importance of using the proper substrates, we show optical images of transparent $LaInO_3$ (t = 300 μm) and $BaSnO_3$ (t = 700 μm) crystals grown by our research group (*top middle*).

Another fascinating phenomenon will be the superconductivity at the $BaSnO_3$ system, which are likely to occur at a high *n* regime. Based on the carrier accumulation by electrical double layer (EDL) transistor as well as modulation and polar discontinuity doping, interfacial superconductivity was recently emerged in the channel made of similar wide band-gap oxides, $SrTiO_3$, $KTaO_3$, and heterointerface of $LaAlO_3/SrTiO_3$ (*207, 216-218*). Therefore, we also anticipate superconductivity in the $BaSnO_3$ based heterostructure by accumulation of carriers by EDL and/or modulation or polar discontinuity doping.

Bibliography

1. D. S. Ginley, C. Bright, Transparent conducting oxides. *MRS Bull.* **25**, 15-18 (2000).
2. T. Minami, New n-type transparent conducting oxides. *MRS Bull.* **25**, 38-44 (2000).
3. A. J. Freeman, K. R. Poeppelmeier, T. O. Mason, R. P. H. Chang, T. J. Marks, Chemical and thin-film strategies for new transparent conducting oxides. *MRS Bull.* **25**, 45-51 (2000).
4. H. Ohta *et al.*, Frontier of transparent oxide semiconductors. *Solid-State Electron.* **47**, 2261-2267 (2003).
5. H. Hosono, Recent progress in transparent oxide semiconductors: Materials and device application. *Thin Solid Films* **515**, 6000-6014 (2007).
6. K. Nomura *et al.*, Room-temperature fabrication of transparent flexible thin-film transistors using amorphous oxide semiconductors. *Nature* **432**, 488-492 (2004).
7. T. Kamiya, K. Nomura, H. Hosono, Present status of amorphous In–Ga–Zn–O thin-film transistors. *Sci. Technol. Adv. Mater.* **11**, 044305 (2010).
8. S. Calnan, A. N. Tiwari, High mobility transparent conducting oxides for thin film solar cells. *Thin Solid Films* **518**, 1839-1849 (2010).
9. H. Hosono, H. Ohta, K. Hayashi, M. Oritaa, M. Hirano, Near-UV emitting diodes based on a transparent p–n junction composed of heteroepitaxially grown p-$SrCu_2O_2$ and n-ZnO. *J. Cryst. Growth* **237-239**, 496-502 (2002).
10. S. Das, V. Jayaraman, SnO_2: A comprehensive review on structures and gas sensors. *Prog. Mater. Sci.* **66**, 112-255 (2014).
11. Z. Wang, P. K. Nayak, J. A. Caraveo-Frescas, H. N. Alshareef, Recent developments in p-type oxide semiconductor materials and devices. *Adv. Mater.* **28**, 3831-3892 (2016).
12. N. Preissler, O. Bierwagen, A. T. Ramu, J. S. Speck, Electrical transport, electrothermal transport, and effective electron mass in single-crystalline In_2O_3 films. *Phys. Rev. B* **88**, 085305 (2013).
13. S. Nakao *et al.*, High mobility exceeding 80 $cm^2V^{-1}s^{-1}$ in polycrystalline Ta-doped SnO_2 thin films on glass using anatase TiO_2 seed layers. *Appl. Phys. Express* **3**, 031102 (2010).
14. Q. Nian, M. Y. Zhang, B. D. Schwartz, G. J. Cheng, Ultraviolet laser crystallized ZnO:Al films on sapphire with high Hall mobility for simultaneous enhancement of conductivity and transparency. *Appl. Phys. Lett.* **104**, 201907 (2014).
15. E. Sachet *et al.*, Dysprosium-doped cadmium oxide as a gateway material for mid-infrared plasmonics. *Nature Mater.* **14**, 414-420 (2015).
16. K. Sasaki *et al.*, Device-quality β-Ga_2O_3 epitaxial films fabricated by ozone molecular beam epitaxy. *Appl. Phys. Express* **5**, 035502 (2012).
17. J. Son *et al.*, Epitaxial $SrTiO_3$ films with electron mobilities exceeding 30,000 $cm^2V^{-1}s^{-1}$. *Nature Mater.* **9**, 482-484 (2010).

18. S. Raghavan *et al.*, High-mobility $BaSnO_3$ grown by oxide molecular beam epitaxy. *APL Mater.* **4**, 016106 (2016).

19. S. J. Wen *et al.*, Electrical-properties of pure In_2O_3 and Sn-doped In_2O_3 single-crystals and ceramics. *J. Solid State Chem.* **101**, 203-210 (1992).

20. M. Nagasawa, S. Shionoya, S. Makishima, Vapor reaction growth of SnO_2 single crystals and their properties. *Jpn. J. Appl. Phys.* **4**, 195-202 (1965).

21. W. Lin *et al.*, Hydrothermal growth of ZnO single crystals with high carrier mobility. *Crystal Growth & Design* **9**, 4378-4383 (2009).

22. F. P. Koffyberg, Electronic conduction and defect equilibria in CdO single crystals. *J. Solid State Chem.* **2**, 176-181 (1970).

23. T. Oishi, Y. Koga, K. Harada, M. Kasu, High-mobility β-Ga_2O_3(201) single crystals grown by edge-defined film-fed growth method and their Schottky barrier diodes with Ni contact. *Appl. Phys. Express* **8**, 031101 (2015).

24. S. Ohta, T. Nomura, H. Ohta, K. Koumoto, High-temperature carrier transport and thermoelectric properties of heavily La- or Nb-doped $SrTiO_3$ single crystals. *J. Appl. Phys.* **97**, 034106 (2005).

25. H. J. Kim *et al.*, High mobility in a stable transparent perovskite oxide. *Appl. Phys. Express* **5**, 061102 (2012).

26. I. Hamberg, C. G. Granqvist, Evaporated Sn-doped In_2O_3 films: Basic optical properties and applications to energy-efficient windows. *J. Appl. Phys.* **60**, R123 (1986).

27. F. Simonis, M. Vanderleij, C. J. Hoogendoorn, Physics of doped tin dioxide films for spectral-selective surfaces. *Sol. Energy Mater.* **1**, 221-231 (1979).

28. A. E. Rakhshani, Y. Makdisi, H. A. Ramazaniyan, Electronic and optical properties of fluorine-doped tin oxide films. *J. Appl. Phys.* **83**, 1049 (1998).

29. C. Agashe, Efforts to improve carrier mobility in radio frequency sputtered aluminum doped zinc oxide films. *J. Appl. Phys.* **95**, 1911 (2004).

30. K. Ellmer, Resistivity of polycrystalline zinc oxide films: current status and physical limit. *J. Phys. D: Appl. Phys.* **34**, 3097-3108 (2001).

31. A. Wang *et al.*, Indium-cadmium-oxide films having exceptional electrical conductivity and optical transparency: clues for optimizing transparent conductors. *Proc. Nat. Acad. Sci. U.S.A.* **98**, 7113-7116 (2001).

32. Y. Zhu, R. J. Mendelsberg, J. Zhu, J. Han, A. Anders, Dopant-induced band filling and bandgap renormalization in CdO : In films. *J. Phys. D: Appl. Phys.* **46**, 195102 (2013).

33. M. Orita, H. Ohta, M. Hirano, H. Hosono, Deep-ultraviolet transparent conductive β-Ga_2O_3 thin films. *Appl. Phys. Lett.* **77**, 4166 (2000).

34. J. B. Varley, J. R. Weber, A. Janotti, C. G. Van de Walle, Oxygen vacancies and donor impurities in β-Ga_2O_3. *Appl. Phys. Lett.* **97**, 142106 (2010).

35. T. Kamiya, K. Nomura, H. Hosono, Origins of High Mobility and Low Operation Voltage of Amorphous Oxide TFTs: Electronic Structure, Electron Transport, Defects and Doping. *Journal of Display Technology* **5**, 273-288 (2009).

36. D. H. Lee, K. Nomura, T. Kamiya, H. Hosono, Metal-semiconductor field-effect

transistor made using amorphous In-Ga-Zn-O channel and nottom Pt Schottky contact structure at 200 ºC. *Ecs Solid State Letters* **1**, Q8-Q10 (2012).

37. K. A. Müller, H. Burkard, $SrTiO_3$: An intrinsic quantum paraelectric below 4 K. *Phys. Rev. B* **19**, 3593-3602 (1979).

38. K. van Benthem, C. Elsässer, R. H. French, Bulk electronic structure of $SrTiO_3$: Experiment and theory. *J. Appl. Phys.* **90**, 6156 (2001).

39. M. Marques *et al.*, Full-relativistic calculations of the $SrTiO_3$ carrier effective masses and complex dielectric function. *Appl. Phys. Lett.* **82**, 3074 (2003).

40. H. J. Kim *et al.*, Physical properties of transparent perovskite oxides (Ba,La)SnO_3 with high electrical mobility at room temperature. *Phys. Rev. B* **86**, 165205 (2012).

41. T. Minami, Transparent conducting oxide semiconductors for transparent electrodes. *Semicond. Sci. Technol.* **20**, S35-S44 (2005).

42. H. He *et al.*, First-principles study of the structural, electronic, and optical properties of Ga_2O_3 in its monoclinic and hexagonal phases. *Phys. Rev. B* **74**, 195123 (2006).

43. T. Kamiya, K. Nomura, H. Hosono, Electronic structure of the amorphous oxide semiconductor a-$InGaZnO_{4-x}$: Tauc-Lorentz optical model and origins of subgap states. *Phys. Status Solidi A* **206**, 860-867 (2009).

44. G. J. Exarhos, X.-D. Zhou, Discovery-based design of transparent conducting oxide films. *Thin Solid Films* **515**, 7025-7052 (2007).

45. A. Walsh, J. L. Da Silva, S. H. Wei, Multi-component transparent conducting oxides: progress in materials modelling. *J. Phys.: Condens. Matter* **23**, 334210 (2011).

46. O. Mryasov, A. Freeman, Electronic band structure of indium tin oxide and criteria for transparent conducting behavior. *Phys. Rev. B* **64**, 233111 (2001).

47. A. Kumar, C. W. Zhou, The race to teplace tin-doped indium oxide: which material will win? *Acs Nano* **4**, 11-14 (2010).

48. B. Bayraktaroglu, K. Leedy, R. Bedford, High temperature stability of postgrowth annealed transparent and conductive ZnO:Al films. *Appl. Phys. Lett.* **93**, 022104 (2008).

49. W. Ping *et al.*, Instability induced by ultravioletlLight in ZnO thin-film transistors. *IEEE Trans. Electron Devices* **61**, 1431-1435 (2014).

50. B. Claflin, D. C. Look, S. J. Park, G. Cantwell, Persistent n-type photoconductivity in p-type ZnO. *J. Cryst. Growth* **287**, 16-22 (2006).

51. A. Janotti, C. G. Van de Walle, Fundamentals of zinc oxide as a semiconductor. *Rep. Prog. Phys.* **72**, 126501 (2009).

52. E. Fortunato, P. Barquinha, G. Goncalves, L. Pereira, R. Martins, High mobility and low threshold voltage transparent thin film transistors based on amorphous indium zinc oxide semiconductors. *Solid-State Electron.* **52**, 443-448 (2008).

53. Y. Oana, Current and future technology of low-temperature poly-Si TFT-LCDs. *J. Soc. Info. Display* **9**, 169-172 (2001).

54. A. Kojima, K. Teshima, Y. Shirai, T. Miyasaka, Organometal halide perovskites as visible-light sensitizers for photovoltaic cells. *J. Am. Chem. Soc.* **131**, 6050-

6051 (2009).

55. M. Liu, M. B. Johnston, H. J. Snaith, Efficient planar heterojunction perovskite solar cells by vapour deposition. *Nature* **501**, 395-398 (2013).

56. L. F. Mattheiss, E. M. Gyorgy, D. W. Johnson, Superconductivity above 20 K in the Ba-K-Bi-O system. *Phys. Rev. B* **37**, 3745-3746 (1988).

57. R. J. Cava *et al.*, Superconductivity near 30-K without copper - the $Ba_{0.6}K_{0.4}BiO_3$ perovskite. *Nature* **332**, 814-816 (1988).

58. R. J. Cava *et al.*, Superconductivity at 3.5 K in $BaPb_{0.75}Sb_{0.25}O_3$ - Why is T_c so low? *Nature* **339**, 291-293 (1989).

59. Y. Tokura, Y. Tomioka, Colossal magnetoresistive manganites. *J. Magn. Magn. Mater.* **200**, 1-23 (1999).

60. G. H. Haertling, Ferroelectric ceramics: History and technology. *J. Am. Ceram. Soc.* **82**, 797-818 (1999).

61. J. Ryu, A. V. Carazo, K. Uchino, H.-E. Kim, Magnetoelectric properties in piezoelectric and magnetostrictive laminate composites. *Jpn. J. Appl. Phys.* **40**, 4948 (2001).

62. T. Kimura *et al.*, Magnetic control of ferroelectric polarization. *Nature* **426**, 55-58 (2003).

63. C.-W. Nan, M. I. Bichurin, S. Dong, D. Viehland, G. Srinivasan, Multiferroic magnetoelectric composites: Historical perspective, status, and future directions. *J. Appl. Phys.* **103**, 031101 (2008).

64. S. Mathews, R. Ramesh, T. Venkatesan, J. Benedetto, Ferroelectric field effect transistor based on epitaxial perovskite heterostructures. *Science* **276**, 238-240 (1997).

65. J. Wang *et al.*, Epitaxial $BiFeO_3$ multiferroic thin film heterostructures. *Science* **299**, 1719-1722 (2003).

66. S. H. Wemple, Some transport properties of oxygen-deficient single-crystal potassium tantalate ($KTaO_3$). *Phys. Review* **137**, A1575-A1582 (1965).

67. A. Ohtomo, H. Y. Hwang, Surface depletion in doped $SrTiO_3$ thin films. *Appl. Phys. Lett.* **84**, 1716 (2004).

68. R. D. Shannon, Revised effective ionic-radii and systematic studies of interatomic distances in halides and chalcogenides. *Acta Crystallogr. Sect. A* **32**, 751-767 (1976).

69. E. H. Mountstevens, J. P. Attfield, S. A. T. Redfern, Cation-size control of structural phase transitions in tin perovskites. *J. Phys.: Condens. Matter* **15**, 8315-8326 (2003).

70. W. Zhang, J. Tang, J. Ye, Structural, photocatalytic, and photophysical properties of perovskite $MSnO_3$ (M = Ca, Sr, and Ba) photocatalysts. *J. Mater. Res.* **22**, 1859-1871 (2007).

71. H. Mizoguchi, H. W. Eng, P. M. Woodward, Probing the electronic structures of ternary perovskite and pyrochlore oxides containing Sn^{4+} or Sb^{5+}. *Inorg. Chem.* **43**, 1667-1680 (2004).

72. D. J. Singh, D. A. Papaconstantopoulos, J. P. Julien, F. Cyrot-Lackmann,

Electronic structure of $Ba(Sn,Sb)O_3$: Absence of superconductivity. *Phys. Rev. B* **44**, 9519-9523 (1991).

73. H. F. Wang *et al.*, Transparent and conductive oxide films with the perovskite structure: La- and Sb-doped BaSnO3. *J. Appl. Phys.* **101**, 106105 (2007).

74. B. Hadjarab, A. Bouguelia, M. Trari, Optical and transport properties of lanthanum-doped stannate $BaSnO_3$. *J. Phys. D: Appl. Phys.* **40**, 5833-5839 (2007).

75. Q. Liu *et al.*, Composition dependent metal-semiconductor transition in transparent and conductive La-doped $BaSnO_3$ epitaxial films. *Appl. Phys. Lett.* **101**, 241901 (2012).

76. W.-J. Lee *et al.*, Oxygen diffusion process in a $Ba_{0.96}La_{0.04}SnO_3$ thin film on $SrTiO_3$(001) substrate as investigated by time-dependent Hall effect measurements. *Phys. Status Solidi A* **212**, 1487-1493 (2015).

77. R. Schmid, A thermodynamic analysis of the Cu-O system with an associated solution model. *Metall. Trans. B* **14**, 473-481 (1983).

78. Z. Hiroi, M. Takano, M. Azuma, Y. Takeda, A new family of copper oxide superconductors $Sr_{n+1}Cu_nO_{2n+1+\delta}$ stabilized at high pressure. *Nature* **364**, 315-317 (1993).

79. B. A. Scott, J. R. Kirtley, D. Walker, B.-H. Chen, Y. Wang, Application of scanning SQUID petrology to high-pressure materials science. *Nature* **389**, 164-167 (1997).

80. W.-J. Lee, H. J. Kim, T. H. Kim, K. H. Kim, Transparent Perovskite Barium Stannate with High Electron Mobility and Thermal Stability. *Ann. Rev. Mater. Res.* **47**, 391-423 (2017).

81. H. Mun *et al.*, Large effects of dislocations on high mobility of epitaxial perovskite $Ba_{0.96}La_{0.04}SnO_3$ films. *Appl. Phys. Lett.* **102**, 252105 (2013).

82. H. J. Kim *et al.*, Indications of strong neutral impurity scattering in $Ba(Sn,Sb)O_3$ single crystals. *Phys. Rev. B* **88**, 125204 (2013).

83. X. Luo *et al.*, High carrier mobility in transparent $Ba_{1-x}La_xSnO_3$ crystals with a wide band gap. *Appl. Phys. Lett.* **100**, 172112 (2012).

84. D. Tenne *et al.*, Raman study of oxygen reduced and re-oxidized strontium titanate. *Phys. Rev. B* **76**, 024303 (2007).

85. M. Licheron, G. Jouan, E. Husson, Characterization of $BaSnO_3$ powder obtained by a modified sol-gel route. *J. Eur. Ceram. Soc.* **17**, 1453-1457 (1997).

86. E. Moreira *et al.*, Structural and optoelectronic properties, and infrared spectrum of cubic $BaSnO_3$ from first principles calculations. *J. Appl. Phys.* **112**, 043703 (2012).

87. S. S. Li, *Semiconductor physical electronics*. (Springer Science & Business Media, 2012).

88. N. W. Ashcroft, N. D. Mermin, Solid State Physics (Holt, Rinehart and Winston, New York, 1976). *Google Scholar* **403**, (2005).

89. H. Brooks, Theory of the electrical properties of germanium and silicon. *Advances in electronics and electron physics* **7**, 85-182 (1955).

90. R. B. Dingle, XCIV. Scattering of electrons and holes by charged donors and

acceptors in semiconductors. *The London, Edinburgh, and Dublin Philosophical Magazine and Journal of Science* **46**, 831-840 (1955).

91. M. Lundstrom, *Fundamentals of carrier transport*. (Cambridge University Press, 2009).

92. W.-J. Lee *et al.*, Enhanced electron mobility in epitaxial (Ba,La)SnO_3 films on $BaSnO_3$(001) substrates. *Appl. Phys. Lett.* **108**, 082105 (2016).

93. H. Kim, J. Horwitz, S. Qadri, D. Chrisey, Epitaxial growth of Al-doped ZnO thin films grown by pulsed laser deposition. *Thin Solid Films* **420**, 107-111 (2002).

94. H. Toyosaki, M. Kawasaki, Y. Tokura, Electrical properties of Ta-doped SnO 2 thin films epitaxially grown on TiO 2 substrate. *Appl. Phys. Lett.* **93**, 132109 (2008).

95. T. Ohnishi, K. Shibuya, T. Yamamoto, M. Lippmaa, Defects and transport in complex oxide thin films. *J. Appl. Phys.* **103**, 103703 (2008).

96. T. Koida, M. Kondo, Comparative studies of transparent conductive Ti-, Zr-, and Sn-doped In[sub 2]O[sub 3] using a combinatorial approach. *J. Appl. Phys.* **101**, 063713 (2007).

97. D. J. Keeble *et al.*, Suppression of vacancy defects in epitaxial La-doped SrTiO3 films. *Appl. Phys. Lett.* **99**, 232905 (2011).

98. E. Ertekin *et al.*, Interplay between intrinsic defects, doping, and free carrier concentration in SrTiO3thin films. *Phys. Rev. B* **85**, (2012).

99. R. Ubic, Revised method for the prediction of lattice constants in cubic and pseudocubic perovskites. *J. Am. Ceram. Soc.* **90**, 3326-3330 (2007).

100. H. J. Scheel, J. G. Bednorz, P. Dill, Crystal growth of strontium titanate $SrTiO_3$. *Ferroelectrics* **13**, 507-509 (1976).

101. S. A. Chambers, T. C. Kaspar, A. Prakash, G. Haugstad, B. Jalan, Band alignment at epitaxial $BaSnO_3/SrTiO_3$(001) and $BaSnO_3/LaAlO_3$(001) heterojunctions. *Appl. Phys. Lett.* **108**, 152104 (2016).

102. J. M. Henriques, E. W. S. Caetano, V. N. Freire, J. A. P. d. Costa, E. L. Albuquerque, Structural, electronic, and optical absorption properties of orthorhombic $CaSnO_3$ through ab initio calculations. *J. Phys. Condens. Matter* **19**, 106214 (2007).

103. R. Uecker *et al.*, Properties of rare-earth scandate single crystals (Re=Nd−Dy). *J. Cryst. Growth* **310**, 2649-2658 (2008).

104. C. Derks *et al.*, Band-gap variation in $RScO_3$(R=Pr, Nd, Sm, Eu, Gd, Tb, and Dy): X-ray absorption and O *K*-edge x-ray emission spectroscopies. *Phys. Rev. B* **86**, (2012).

105. G. E. Jellison, I. Paulauskas, L. A. Boatner, D. J. Singh, Optical functions of $KTaO_3$ as determined by spectroscopic ellipsometry and comparison with band structure calculations. *Phys. Rev. B* **74**, (2006).

106. R. Uecker *et al.*, Spiral formation during Czochralski growth of rare-earth scandates. *J. Cryst. Growth* **295**, 84-91 (2006).

107. T. M. Gesing, R. Uecker, J. C. Buhl, Refinement of the crystal structure of praseodymium orthoscandate, $PrScO_3$. *Zeitschrift für Kristallographie - New Crystal Structures* **224**, (2009).

108. G. L. Lucena, A. S. Maia, A. G. Souza, I. M. G. Santos, Structural changes in Fe-doped $SrSnO_3$ perovskites during thermal analysis. *J. Therm. Anal. Calorim.* **115**, 137-144 (2013).

109. K. Ovanesyan, A. Petrosyan, G. Shirinyan, C. Pedrini, L. Zhang, Single crystal growth and characterization of $LaLuO_3$. *Opt. Mater.* **10**, 291-295 (1998).

110. J. Liu, F. Iguchi, N. Sata, H. Yugami, Optical absorption of Sr-doped $LaScO_3$ single crystals. *Solid State Ionics* **178**, 521-526 (2007).

111. B. J. Kennedy, C. J. Howard, B. C. Chakoumakos, High-temperature phase transitions in $SrHfO_3$. *Phys. Rev. B* **60**, 2972-2975 (1999).

112. C. Rossel *et al.*, Field-effect transistors with $SrHfO_3$ as gate oxide. *Appl. Phys. Lett.* **89**, 053506 (2006).

113. K. H. K. D. H. Jang, Single crystal growth and optical properties of a transparent perovskite oxide PrInO3. (unpublished results).

114. D. Souptel, G. Behr, A. Balbashov, $SrZrO_3$ single crystal growth by floating zone technique with radiation heating. *J. Cryst. Growth* **236**, 583-588 (2002).

115. R. Schafranek *et al.*, Band offsets at the epitaxial $SrTiO_3/SrZrO_3$(0 0 1) heterojunction. *J. Phys. D: Appl. Phys.* **45**, 055303 (2012).

116. D. H. Jang *et al.*, Single crystal growth and optical properties of a transparent perovskite oxide LaInO3. *J. Appl. Phys.* **121**, 125109 (2017).

117. T. Maekawa, K. Kurosaki, S. Yamanaka, Thermal and mechanical properties of perovskite-type barium hafnate. *J. Alloys Compd.* **407**, 44-48 (2006).

118. G. Lupina *et al.*, Characterization of group II hafnates and zirconates for metal-insulator-metal capacitors. *Phys. Status Solidi B* **248**, 323-326 (2011).

119. K. L. Ovanesyan, A. G. Petrosyan, G. O. Shirinyan, C. Pedrini, L. Zhang, Czochralski single crystal growth of Ce- and Pr-doped $LaLuO_3$, double oxide. *J. Cryst. Growth* **198**, 497-500 (1999).

120. K. Xiong, J. Robertson, Electronic structure of oxygen vacancies in La_2O_3, Lu_2O_3 and $LaLuO_3$. *Microelectron. Eng.* **86**, 1672-1675 (2009).

121. J. L. Zhang, J. E. Evetts, $BaZrO_3$ and $BaHfO_3$ - preparation, properties and compatibility with $YBa_2Cu_3O_{7-X}$. *J. Mater. Sci.* **29**, 778-785 (1994).

122. J. Robertson, Band offsets of wide-band-gap oxides and implications for future electronic devices. *J. Vac. Sci. Technol. B* **18**, 1785 (2000).

123. P. V. Wadekar *et al.*, Improved electrical mobility in highly epitaxial La:$BaSnO_3$ films on $SmScO_3$(110) substrates. *Appl. Phys. Lett.* **105**, 052104 (2014).

124. C. Park *et al.*, High mobility field effect transistor based on $BaSnO_3$ with Al_2O_3 gate oxide. *Appl. Phys. Lett.* **105**, 203503 (2014).

125. J. Shiogai, K. Nishihara, K. Sato, A. Tsukazaki, Improvement of electron mobility in La:$BaSnO_3$ thin films by insertion of an atomically flat insulating (Sr,Ba)SnO_3 buffer layer. *AIP Adv.* **6**, 065305 (2016).

126. C. A. Niedermeier *et al.*, Solid phase epitaxial growth of high mobility La:$BaSnO_3$ thin films co-doped with interstitial hydrogen. *Appl. Phys. Lett.* **108**, 172101 (2016).

127. U. S. Alaan, P. Shafer, A. T. N'Diaye, E. Arenholz, Y. Suzuki, Gd-doped $BaSnO_3$: A transparent conducting oxide with localized magnetic moments. *Appl. Phys. Lett.* **108**, 042106 (2016).

128. Q. Liu *et al.*, Effect of thickness on the electrical and optical properties of epitaxial $(La_{0.07}Ba_{0.93})SnO_3$ thin films. *Superlattices Microstruct.* **96**, 205-211 (2016).

129. K. Ganguly *et al.*, Structure and transport in high pressure oxygen sputter-deposited $BaSnO_{3-\delta}$. *APL Mater.* **3**, 062509 (2015).

130. R. H. Wei *et al.*, Solution processing of transparent conducting epitaxial La:$BaSnO_3$ films with improved electrical mobility. *Appl. Phys. Lett.* **106**, 101906 (2015).

131. Z. Lebens-Higgins *et al.*, Direct observation of electrostatically driven band gap renormalization in a degenerate perovskite transparent conducting oxide. *Phys. Rev. Lett.* **116**, 027602 (2016).

132. R. Uecker *et al.*, Large-lattice-parameter perovskite single-crystal substrates. *J. Cryst. Growth*, (2016).

133. K. Krishnaswamy *et al.*, $BaSnO_3$ as a channel material in perovskite oxide heterostructures. *Appl. Phys. Lett.* **108**, 083501 (2016).

134. U. Kim, C. Park, Y. M. Kim, J. Shin, K. Char, Conducting interface states at LaInO3/BaSnO3 polar interface controlled by Fermi level. *APL Mater.* **4**, 071102 (2016).

135. K. Nomura *et al.*, Thin-film transistor fabricated in single-crystalline transparent oxide semiconductor. *Science* **300**, 1269-1272 (2003).

136. T. I. Suzuki *et al.*, Hall and field-effect mobilities of rlectrons sccumulated at a lattice-matched ZnO/$ScAlMgO_4$ heterointerface. *Adv. Mater.* **16**, 1887-1890 (2004).

137. T. Miyasako, M. Senoo, E. Tokumitsu, Ferroelectric-gate thin-film transistors using indium-tin-oxide channel with large charge controllability. *Appl. Phys. Lett.* **86**, 162902 (2005).

138. M. Prins, S. Zinnemers, J. Cillessen, J. Giesbers, Depletion-type thin-film transistors with a ferroelectric insulator. *Appl. Phys. Lett.* **70**, 458-460 (1997).

139. J. Nishii, A. Ohtomo, K. Ohtani, H. Ohno, M. Kawasaki, High-mobility field-effect transistors based on single-crystalline ZnO channels. *Jpn. J. Appl. Phys.* **44**, L1193 (2005).

140. K. Uchida *et al.*, A single crystalline strontium titanate thin film transistor. *J. Appl. Phys.* **107**, 096103 (2010).

141. K. Shibuya, T. Ohnishi, M. Lippmaa, M. Kawasaki, H. Koinuma, Single crystal $SrTiO_3$ field-effect transistor with an atomically flat amorphous $CaHfO_3$ gate insulator. *Appl. Phys. Lett.* **85**, 425 (2004).

142. K. Nishio, T. Abe, R. Takahashi, M. Lippmaa, Characteristics of SrTiO3 Field-Effect Transistors with DyScO3 Gate Insulators. *Jpn. J. Appl. Phys.* **49**, 125701 (2010).

143. U. Kim *et al.*, All-perovskite transparent high mobility field effect using epitaxial $BaSnO_3$ and $LaInO_3$. *APL Mater.* **3**, 036101 (2015).

144. S. M. Sze, *Semiconductor devices: physics and technology*. (John Wiley & Sons,

2008).

145. Z. Q. Liu *et al.*, Origin of the two-dimensional electron gas at $LaAlO_3/SrTiO_3$ Interfaces: The role of oxygen vacancies and electronic reconstruction. *Phys. Rev. X* **3**, 021010 (2013).

146. L. Yu, A. Zunger, A polarity-induced defect mechanism for conductivity and magnetism at polar-nonpolar oxide interfaces. *Nature Comm.* **5**, 5118 (2014).

147. T. Tsuruoka *et al.*, Effects of moisture on the switching characteristics of oxide-based, gapless-type atomic switches. *Adv. Funct. Mater.* **22**, 70-77 (2012).

148. J.-C. Wang *et al.*, High-performance multilevel resistive switching gadolinium oxide memristors with hydrogen plasma immersion ion implantation treatment. *IEEE Electron Device Lett.* **35**, 452-454 (2014).

149. J. Lane, J. Kilner, Measuring oxygen diffusion and oxygen surface exchange by conductivity relaxation. *Solid State Ionics* **136**, 997-1001 (2000).

150. Y. Li *et al.*, Secondary-ion-mass-spectroscopy study of oxygen tracer diffusion in ac-axis-orientedYBa2Cu3O7−δfilm. *Phys. Rev. B* **51**, 8498-8502 (1995).

151. J. R. LaGraff, D. A. Payne, Chemical diffusion of oxygen in single-crystal and polycrystallineYBa2Cu3O6+xdetermined by electrical-resistance measurements. *Phys. Rev. B* **47**, 3380-3390 (1993).

152. K. Conder, E. Kaldis, M. Maciejewski, K. Müller, E. Steigmeier, Oxygen isotope exchange kinetics and site-selective oxygen substitution in YBa2Cu318O7− χ. *Physica C* **210**, 282-288 (1993).

153. S. H. Lee, S. C. Bae, J. K. Ku, H. J. Shin, Oxygen diffusion in epitaxialYBa2Cu3O7−xthin films. *Phys. Rev. B* **46**, 9142-9146 (1992).

154. S. J. Rothman, J. L. Routbort, U. Welp, J. E. Baker, Anisotropy of oxygen tracer diffusion in single-crystalYBa2Cu3O7−δ. *Phys. Rev. B* **44**, 2326-2333 (1991).

155. K. Kishio *et al.*, Study on chemical diffusion of oxygen in Ba2YCu3O7− δ. *J. Solid State Chem.* **82**, 192-202 (1989).

156. K. Szot, W. Speier, R. Carius, U. Zastrow, W. Beyer, Localized metallic conductivity and self-healing during thermal reduction of SrTiO3. *Phys Rev Lett* **88**, 075508 (2002).

157. D. A. Muller, N. Nakagawa, A. Ohtomo, J. L. Grazul, H. Y. Hwang, Atomic-scale imaging of nanoengineered oxygen vacancy profiles in SrTiO3. *Nature* **430**, 657-661 (2004).

158. S. Lee *et al.*, The effect of oxygen remote plasma treatment on ZnO TFTs fabricated by atomic layer deposition. *Phys. Status Solidi A* **207**, 1845-1849 (2010).

159. S. Kittelberger, O. Stoll, R. Huebener, Oxygen diffusion in thin films studied from isothermal electric resistivity measurements. *Supercond. Sci. Technol.* **11**, 744 (1998).

160. K. Yamamoto, B. M. Lairson, J. C. Bravman, T. H. Geballe, Oxidation kinetics of YBa2Cu3O7−x thin films in the presence of atomic oxygen and molecular oxygen by in-situ resistivity measurements. *J. Appl. Phys.* **69**, 7189 (1991).

161. L. Malavasi, G. Flor, Oxygen chemical diffusion coefficient in manganite thin films by isothermal electric resistivity measurements. *The Journal of Physical Chemistry B* **107**, 13880-13884 (2003).

162. J. Nowotny, M. Rekas, Defect structure, electrical properties and transport in barium titanate. VII. Chemical diffusion in Nb-doped BaTiO3. *Ceram. Int.* **20**, 265-275 (1994).

163. R. Moos, K. H. Hardtl, Defect Chemistry of Donor-Doped and Undoped Strontium Titanate Ceramics between 1000° and 1400° C. *J. Am. Ceram. Soc.* **80**, 2549-2562 (1997).

164. R. Meyer, R. Waser, J. Helmbold, G. Borchardt, Observation of vacancy defect migration in the cation sublattice of complex oxides by 18O tracer experiments. *Phys Rev Lett* **90**, 105901 (2003).

165. R. Merkle, J. Maier, How Is Oxygen Incorporated into Oxides? A Comprehensive Kinetic Study of a Simple Solid-State Reaction with SrTiO3 as a Model Material. *Angew. Chem. Int. Ed.* **47**, 3874-3894 (2008).

166. C.-J. Shin, H.-I. Yoo, Al-doped SrTiO 3: Part II, unusual thermodynamic factor and chemical diffusivity. *Solid State Ionics* **178**, 1089-1094 (2007).

167. P. Pasierb, S. Komornicki, M. Rekas, Comparison of the chemical diffusion of undoped and Nb-doped SrTiO 3. *J. Phys. Chem. Solids* **60**, 1835-1844 (1999).

168. A. Müller, K. Härdtl, Ambipolar diffusion phenomena in BaTiO 3 and SrTiO 3. *Applied Physics A: Materials Science & Processing* **49**, 75-82 (1989).

169. P. Singh *et al.*, Electronic structure, electrical and dielectric properties of $BaSnO_3$ below 300 K. *Jpn. J. Appl. Phys.* **47**, 3540-3545 (2008).

170. C. Shan *et al.*, Optical and electrical properties of sol–gel derived $Ba_{1-x}La_xSnO_3$ transparent conducting films for potential optoelectronic applications. *J. Phys. Chem. C* **118**, 6994-7001 (2014).

171. D. Seo *et al.*, Infrared-optical spectroscopy of transparent conducting perovskite (La,Ba)SnO_3 thin films. *Appl. Phys. Lett.* **104**, 022102 (2014).

172. U. Kim *et al.*, Dopant-site-dependent scattering by dislocations in epitaxial films of perovskite semiconductor $BaSnO_3$. *APL Mater.* **2**, 056107 (2014).

173. D. O. Scanlon, Defect engineering of $BaSnO_3$ for high-performance transparent conducting oxide applications. *Phys. Rev. B* **87**, 161201(R) (2013).

174. H.-R. Liu, J.-H. Yang, H. J. Xiang, X. G. Gong, S.-H. Wei, Origin of the superior conductivity of perovskite Ba(Sr)SnO_3. *Appl. Phys. Lett.* **102**, 112109 (2013).

175. C. Ling, C. L. Chen, A. J. Jacobson, Electrical conductivity relaxation studies of oxygen transport in epitaxial YBa/sub 2/Cu/sub 3/O//sub 7-γ/ thin films. *IEEE Transactions on Appiled Superconductivity* **13**, 2882-2885 (2003).

176. V. Metlenko *et al.*, Do dislocations act as atomic autobahns for oxygen in the perovskite oxide SrTiO3? *Nanoscale* **6**, 12864-12876 (2014).

177. G. Blaustein, M. Castro, C. Aldao, Influence of frozen distributions of oxygen vacancies on tin oxide conductance. *Sens. Actuators, B* **55**, 33-37 (1999).

178. F. Hernandez-Ramirez *et al.*, Insight into the role of oxygen diffusion in the sensing mechanisms of SnO2 nanowires. *Adv. Funct. Mater* **18**, 2990-2994 (2008).

179. F. Hernandez-Ramirez *et al.*, Insight into the Role of Oxygen Diffusion in the Sensing Mechanisms of SnO2Nanowires. *Adv. Funct. Mater.* **18**, 2990-2994 (2008).

180. P. Shewmon, *Diffusion in solids*. (Springer, 2016).

181. J. Crank, *The mathematics of diffusion*. (Oxford university press, 1979).

182. P. Pasierb, S. Komornicki, M. Rekas, Comparison of the chemical diffusion of undoped and Nb-doped $SrTiO_3$. *J. Phys. Chem. Solids* **60**, 1835-1844 (1999).

183. R. A. De Souza, V. Metlenko, D. Park, T. E. Weirich, Behavior of oxygen vacancies in single-crystal $SrTiO_3$: Equilibrium distribution and diffusion kinetics. *Phys. Rev. B* **85**, (2012).

184. H.-I. Yoo, C.-R. Song, D.-K. Lee, BaTiO 3− δ: defect structure, electrical conductivity, chemical diffusivity, thermoelectric power, and oxygen nonstoichiometry. *J. Electroceram.* **8**, 5-36 (2002).

185. M. Kessel, R. A. De Souza, M. Martin, Oxygen diffusion in single crystal barium titanate. *Phys. Chem. Chem. Phys.* **17**, 12587-12597 (2015).

186. L. Bjaalie, B. Himmetoglu, L. Weston, A. Janotti, G. C. Van de Walle, Oxide interfaces for novel electronic applications. *New J. Phys.* **16**, 025005 (2014).

187. X. Fan, W. Zheng, X. Chen, D. J. Singh, 2DEGs at perovskite interfaces between $KTaO_3$ or $KNbO_3$ and stannates. *PLoS One* **9**, e91423 (2014).

188. M. Kawasaki *et al.*, Atomic Control of the SrTiO3 Crystal Surface. *Science* **266**, 1540-1542 (1994).

189. G. Koster, B. L. Kropman, G. J. H. M. Rijnders, D. H. A. Blank, H. Rogalla, Quasi-ideal strontium titanate crystal surfaces through formation of strontium hydroxide. *Appl. Phys. Lett.* **73**, 2920-2922 (1998).

190. C. H. Y. Abhijit Biswas, Ramamoorthy Ramesh, and Yoon H. Jeong, Atomically flat single terminated oxide substrate surfaces. *Unpublished manuscript*.

191. F. Sanchez, C. Ocal, J. Fontcuberta, Tailored surfaces of perovskite oxide substrates for conducted growth of thin films. *Chem. Soc. Rev.* **43**, 2272-2285 (2014).

192. R. Bachelet, F. Valle, I. C. Infante, F. Sánchez, J. Fontcuberta, Step formation, faceting, and bunching in atomically flat SrTiO[sub 3] (110) surfaces. *Appl. Phys. Lett.* **91**, 251904 (2007).

193. K. Sudoh, H. Iwasaki, Kinetics of faceting driven by attractive step-step interactions on vicinal Si(113). *Phys Rev Lett* **87**, 216103 (2001).

194. G.-B. Cho, M. Yamamoto, Y. Endo, Surface features of self-organized SrTiO3 (001) substrates inclined in [100] and [110] directions. *Thin Solid Films* **464-465**, 80-84 (2004).

195. L. Zhang, D. Wett, R. Szargan, T. Chassé, Determination of ZnO(0001) surface termination by x-ray photoelectron spectroscopy at photoemission angles of 0° and 70°. *Surf. Interface Anal.* **36**, 1479-1483 (2004).

196. M. Sing *et al.*, Profiling the interface electron gas of LaAlO3/SrTiO3 heterostructures with hard x-ray photoelectron spectroscopy. *Phys. Rev. Lett.* **102**, 176805 (2009).

197. H. Van Doveren, J. Verhoeven, XPS spectra of Ca, Sr, Ba and their oxides. *J. Electron. Spectrosc. Relat. Phenom.* **21**, 265-273 (1980).

198. M. Koenig, J. Grant, XPS studies of the chemical state of Ba on the surface of

impregnated tungsten dispenser cathodes. *Applications of Surface Science* **20**, 481-496 (1985).

199. P. Van der Heide, Surface core level shifts in photo-electron spectra from the Ca, Sr and Ba titanates. *Surf. Sci.* **490**, L619-L626 (2001).

200. L. T. Hudson, R. L. Kurtz, S. W. Robey, D. Temple, R. L. Stockbauer, Surface core-level shifts of barium observed in photoemission of vacuum-fracturedBaTiO3(100). *Phys. Rev. B* **47**, 10832-10838 (1993).

201. C. Baeumer *et al.*, Surface Termination Conversion during SrTiO3 Thin Film Growth Revealed by X-ray Photoelectron Spectroscopy. *Sci. Rep.* **5**, 11829 (2015).

202. A. Ohtomo, H. Hwang, A high-mobility electron gas at the $LaAlO_3/SrTiO_3$ heterointerface. *Nature* **427**, 423-426 (2004).

203. N. C. Bristowe, P. Ghosez, P. B. Littlewood, E. Artacho, The origin of two-dimensional electron gases at oxide interfaces: insights from theory. *J. Phys.: Condens. Matter* **26**, 143201 (2014).

204. G. Herranz *et al.*, High mobility in $LaAlO_3/SrTiO_3$ heterostructures: origin, dimensionality, and perspectives. *Phys Rev Lett* **98**, 216803 (2007).

205. A. P. Kajdos, D. G. Ouellette, T. A. Cain, S. Stemmer, Two-dimensional electron gas in a modulation-doped $SrTiO_3/Sr(Ti, Zr)O_3$ heterostructure. *Appl. Phys. Lett.* **103**, 082120 (2013).

206. Y. Z. Chen *et al.*, Extreme mobility enhancement of two-dimensional electron gases at oxide interfaces by charge-transfer-induced modulation doping. *Nature Mater.* **14**, 801-806 (2015).

207. Y. Kozuka *et al.*, Two-dimensional normal-state quantum oscillations in a superconducting heterostructure. *Nature* **462**, 487-490 (2009).

208. B. Jalan, S. Stemmer, S. Mack, S. J. Allen, Two-dimensional electron gas in δ-doped $SrTiO_3$. *Phys. Rev. B* **82**, (2010).

209. V. Stevanović, S. Lany, D. S. Ginley, W. Tumas, A. Zunger, Assessing capability of semiconductors to split water using ionization potentials and electron affinities only. *Phys. Chem. Chem. Phys.* **16**, 3706-3714 (2014).

210. P. Dorenbos, The electronic structure of lanthanide impurities in TiO_2, ZnO, SnO_2, and related compounds. *ECS Journal of Solid State Science and Technology* **3**, R19-R24 (2014).

211. S. A. Chambers, Y. Liang, Z. Yu, R. Droopad, J. Ramdani, Band offset and structure of $SrTiO_3$/Si(001) heterojunctions. *J. Vac. Sci. Technol. A* **19**, 934 (2001).

212. N. Nakagawa, H. Y. Hwang, D. A. Muller, Why some interfaces cannot be sharp. *Nat. Mater.* **5**, 204-209 (2006).

213. A. K. Singh, A. Janotti, M. Scheffler, C. G. Van de Walle, Sources of electrical conductivity in SnO2. *Phys Rev Lett* **101**, 055502 (2008).

214. M. L. Reinle-Schmitt *et al.*, Tunable conductivity threshold at polar oxide interfaces. *Nat Commun* **3**, 932 (2012).

215. A. D. Caviglia *et al.*, Two-dimensional quantum oscillations of the conductance at $LaAlO_3/SrTiO_3$ interfaces. *Phys. Rev. Lett.* **105**, 236802 (2010).

216. K. Ueno *et al.*, Electric-field-induced superconductivity in an insulator. *Nature*

Mater. **7**, 855-858 (2008).

217. K. Ueno *et al.*, Discovery of superconductivity in $KTaO_3$ by electrostatic carrier doping. *Nat. Nanotechnol.* **6**, 408-412 (2011).

218. N. Reyren *et al.*, Superconducting interfaces between insulating oxides. *Science* **317**, 1196-1199 (2007).

Appendix A New design of a microcalorimeter for measuring absolute heat capacity from 300 to 550 K

A.1 Introduction

Heat capacity (C_p) measurements are one of the most fundamental probes for studying the basic properties of solids such as magnetic [1,2], structural and electronic phase transitions [3-5]. Since many interesting new materials including oxide single crystals, polymers and bio materials often exist in a small volume, the C_p measurements of those small samples become quite challenging due to the relatively large addenda heat capacity, C_{add}, of a calorimeter platform. The C_{add} value of a commercially available calorimeter is typically as high as 1-10 mJ K^{-1} at room temperature. Therefore, if the sample C_p is not large enough to compared to C_{add}, accurate C_p measurements becomes quite difficult. In order to overcome those limitations, it is important first of all to reduce C_{add}.

Over the past three decades, numerous efforts have been made to fabricate novel micro or nanocalorimeters with greatly reduced C_{add} [6-13]. In particular, it has well known that a calorimeter made of amorphous Si:N (*a*-Si:N) membrane is useful for achieving the extremely small C_{add} down to a few nJ K^{-1} [9-12]. With these developments, the microcalorimeter is being progressively used to measure various small samples with greatly enhanced sensitivity. A few examples include the samples with a nanometer length scale, i.e., thin nanofilms [11,12,14-17], nanoparticles [18], nanopolymers [13,19-21], micro organic materials [22], carbon nanotubes [23,24] and micro bio materials [25]. However,

most heater designs of these micro or nanocalorimeters consist of serpentine lines, which often produces temperature gradient within the sample platform [9,11,17,24,26,27]. Therefore, in order to achieve the isothermal condition on the sample platform, a thick thermal conduction layer or a thin membrane layer has been tried, which consequently gives rise to a large C_{add} or a fragile membrane, respectively. Recently, the conventional design of a heater and a thermal sensor was modified to the circular shape design [28,29].

We have previously developed several types of microcalorimeters based on the *a*-Si:N membrane, i.e., Type I-III, which consist of basically meander-shaped heater/sensor leads on the sample platform [30,31]. Type I and II microcalorimeters, however, produced rather large errors in the C_p data as high as 15-20 % from 20 to 300 K. Those errors were mainly coming from an imperfect isothermal condition in the sample platform. Moreover, a Type III microcalorimeter with well separated and relatively thin heater/sensor leads has exhibited reduced measurement errors down to 10 % from 20 to 300 K. In spite of these results, C_{add} values were rather large at room temperature (~20 μJ K^{-1}), and the measurement error systematically increased at higher temperatures to reach as high as 10-15 % [32]. In order to enhance the accuracy of the measured C_p data and to reduce the temperature gradient within the sample platform, it has become necessary to modify geometry of a heater and a thermal sensor.

In this work, we report a new Type IV microcalorimeter with further reduced errors above 300 K. Based on the computer simulation of the two dimensional (2D) thermal profile and actual microfabrications, we found that the sample platform composed of an isothermal Au film of a disc shape and concentric Pt leads (a heater and a thermal sensor) has better heat confinement, and thus produce a good isothermal condition. Moreover, we designed the microcalorimeter to have all the isothermal platform and heater/sensor leads in one side of the membrane by use of an amorphous SiO_2 (*a*-SiO_2) insulation layer so that the

microfabrication became easy and cost-effective.

A.2 Experimentals

A.2.1 Thermal simulation

To apply thermal simulation by use of the COMSOL Multiphysics™, the two types of microcalorimeters were prepared. Figure A.1 shows a structure of Type III and of newly designed Type IV microcalorimeters used in the simulation. The cross-sectional and planar views of Type III are shown in Figs. A.1(a) and (b), respectively, which consists of the Au isothermal layer located in the center of the *a*-Si:N membrane (1000 nm thick). Meander-shaped Au heater/sensor leads (50 nm thick) are located on the left and right sides of the Au isothermal layer, respectively. The width of Au heater/sensor leads is 20 μm and the distance between each line is 40 μm. The cross-sectional and planar views of Type IV are also shown in Figs. A.1(c) and (d), respectively. In sharp contrast to the case of Type III, Type IV is composed of two amorphous membrane layers, i.e., *a*-Si:N (500 nm thick) and *a*-SiO_2 (200 nm thick). The circular Pt heater/sensor leads (50 nm thick) are located in between the two membrane layers so that they are electrically isolated with the Au isothermal layer (200 nm thick). The width of the heater/sensor leads is 10 μm and the distance between each line is 20 μm.

Table A.1 κ (W m^{-1} K^{-1}) values of components used in the thermal simulation at 20, 300 and 600 K.

	20 K	300 K	600 K
a-Si:N	0.8 [a)]	3.0 [a)]	3.5 [f)]
a-SiO_2	0.15 [b)]	1.0 [c)]	1.3 [b)]

Au	400 [d]	320 [d]	305 [e]
Pt	450 [d]	70 [d]	73 [e]

a) Ref. 32, b) Ref. 33, c) Ref. 34, d) Ref. 35, e) Ref. 36

f) This value was extrapolated by using κ vs T in Ref. 32.

Since the total membrane thickness of ~1 μm is much smaller than the planar length scale [33], we safely used the 2D finite element method to predict the planar temperature profiles. Here, we used 2D thermal conductivity as $\kappa_{2d} = \kappa \cdot t$, in which κ and t are thermal conductivity and thickness of the deposited materials (*a*-Si:N, *a*-SiO_2, Au and Pt). All the κ values used in the simulation are summarized in the Table 1 [34-38]. As C_p measurements are performed under high vacuum (~10^{-5} Torr), we considered the thermal conduction and black-body radiation effects in the simulation. In order to increase the temperature of the sample platform, we applied power, P, to the Pt heater and monitored temperature values in a steady state. Increased temperature (ΔT) was set to be about 4 % of the reservoir temperature (T_0) in the simulation (ΔT = 0.8 K at 20 K, 12 K at 300 K and 24 K at 600 K).

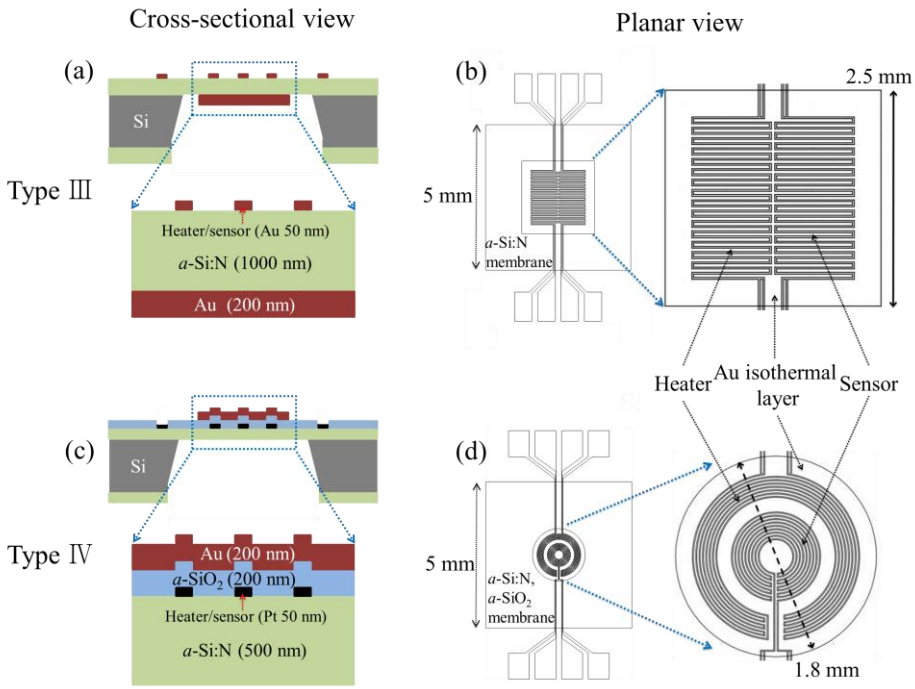

Figure A.1 Schematic drawings showing (a) cross-sectional and (b) planar layouts of our previous microcalorimeter (Type III, reproduced from Refs. 28 and 29), and (c) cross-sectional and (d) planar layouts of the new microcalorimeter fabricated in this work (Type IV). In (a) and (b), the *a*-Si:N membrane is supported by the Si frame (10 × 10 mm^2) while the Au isothermal layer is located in the backside of the *a*-Si:N membrane. In (c) and (d), the membrane area is composed of *a*-Si:N and *a*-SiO_2 layers while the Au isothermal layer of a disc shape and Pt heater/sensor leads of a concentric shape are located in the center of the membrane. The area of the Au isothermal region is reduced in Type IV microcalorimeter.

A.2.2 Fabrication

In the previous fabrication processes based on the *a*-Si:N membrane, metal films for an isothermal layer were deposited at the back side of the microcalorimeter [30,31]. This has often caused a mismatch between the areas of the metal isothermal films and heater/sensor leads because a perfect alignment of the shadow mask was somewhat difficult.

Moreover, the use of a shadow mask in the backside made the fabrication of a smaller isothermal area difficult, which in turn prevented the C_{add} from being reduced further.

In order to overcome the limitations, we introduced the *a*-SiO_2 layer on top of the *a*-Si:N membrane. There are several reasons and advantages for using the additional *a*-SiO_2 layer in the membrane. First, it was used for making electrical insulation between heater/sensor leads and the Au isothermal layer. Second, because the deposition process in the backside is not necessary anymore, the microfabrication became more simpler than the previous cases using the deposition in both sides of the membrane [30,31]. As a result, all the isothermal platform and heater/sensor leads are located in the top side of the membrane, which made the microfabrication easier and more cost-effective. Third, due to the superior mechanical strength of the *a*-SiO_2, the *a*-SiO_2 layer of 200 nm thick in combination of the *a*-Si:N layer of 500 nm was enough to constitute the strong membrane layers as compared with the previous case of using ~1000 nm thick *a*-Si:N membrane only (Type III) [31]. Detailed fabrication procedures are summarized below and are displayed in Fig. A.2.

(a) A low stress *a*-Si:N layer of 500 nm thick was deposited in both sides of a four-inch Si (100) wafer using low-pressure chemical vapor deposition (LPCVD) at 820 °C.

(b) Photolithography with a photo-mask 1 was used to form heater and sensor patterns. Cr/Pt layers of 5/50 nm thick were subsequently deposited through the sputtering. After the lift-off process, only metal patterns remained in the *a*-Si:N layer.

(c) The *a*-SiO_2 layer of 200 nm thick was deposited by the plasma-enhanced chemical vapor deposition (PECVD) at 350 °C.

(d) Photolithography with a photo-mask 2 was used to form the isothermal Au layer of a circular shape. Ti/Au layers of 5/200 nm thick were deposited sequentially through the thermal evaporation method. After the lift-off process, only the isothermal layer remained

in the *a*-SiO_2 layer.

(e) Photolithography with a photo-mask 3 was used to expose the contact pad of a heater and a thermal sensor. The *a*-SiO_2 layer on the contact pad was etched away in a buffered oxide etch solution for one minute.

(f) Photolithography with a photo-mask 4 was used to form the square shaped membrane layer (5 × 5 mm^2). Then, the square shaped *a*-Si:N layer was etched by a reactive ion etcher. The residual photoresist was removed with acetone. The backside of the Si bulk was subsequently etched away in the 20 wt.% KOH solution at 90 °C for 5 hour. The etch rate was found to be ~2 μm min^{-1}. Since the *a*-SiO_2 layer should be protected from the KOH etching, the top side of the wafer was covered by a plastic cap.

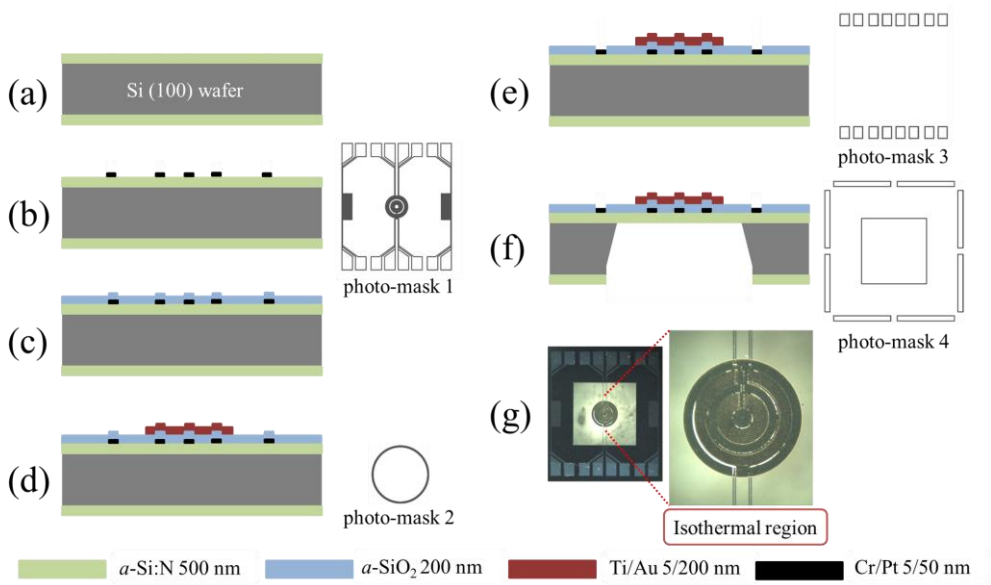

Figure A.2 Fabrication procedures for Type IV microcalorimeter; (a) deposition of the low stress *a*-Si:N using LPCVD at 820 °C, (b) photolithography with a photo-mask 1 to form Pt heater/sensor leads, (c) deposition of the *a*-SiO_2 film using PECVD at 350 °C, (d) photolithography with a photo-mask 2 to form an circular isothermal Au layer, (e) photolithography with a photo-mask 3 to open the Pt contact pad, (f) photolithography with

a photo-mask 4 and reactive ion etching of the *a*-Si:N back layer for creating the square (5 × 5 mm^2) and etch-line shapes, and the etching of bulk Si in a hot KOH solution. Finally, in (g), a planar view of the fabricated Type IV microcalorimeter and the expanded circular isothermal region are shown.

Figure A.2(g) shows the final photograph of the fabricated Type IV microcalorimeter, in which transparent *a*-Si:N and *a*-SiO_2 layers and a circular Au isothermal film with concentric Pt leads can be found. It should be stressed once more that the new microfabrication method became easier than the previous case. Therefore, the method can be applied easily in larger wafer sizes although our current method employs the four-inch wafer, which allows us to obtain a total of 49 devices.

A.2.3 C_p measurements and black-body radiation

Figure A.3 shows a schematic diagram of the instrumentation and circuit connections used in the C_p measurement. We performed the C_p measurement by using a home-made probe [32]. We controlled the base temperature (T_0) by using a tube furnace and measured T_0 by use of a S-type thermocouple. In order to compensate T_0, the outside temperature of a probe was measured by a thermistor. To provide P to a Pt heater, we applied the dc current, I_H, and measured the voltage, V_H, generated across the Pt heater by using a source meter (Keithley 236). The total P, i.e., $I_H V_H$, given to the Pt heater was automatically adjusted to induce the temperature increase (ΔT) within 3-4 % of the T_0. Typical applied P during the C_{add} measurements is about 1.5 mW (~0.24 mA) around 550 K. During the measurements of the sample heat capacity (C_{sample}), however the applied P depends on the amount of the loaded sample. For athe measurement of the 0.2 mg α-Al_2O_3 single crystal, P of 36 mW (~1.18 mA) is applied around 550 K.

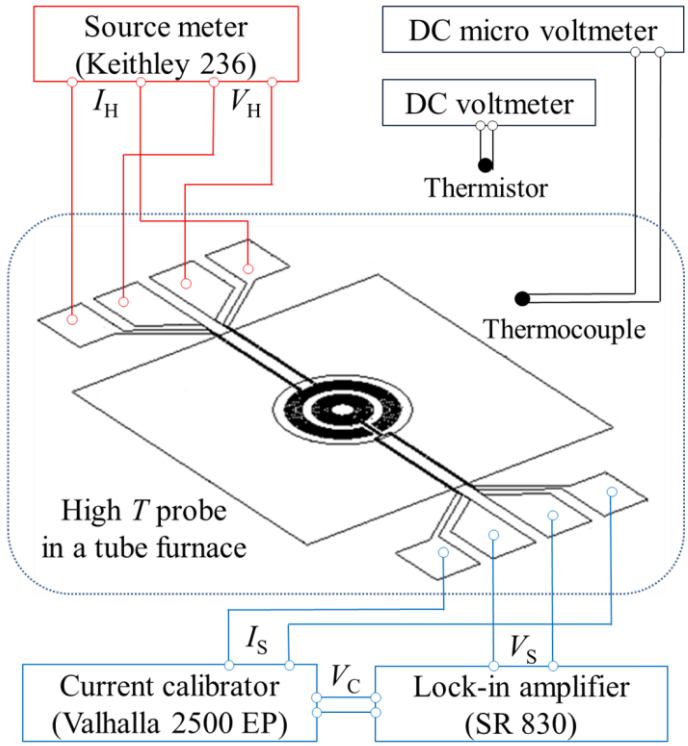

Figure A.3 A schematic diagram of the instrumentation and circuit connections for measuring heat capacity, C_p with the microcalorimeter.

The commercial lock-in amplifier (SR 830) was used to read the sensor resistance at a frequency of ~1k Hz. An ac output voltage from the lock-in amplifier, V_C, was sent to the input of a current calibrator (2500 EP, Valhalla) to generate an ac current, I_S, across the thermometer on the sample platform. V_C was set to generate I_S of ~10-50 μA. Then, the same lock-in amplifier measured V_S generated across the thermometer. All these measurements were automatically performed by a custom-made program based on LabVIEW™ [30]. It controlled all of the instruments and calculated the C_p value simultaneously based on the curve fitting method (CFM) [39].

The CFM assumes that finite thermal conductance exists between the sample and the sample platform, λ_s, in addition to the total thermal conductance between the sample

platform and the outside world, λ_l. Thus, the CFM employs two relaxation time constants, i.e., external one, τ_1, and internal one, τ_2, based on the lumped-τ_2 model [40]. This method can remedy the problems caused by the poor λ_s between the sample and the sample platform by including τ_2. If we assume that the T_0 is constant and initially in equilibrium with the platform temperature T', the general heat transfer equations in the lumped-τ_2 model can be expressed as

$$P(t) = C_{\text{add}} \frac{dT'}{dt} + \lambda_s \left(T' - T\right) + \lambda_l \left(T' - T_0\right)$$
$$0 = C_{\text{sample}} \frac{dT}{dt} + \lambda_s \left(T - T'\right) \qquad \text{Equation A.1}$$

where T is the temperature of the sample. By employing the general linear-least-square fitting scheme, we can eventually determine C_{add}, C_{sample}, λ_l, λ_s, τ_1 and τ_2.

Because the C_p measurements are performed at high temperatures, the black-body radiation can also affect the measured C_p. Upon applying ΔT onto the sample platform sitting at a T_0, the effective power loss due to the emissive radiation, ΔP_r, can be expressed as $A\sigma(\varepsilon_{\text{Au}}+\varepsilon_{a\text{-Si:N}})((T_0+\Delta T)^4-T_0^4) \approx 4A\sigma(\varepsilon_{\text{Au}}+\varepsilon_{a\text{-Si:N}})T_0^3\Delta T$ based on the Stefan–Boltzmann law. Here, A is the area of the Au isothermal region ε_{Au} and $\varepsilon_{a\text{-Si:N}}$ are emissivity of the Au film (~0.02) and the *a*-Si:N layer (~0.1) [41,42], and σ is the Stefan–Boltzmann constant. Such ΔP_r through the sample platform upon applying ΔT can effectively constitutes additional thermal conductance between the sample platform and the outside world, as in the form of $\Delta P_r/\Delta T \approx 4A\sigma(\varepsilon_{\text{Au}}+\varepsilon_{a\text{-Si:N}})T_0^3$ [7]. In the CFM, λ_l can thus include the conductance through the radiation ($\Delta P_r/\Delta T$) as well as the conductance through the membrane and metal leads (λ_{cond}) which can be expressed as $\lambda_l \approx \lambda_{\text{cond}} + 4A\sigma(\varepsilon_{\text{Au}}+\varepsilon_{a\text{-Si:N}})T_0^3$. It should be stressed once more that the black-body radiation over ΔT during the C_p measurements based on the lumped-τ_2 model is certainly included in λ_l which is not related

with the uncertainties of the measured C_p.

For the C_{add} measurement at T_0 = 550 K, ΔP_r is roughly calculated as ~0.27 mW with ΔT = 22 K, which is about 17.9 % of the typically applied P (~1.5 mW). On the other hand, $\Delta P_r/\Delta T$ at 550 K becomes approximately 12.2 μW K^{-1}, which corresponds to about 17.5 % of λ_l in the Type IV microcalorimeter (see Fig. A.5(c)). Moreover, in the case of the C_{sample} measurements, if the λ_s is sufficiently high due to the good thermal contact between the sample and the platform, $\Delta P_r/\Delta T$ could be also contained in the λ_l. However, if the thermal contact is bad, we should consider $\Delta P_r/\Delta T$, which is not included in λ_l. In the worst case, at T_0 = 550 K, ΔP_r through the α-Al_2O_3 single crystal (~0.9 × 0.9 × 0.8 mm^3) with the emissivity value of 0.02 [43] is expected as ~50.8 μW with which is only about 0.14 % of the applied P (~36 mW). Therefore, in the CFM scheme, we postulate that the uncertainty of our measured C_{sample} due to the thermal radiation can be less than 0.14 % around 550 K as the CFM is subject to the uncertainty in the determination of absolute ΔT due to the radiation through the sample platform while it can fit the λ_l increase without significant errors. We note that, in the case of the bad thermal contact between the sample and the platform, if the C_p of the sample with the large area and high emissivity was measured at high temperatures, the amount of the radiation through the sample will be significantly increased which should be corrected.

For the thermal sensor calibration, we loaded a microcalorimeter on top of the Cu block (10 × 10 × 5 mm^3), which acted as a thermal bath with relatively high κ. The Cu block with a loaded microcalorimeter was then inserted into a home-made probe. A T_0 was slowly varied by ramping up and down repeatedly with a ramping rate of 3 K min^{-1}. The measured ac resistance by the four-probe technique followed almost linear temperature dependence in repeated cycles up to 600 K in both Type III and IV. During the sensor calibration of Type III (IV), the temperature errors of the Au (Pt) thermometer were

approximately ±0.2 K (±0.1 K) as estimated by the fluctuation in the resistance data. In the case of Type III (IV), repeated thermal cycling from 300 to 600 K resulted in slight increases in the resistance offset by about 0.5–1 % (0.1 %) in each run. Such an increase was quite predictable so that the calibration was slightly adjusted after each run by adding up a small constant resistance.

In order to obtain C_p of an α-Al_2O_3 single crystal, we measured first C_{add} with a drop of silicon oil (KF-96-1000CS, Shin-etsu), which turned out to be a good thermal grease for increasing thermal contact between the sample and the platform [32]. The C_{add} measurements were performed from 300 to 550 K during a slow increase of a T_0 with a ramp rate 0.3 K min^{-1}. After measuring the C_{add}, we carefully loaded an α-Al_2O_3 single crystal (~0.2-0.4 mg), which was weighed by a micro-balance (SE2, Satorius). We then measured the C_p of an α-Al_2O_3 single crystal with the platform from 300 to 550 K. The C_{add} obtained earlier was automatically subtracted from the acquired data to calculate the C_p of an α-Al_2O_3 single crystal at each temperature.

A.3 Results and discussions

In order to compare thermal behavior of the two types of microcalorimeters, we carried out thermal simulations. Resultant isothermal contour plots of Type III at 20, 300, and 600 K are displayed in Figs. A.4(a), (b), and (c), respectively. The distance between the neighboring isothermal contour represents 5 % of each ΔT as represented in the bars at the bottom. The simulation results for Type III indicate that the temperature difference between the central regions of both the heater and the sensor is roughly about 0, 4, and 5 % at 20, 300, and 600 K, respectively. These temperature gradients persisting inside the sample platform are coupled to the errors in the absolute value of the measured specific heat, c_p (see Fig. A.6(b)). It is thus important to reduce the temperature gradient in the isothermal

platform to increase the accuracy of the measured c_p.

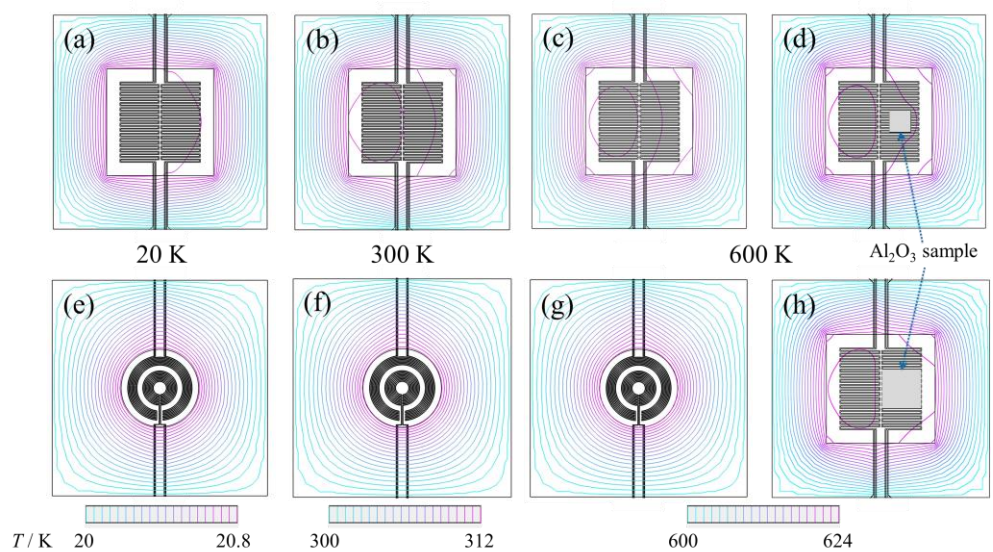

Figure A.4 Isothermal contour plots for Type III microcalorimeter at (a) 20, (b) 300 and (c) 600 K, and for Type IV microcalorimeter at (e) 20, (f) 300 and (g) 600 K. Magenta and cyan colors represent the high and low temperature contours, respectively. Each spacing of the neighboring isothermal contour represents the 5 % of ΔT. Isothermal contour plots of Type III at 600 K are also displayed with an α-Al_2O_3 sample of (d) 0.4 mg (0.5 × 0.5 × 0.4 mm^3) and (h) 2.6 mg (0.9 × 0.9 × 0.8 mm^3).

The temperature gradient is generally linked to the three physical parameters: κ_{2d} ratio defined as $\kappa_{2d,s}/\kappa_{2d,m}$, geometry of heater/senor leads, and the distance between the metal isothermal layer to the Si frame. Here, $\kappa_{2d,s}$ refers to a sum of κ_{2d} contributions of the sample platform (such as Au, Pt, *a*-Si:N and *a*-SiO_2), and $\kappa_{2d,m}$ represents a sum of κ_{2d} contributions of the membrane region (such as *a*-Si:N and *a*-SiO_2). First, we considered the κ_{2d} ratio in the Type III microcalorimeter, which was reported in Ref. [33]. If $\kappa_{2d,s}$ is high and $\kappa_{2d,m}$ is low to result in a large κ_{2d} ratio, the heat can be easily confined in the sample platform. Therefore, the value of $\kappa_{2d,s}/\kappa_{2d,m}$ stands for a gauge on the degree of the isothermal condition and heat confinement in the sample platform at each structure. Using

the value of κ and t of the used materials, we evaluated the value of $\kappa_{2d,s}/\kappa_{2d,m}$ of Type III as 106, 23.4, and 18.4 at 20, 300, and 600 K, respectively. The isothermal contour of Type III confirms that the higher value of $\kappa_{2d,s}/\kappa_{2d,m}$ clearly satisfy better the isothermal condition in the sample platform.

If one wants to increase the κ_{2d} ratio for better accuracy, it is thus possible to either increase thickness of the metal isothermal layer or reduce thickness of the amorphous membrane layers. However, increasing the thickness of the metal isothermal layer obviously results in a larger C_{add} while reducing the thickness of the membrane produces relatively weak membrane strength, which can cause easy breaking of the platform. As a result, a modification of geometry of a heater and a sensor will be additionally helpful even without directly increasing the κ_{2d} ratio. Once the lateral layout of the sample platform becomes different, the absolute value of $\kappa_{2d,s}/\kappa_{2d,m}$ that is required to reach the isothermal condition is likely to be also different.

As the second consideration to achieve a better isothermal condition, we have thus considered various geometry of the lateral layout in the sample platform and sequentially carried out the thermal simulation. Because Type III has separated heater and sensor regions to reduce the capacitive coupling during the C_p measurements, it was located in the left and right sides of the platform, resulting in a larger sample platform (see Fig. A.1(b)). Moreover, most heater designs of well-known micro or nanocalorimeters consist of serpentine lines [9,11,17,24,26,27]. Without a thick metal isothermal layer or a thin membrane layer, these structures may cause an unwanted temperature gradient in the sample platform. To remedy the shortcoming while maintaining the thickness of the metal isothermal layer, we considered concentric geometry with the isothermal platform of a disc shape in the Type IV microcalorimeter, as displayed in Figs. A.1(c) and (d).

As the third consideration of improvement, a shortest (longest) distance between the

metal isothermal layer and the Si frame was increased to be ~1.6 (2.8) mm in Type IV as compared with ~1.25 (1.8) mm in Type III, reducing heat flow from the isothermal region to the Si frame. Heat confinement is thus likely to become enhanced in Type IV. With an extended distance between the Au isothermal layer and the Si frame, the isothermal area is naturally reduced to be about ~10 % of the total membrane area in Type IV as compared with 25 % in Type III, giving rise to reduction of C_{add}. In order to reduce C_{add} further, we also reduced the thickness of the *a*-Si:N membrane from 1000 nm in Type III to 500 nm in Type IV as the *a*-SiO_2 of 200 nm thick is newly added. We note that the reported κ value of the *a*-SiO_2 is varied in literatures but obviously smaller than the *a*-Si:N from 20 to 300 K by more than two times [34-36].

Finally, since the smaller width of heater/sensor leads can be useful to increase the accuracy of the measured c_p [31], we also reduced the width of heater/sensor leads from 20 to 10 μm and the distance between each leads as 40 to 20 μm in the Type IV microcalorimeter. This thin width of heater/sensor leads consequently prevents the heat loss in the membrane regions during the C_p measurement. In Fig. A.4, the temperature gradient from heater leads on the membrane layer shows that the heat loss from the heater leads of Type III is bigger than that of Type IV.

Figures A.4(e), (f), and (g) display the resultant isothermal contour plots of Type IV at 20, 300, and 600 K, respectively. Using the value of κ and t of deposited materials, we calculated the κ_{2d} ratio in Type IV; 201, 38.3, and 30.2 at 20, 300, and 600 K, respectively. This value is 1.6-1.9 times higher than those of Type III because of reduced effective thickness in the membrane. At 20 K, a perfect isothermal platform is achieved with a higher value of the κ_{2d} ratio. Thus, if we replace the Pt sensor of Type IV to the low temperature sensor, e.g., Nb_xSi_{1-x} [7] to have better sensitivity at low temperatures, it is expected that the same Type IV microcalorimeter can be also operating successfully even well below 20

K. Moreover, at 300 K, although $\kappa_{2d,s}/\kappa_{2d,m}$ = 38.3 is rather low, the sample platform shows completely a perfect isothermal condition. Another noteworthy finding is that even though $\kappa_{2d,s}/\kappa_{2d,m}$ = 30.2 at 600 K in Type IV is only 30 % higher than that of Type III at 300 K, the sample platform is nearly isothermal. Therefore, the concentric heater and sensor seems to provide better heat confinement if the κ_{2d} ratio is fixed.

Above thermal simulations were based on the empty platform. In practice, the presence of the sample can also distort the thermal profiles as well as the resultant C_p values. In order to know such effects of the sample on the temperature profile, we performed the 2D thermal simulation with an α-Al_2O_3 sample and a value of κ [44] at 600 K in the Type III microcalorimeter, in which the effects of the sample on the temperature gradients are clearly visible. The resultant contour plots are shown in Figs. A.4(d) and (h) for the Al_2O_3 sample with 0.4 mg (0.5 × 0.5 × 0.4 mm^3) and with 2.6 mg (0.9 × 0.9 × 0.8 mm^3), respectively. Both results show that the temperature gradients are overall reduced upon increasing the sample mass and volume. However, due to the heat loss through the sample, it is found that the measured ΔT are also reduced to become 0.16 K (0.7 % of ΔT) and 0.51 K (2.1 % of ΔT), respectively. Based on these results, it is expected that the C_p measurements with Al_2O_3 samples with ~0.4–2.6 mg should not affect the resultant C_p data within 1-2 % of errors while the larger sample volume can further deteriorate the accuracy of C_p. As we have used a standard α-Al_2O_3 single crystal of 0.2–0.4 mg in the measurements in Fig. A.5, the main errors of c_p shown in Fig. A.6(b) for Type III are attributed to the lack of isothermal condition in the platform rather than the effect of sample mass/volume to the temperature profile.

Figure A.5(a) compares the total C_p of the platform with the sample and the C_{add} of Type III (solid blue dots) and IV (solid red dots) microcalorimeters. We find that the C_{add} of Type IV at 300 K (6 μJ K^{-1}) is smaller than that of Type III (20 μJ K^{-1}) by about three times.

It is thus possible to measure the smaller C_p, practically as low as 10 μJ K^{-1} at 550 K by use of Type IV. It has been known in the thermal relaxation method that 1/3 of C_p of the surrounding membrane, 1/3C_{link}, contributes to C_{add} [7,40]. In our microcalorimeters, the C_{link} should consist of membrane and leads so that C_{link} equals $V_{membrane} \times \rho_{membrane} \times c_{membrane} + V_{leads} \times \rho_{leads} \times c_{leads}$, where V, ρ, and c represent volume, density, and specific heat of each material, respectively [34,45]. The calculated 1/3C_{link} of Type III (IV) at 300 K was ~6.3 (6.1) μJ K^{-1} while the C_p value of the sample platform in Type III (IV) was estimated to be ~9.4 (1.3) μJ K^{-1}. As a result, the total C_{add} values are estimated to become ~16 μJ K^{-1} and ~7 μJ K^{-1} in Type III and IV microcalorimeters, of which values are in good agreement with the actual data shown in Fig. A.5(a). We note that the C_p value of the silicon oil, ranging from ~1-3 μJ K^{-1}, can also contribute to the experimentally obtained C_{add} in Fig. A.5(a). Therefore, we confirmed by simple estimations and experiments that the C_{add} value of Type IV is clearly smaller than that of Type III by a factor of two at least.

The measured C_p values of an α-Al_2O_3 single crystal are ~170-350 μJ K^{-1} in both Type III and IV micocalorimeters. These C_p data measured with 0.2-0.37 mg samples are much bigger than the C_{add}. These results show that one can safely measure the C_p of the sample with the Type III and IV microcalorimeters without being affected much by the C_{add}. Therefore, errors found in Fig. A.6(b) below in Type III microcalorimeter should not be related to the C_{add} itself.

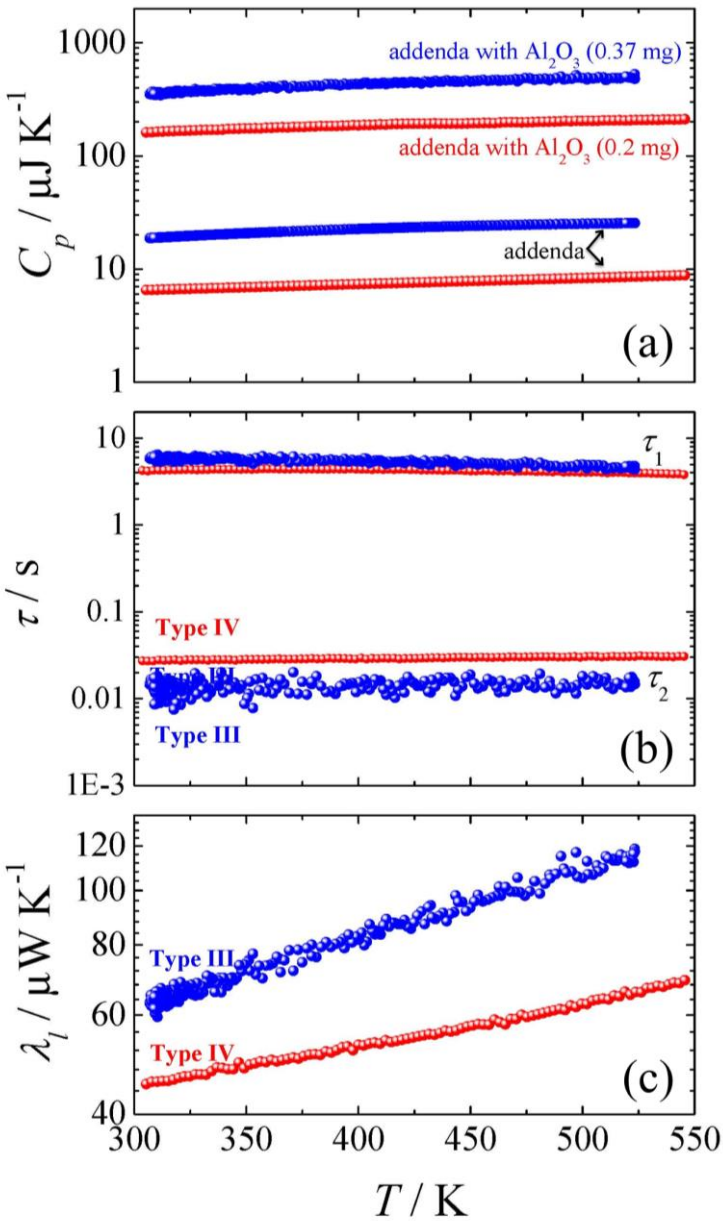

Figure A.5 Temperature dependence of (a) total C_p and C_{add}, (b) the two time constants and (c) λ_l for the Type III (solid blue dots) and IV (solid red dots) microcalorimeters.

Figure A.5(b) shows the temperature dependent evolution of the two time constants during the measurements using the Type III and IV microcalorimeters. Typical fit results

using the two time constants are plotted in our earlier publication (Fig. 4 in Ref. 28) [30]. We found that in both measurements of C_p, the τ_2 value becomes much smaller than τ_1. As shown in Fig. A.5(b), the value of τ_2 is typically ~0.01-0.03 s in both measurements while τ_1 was larger by more than two orders of magnitude (~4.0-6.0 s). This finding shows that the thermal contact between our sample and the sample platform was quite good when the silicon oil was used as the thermal grease. Moreover, the temperature dependence of the time constants is rather monotonous and does not change much between 300 and 550 K, showing the fit results are maintained at overall temperature. When one of the time constant becomes close to 0.01 s or less, there is tendency to have increased noises in the measured data, due to the limit of the measurement speed in the lock-in amplifier (1 kHz with a time constant ~10-30 ms). On the other hand, once the time constants become larger than 0.02 s, the measurements become more stable as indicated by the results for the Type IV microcalorimeter. Thus, one of key reasons to have higher data scatterings and larger standard deviations in Type III (see also, Fig. A.6(b)) may be due to the small τ_2 values while the increased temperature gradient in Type III may also play a role partially.

Figure A.5(c) compares λ_l of Type III (solid blue dots) and IV (solid red dots) microcalorimeters. It is found that λ_l of Type IV at 300 K (44 μW K^{-1}) is smaller than that of Type III (64 μW K^{-1}). Moreover, the slope of λ_l over the temperature is smaller in Type IV than in Type III. According to our previous results [31], the small λ_l was another important factor to increase the accuracy of the C_p measurement in the membrane-based microcalorimeter. Therefore, Type IV is expected to provide the more accurate C_p values at overall temperatures than Type III.

Figure A.6(a) shows the measured c_p of an α-Al_2O_3 single crystal (NIST standard) by using Type III (solid blue dots) and IV (solid red dots) microcalorimeters from 300 to 550 K. Solid black dots are the standard c_p data of an α-Al_2O_3 [46]. The measurement errors of

Type III is as large as 15 % at 300 K and keeps increasing up to about 20 % (Fig. A.6(b)). On the other hand, the measured c_p from Type IV well matches with the standard value within 3 % from 300 to 550 K. It is also found that a standard deviation of the c_p measured by Type IV (~0.45 J mol^{-1} K^{-1}) is smaller than that measured by Type III (~1.57 J mol^{-1} K^{-1}). This result is consistent with the data scatterings appeared in Fig. A.5 and should be attributed to quite small τ_2 values as well as the larger thermal gradient in the Type III microcalorimeter. Combining the thermal simulation and experimental data, all of the results prove that Type IV is superior to Type III in obtaining the smaller C_p data with better accuracy. Concentric geometry of heater/sensor leads allowing the measurement of the temperature inside the circular isothermal region as well as the reduced volume of the platform all seem to be key ingredients in obtaining better heat confinement and thus the smaller C_p with better accuracy.

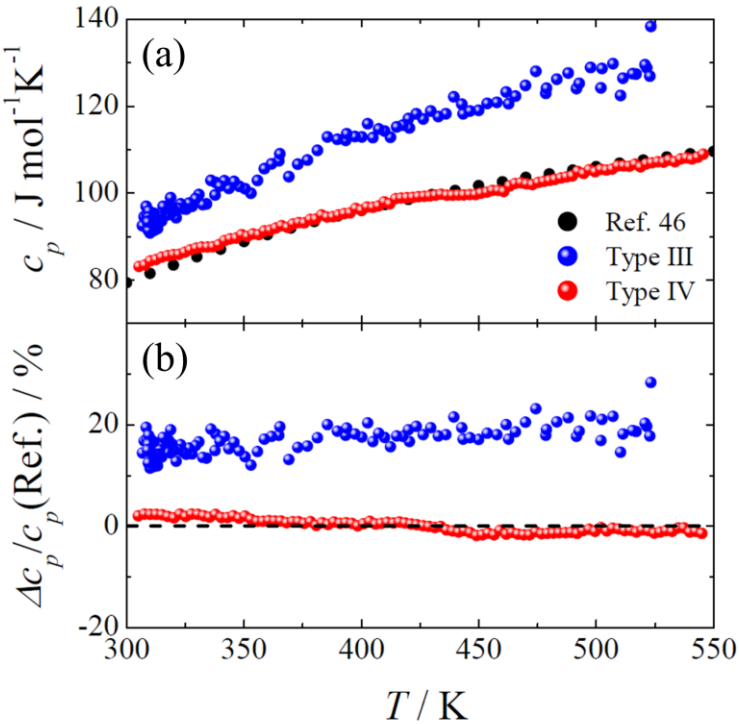

Figure A.6 (a) Temperature dependence of the specific heat, c_p of an α-Al_2O_3 single crystal (NIST standards) as measured by Type III (solid blue dots) and IV (solid red dots) microcalorimeters. The NIST standard values (solid black dots, from Ref. 43) are compared. (b) Temperature dependence of relative errors of the c_p as compared with standard values.

A.4 Summary

Based on the 2D thermal simulation, we have designed and fabricated a new type of microcalorimeter (Type IV) that has two amorphous Si:N and SiO_2 layers as the membrane, and an isothermal platform of a disc shape with concentric Pt leads as a heater and a thermal sensor. As a result, we could achieve a perfect isothermal sample platform from 20 to 600 K. We find that the Type IV microcalorimeter provides a low C_{add} (~6 μJ K^{-1}) value at room temperature and that the uncertainty of the c_p measurement is less than 3 % from 300 to 550 K. The employed microfabrication method putting all heater/sensor leads and

the isothermal meatal layer in one side of the membrane may allow easier fabrication of the nanocalorimeter in future upon further reducing the lateral size of the sample platform and the thickness of the membrane.

Bibliography

[1] T. Kimura, T. Goto, H. Shintani, K. Ishizaka, T. Arima, Y. Tokura, Nature 426 (2003) 55

[2] J.W. Kim, Y.S. Oh, K.S. Suh, Y.D. Park, K.H. Kim, Thermochim. Acta 455 (2007) 2

[3] P.A. Sharma. J.S. Ahn, N. Hur, S. Park, S.B. Kim, S. Lee, J.-G. Park, S. Guha, S.-W. Cheong, Phys. Rev. Lett. 93 (2004) 177202

[4] E.K.H. Salje, M.C. Gallardo, J. Jiménez, F.J. Romero, J.d. Cerro, J. Phys.: Condens. Matter 10 (1998) 5535

[5] R.N. Shelton, L.S. Hausermann-Berg, P. Klavins, H.D. Yang, M.S. Anderson, and C.A. Swenson, Phys. Rev. B 34 (1986) 4590

[6] S.R. Early, F. Hellman, J. Marshall, T.H. Geballe, Physica B+C, 107 (1981) 327

[7] D.W. Denlinger, E.N. Abarra, K. Allen, P.W. Rooney, M.T. Messer, S.K. Watson, F. Hellman, Rev. Sci. Instrum. 65 (1994) 946

[8] S.L. Lai, G. Ramanath, L.H. Allen, P. Infante, Z. Ma, Appl. Phys. Lett. 67 (1995) 1229

[9] F. Fominaya, T. Fournier, P. Gandit, J. Chaussy, Rev. Sci. Instrum. 68 (1997) 4191

[10] K. Xiao, J.M. Gregoire, P.J. McCluskey, J.J. Vlassak, Rev. Sci. Instrum. 83 (2012) 114901

[11] D.R. Queen, F. Hellman, Rev. Sci. Instrum. 80 (2009) 063901

[12] D.W. Cooke, F. Hellman, J.R. Groves, B.M. Clemens, S. Moyerman, E.E. Fullerton, Rev. Sci. Instrum. 82 (2011) 023908

[13] S.A. Adamovsky, A.A. Minakov, C. Schick, Thermochim. Acta 403 (2003) 55

[14] D.R. Queen, X. Liu, J. Karel, T.H. Metcalf, F. Hellman, Phys. Rev. Lett. 110 (2013) 135901

[15] L.P.d.l. Rama, L. Hu, Z. Ye, M.Y. Efremov, L.H. Allen, J. Am. Chem. Soc. 135 (2013) 14286

[16] S. Poran, M. Molina-Ruiz, A. Gérardin, A. Frydman, O. Bourgeois, Rev. Sci. Instrum. 85 (2014) 053903

[17] M.Y. Efremov, E.A. Olson, M. Zhang, F. Schiettekatte, Z. Zhang, L,H. Allen, Rev. Sci. Instrum. 75 (2004) 179

[18] E.A. Olson, M.Y. Efremov, A.T. Kwan, S. Lai, V. Petrova, F. Schiettekatte, J.T. Warren, M. Zhang, L.H. Allen, Appl. Phys. Lett. 77 (2000) 2671

[19] E. Shoifet, Y.Z. Chua, H. Huth, C. Schick, Rev. Sci. Instrum. 84 (2013) 073903

[20] L. Wei, J. Jiang, M. Shan, W. Chen, Y. Deng, G. Xue, D. Zhou, Rev. Sci. Instrum. 85 (2014) 074901

[21] X. Tardif, B. Pignon, N. Boyard, J.W.P. Schmelzer, V. Sobotka, D. Delaunay, C. Schick, Polymer Testing, 36 (2014) 10

[22] Y. Muraoka, S. Yamashita, T. Yamamoto, Y. Nakazawa, Thermochim. Acta 532 (2012) 88

[23] G.A. Jorge, V. Bekeris, M.M. Escobar, S. Goyanes, D. Zilli, A.L. Cukierman, R.J. Candal, Carbon, 48 (2010) 525

[24] W. Ruan, Z. Wang, Y. Li, L. Liu, IEEE Trans. Nanotechnol. 11 (2012) 367

[25] T. Adrega, S.v. Herwaarden, Procedia Engineering 5 (2010) 556

[26] G. Guenther, E. Aulbach, H. Hahn, O. Guillon, Thermochim. Acta 522 (2011) 77

[27] S. Tagliati, V.M. Krasnov, A. Rydh, Rev. Sci. Instrum. 83 (2012) 055107

[28] W. Lee, W. Fon, B. W. Axelrod, M. L. Roukes, Proceedings of the National Academy of Sciences, 106 (2009) 15225

[29] S. v. Herwaarden, E. Iervolino, F. v. Herwaarden , T. Wijffels, A. Leenaersb, V. Mathot, Thermochim. Acta 522 (2011) 46

[30] K.S. Suh, H.J. Kim, Y.D. Park, K.H. Kim, S.-W. Cheong, J. Korean Phys. Soc. 49 (2006) 1370

[31] K.S. Suh, J.W. Kim, H.J. Kim, Y.D. Park, K.H. Kim, Thermochim. Acta 490 (2009) 1

[32] J.W. Kim, P.D.A. Mann, H.J. Kim, K.S. Suh, S.Y. Haam, Y.D. Park, G.R. Stewart, K.H. Kim, Thermochim. Acta 492 (2009) 79

[33] B. Revaz, B.L. Zink, D. O'Neil, L. Hull, F. Hellman, Rev. Sci. Instrum. 74 (2003) 4389

[34] B.L. Zink, F. Hellman, Sol. Stat. Comm. 129 (2004) 199

[35] D.G. Cahill, Rev. Sci. Instrum. 61 (1990) 802

[36] S.-M. Lee, D.G. Cahill, J. Appl. Phys. 81 (1997) 2590

[37] R.L. Powell, W.A. Blanpied, Thermal conductivity of metals and alloys at low temperatures, Nat. Bureau of Standards Circular 556, US Govt. Print. Office (1954)

[38] R.W. Powell, C.Y. Ho, P.E. Liley, Thermal conductivity of selected materials, Nat. Standard Reference Data Series, NSRDS-NBS 8, US Govt. Print. Office (1966)

[39] J.S. Hwang, K.J. Lin, C. Tien, Rev. Sci. Instrum. 68 (1997) 94

[40] R. Bachmann, F.J. DiSalvo Jr., T.H. Geballe, R.L. Greene, R.E. Howard, C.N. King, H.C. Kirsch, K.N. Lee, R.E. Schwall, H.-U. Thomas, R.B. Zubeck, Rev. Sci. Instrum. 43 (1972) 205

[41] Table of total emissivity, Z-88, Omega

[42] L. Giannone, D. Queen, F. Hellman, J.C. Fuchs, Plasma Phys. Control. Fusion 47 (2005) 2123

[43] D. NG, C. M. Spuckler, NASA Technical Memorandum 106252 (1993)

[44] W.H. Gitzen, Alumina as a Ceramic Material, American Ceramic Society, Columbus, Ohio (1970)

[45] A.H. Atabaki, E.S. Hosseini, A.A. Eftekhar, S. Yegnanarayanan, A. Adibi, Optics Express 18 (2010) 18312

[46] D.G. Archer, J. Phys. Chem. Ref. Data 22 (1993) 1441

List of publications

1. High Mobility in a stable transparent perovskite oxide.

Hyung Joon Kim, Useong Kim, Hoon Min Kim, Tai Hoon Kim, Hyo Sik Mun, Byung-Gu Jeon, Kwang Taek Hong, **Woong-Jhae Lee**, Chanjong Ju, Kee Hoon Kim, and Kookrin Char, *Applied Physics Express* ***5***, 061102 (2012).

2. Physical properties of transparent perovskite oxides (Ba,La)SnO_3 with high electrical mobility at room temperature.

Hyung Joon Kim, Useong Kim, Tai Hoon Kim, Jiyeon Kim, Hoon Min Kim, Byung-Gu Jeon, **Woong-Jhae Lee**, Hyo Sik Mun, Kwang Taek Hong, Jaejun Yu, Kookrin Char, and Kee Hoon Kim, Physical Review B **86**, 165205 (2012).

3. Indications of strong neutral impurity scattering in Ba(Sn,Sb)O_3 single crystals.

Hyung Joon Kim, Jiyeon Kim, Tai Hoon Kim, **Woong-Jhae Lee**, Byung-Gu Jeon, Woo Seok Choi, Da Woon Jeong, Jaejun Yu, Tae Won Noh, and Kee Hoon Kim, Physical Review B **88**, 125204 (2013).

4. Determination of temperature-dependent thermal conductivity of a $BaSnO_{3-\delta}$ single crystal by using the 3ω method,

Hyung Joon Kim,Tai Hoon Kim, **Woong-Jhae Lee**, Yisheng Chai, Jae Wook Kim, Yeon Jae Jwa, Sukhwan Chung, Seon Joong Kim, Egon Sohn, Seung Min Lee, Ki-Young Choi, and Kee Hoon Kim, Thermochimica Acta **585**, 16 (2014).

5. New design of a microcalorimeter for measuring absolute heat capacity from 300 to 550 K.

Woong-Jhae Lee, Hyung Joon Kim, Jae Wook Kim, Dong Hak Nam, Ki-Young Choi, and Kee Hoon Kim, Thermochimica Acta **603**, 244 (2015).

6. Oxygen diffusion process in a $Ba_{0.96}La_{0.04}SnO_3$ thin film on $SrTiO_3$(001) substrate as investigated by time-dependent Hall effect measurements.

Woong-Jhae Lee, Hyung Joon Kim, Egon Sohn, Hoon Min Kim, Tai Hoon Kim, Kookrin Char, Jin Hyeok Kim, and Kee Hoon Kim, Physica Status Solidi A **212**, 1487 (2015).

7. Enhanced electron mobility in epitaxial (Ba,La)SnO_3 films on $BaSnO_3$(001) substrates.

Woong-Jhae Lee, Hyung Joon Kim, Egon Sohn, Tai Hoon Kim, Ju-Young Park, Woanseo Park, Hyunhak Jeong, Takhee Lee, Jin Hyeok Kim, Ki-Young Choi, and Kee Hoon Kim, Applied Physics Letters **108**, 082105 (2016).

8. Transparent perovskite barium stannate with high electron mobility and thermal stability.

Woong-Jhae Lee, Hyung Joon Kim, Jeonghun Kang, Dong Hyun Jang, Tai Hoon Kim, Jeong Hyuk Lee, and Kee Hoon Kim, Annual Review of Materials Research **47**, 371 (2017).

9. Single crystal growth and optical properties of a transparent perovskite oxide $LaInO_3$.

Dong Hyun Jang, **Woong-Jhae Lee**, Egon Sohn, Hyung Joon Kim, Dongmin Seo, Ju-Young Park, E. J. Choi, and Kee Hoon Kim, Journal of applied physics **121**, 125109 (2017).

10. Transparent *p*-CuI/*n*-$BaSnO_{3-\delta}$ heterojunctions with a high rectification ratio.

Jeong Hyuk Lee, **Woong-Jhae Lee**, Tai Hoon Kim, Takhee Lee, Seunghun Hong, and Kee Hoon Kim, J. Phys.: Condens. Matter, Accepted.

11 Realization of atomically flat $BaSnO_3$(001) substrate with SnO_2 termination.

Woong-Jhae Lee, Hwangho Lee, Kyung-Tae Ko, Jeonghun Kang, Hyung Joon Kim, Takhee Lee, Jae-Hoon Park, and Kee Hoon Kim, Submitted.

국문 초록

투명 전도성 산화물 및 투명 산화물 반도체는 가시광선 영역에서 투과도가 약 80 % 이상으로 투명하면서도 전기전도도 (~10^{-8} – 10^{3} S cm^{-1})를 갖는 산화물을 의미한다. 지난 20여년 동안 이러한 산화물의 고유한 전기적, 구조적, 광학적 특성을 이용하여 투명 전극, 투명 트랜지스터, 투명 pn다이오드를 활용한 투명 디스플레이, 터치 패널, 스마트 창 등의 투명 전자소자가 활발하게 연구개발되고 있다. 응용소자뿐만 아니라, 최근에는 투명 산화물 반도체 기반 이종접합구조 에서의 높은 전하이동도를 활용한 고속 투명 산화물 반도체 소자 연구가 활발히 진행되어오고 있다. 하지만 대표적인 투명 전도성 산화물인 In_2O_3의 In 고갈 문제, 고온에서의 불안정한 전기적 특성 문제, 기존 반도체에 비해 낮은 상온에서의 전하이동도 문제 등이 보다 우수한 특성을 보이는 새로운 투명 전도성 산화물 개발의 촉매제 역할을 하고 있다. 매장량이 풍부하면서, 고온에서 전기적으로 안정적이며, 상온에서 높은 전하이동도를 가지는 산화물을 찾는 것이 투명 전자소자의 성능 향상뿐만 아니라 향후 Si을 대체할 반도체 융합기술개발과 관련하여 중요한 연구방향 중 하나일 것이다.

2012년 우리는 입방 페로브스카이트 구조의 넓은 밴드갭 (~3.1 eV)을 가지는 $BaSnO_3$의 Ba 자리에 La을 치환한 (Ba,La)SnO_3 단결정을 Cu_2O+CuO 플럭스를 이용한 융제법을 활용하여 세계 최초로 성장하는데 성공하였다. 성장한 단결정이 가시광선 영역에서 투명한 동시에 전자농도 1×10^{20} cm^{-3} 근방에서 최대 320 $cm^2V^{-1}s^{-1}$의 높은 상온 전하이동도를 갖는 n-형 반도체 성질을 보인다는 것을 최초로 보고하였다. 이 전하이동도는 전자농도 10^{20} cm^{-3} 근방에서 산화물 가운데 상온에서 가장 높은 값이다. 또한 (Ba,La)SnO_3의 고온에서의 전기적인 안정성을 확인한 결과, 산소 또는 알곤 분위기에서 (Ba,La)SnO_3 박막의 저항 변화가 10% 이내임을 확인하였고, 공기 분위기에서는 2% 이내로 굉장히 작았다. 이는 (Ba,La)SnO_3의 전기적 특성이 고온에서 매우 안정적, 즉 $BaSnO_3$의 산소가 매우 안정적일 수 있음을 의미한다. 마지막으로 Ba, La, 그리고 Sn의 지구매장량은 In에 비해서 최소 50배 이상 많다. 따라서 (Ba,La)SnO_3의 높은 상온 전하이동도와, 고온에서의 전기적 안정성, 그리고 풍부한 지구매장량을 활용한다면 기존의 투명 산화물 반도체 기반 투명 전자소자의 한계점을 극복하여 차세대 투명 전자소자 구현이 가능 할 것이다.

하지만 $BaSnO_3$ 기반 투명 전자소자 구현을 위해서는 (Ba,La)SnO_3 박막 연구 개발이 필수적이다. 우리는 이를 위해 $SrTiO_3$(001) 기판 위에 (Ba,La)SnO_3 박막을 *c*-축으로 성장하였고, 이 박막의 전하이동도 값이 전자농도 6×10^{20} cm^{-3}에서 최대 ~70 $cm^2V^{-1}s^{-1}$로 단결정에 비해 현저히 작은 것을 확인하였다. 이는 $SrTiO_3$ (~3.905 Å)와 $BaSnO_3$ (~4.116 Å)의 약 5%의 격자상수 차이에 의해 선 어긋나기가 자유 전하에 추가적인 산란을 유도하기 때문이다. 따라서 격자 상수가 맞는 기판을 이용하여 (Ba,La)SnO_3 박막을 성장한다면 자유전자의 산란을 줄여서 단결정과 비

슷한 정도의 높은 전하이동도를 관측할 수 있을 것으로 기대할 수 있다. 하지만 현재까지 $BaSnO_3$의 격자상수와 2% 이내의 차이를 가지는 단결정 기판은 시중에서 판매되고 있지 않다. Cu_2O+CuO 플럭스를 이용한 융제법으로 성장한 $BaSnO_3$ 단결정을 기판으로 활용할 수 있지만, 고온에서 단결정 성장 시 발생한 산소공핍으로 인한 자유전자로 인해 단결정의 전기 전도성이 약 10^3 S·cm^{-1}로 높기에 기판으로 사용하기 부적절하다.

우리는 부족한 단결정 기판에 동기를 부여 받아 전기 절연성 $BaSnO_3$ 단결정을 성장하여 기판으로 활용하고자 다양한 노력을 기울였다. 그 결과 고압합성에 사용하는 $KClO_4$라는 첨가물을 Cu_2O+CuO 플럭스 융제법에 도입함으로서 최초로 전기 절연성 $BaSnO_3$ 단결정 성장에 성공하였다. 성장한 단결정의 비저항을 상온에서 측정한 결과 약 10^{12} ohm·cm으로 높고, 엑스선 오메가 스캔 결과 반값온폭이 0.02 º로 결정질이 우수하여 기판으로 사용하기 적합한 것을 확인하였다. $BaSnO_3$ 단결정의 성분분석 결과 K이 약 0.1 % 검출되었고, 라만 분광학 측정 결과 비저항이 증가함에 따라 일차 라만 봉우리의 크기가 감소하는데, 이를 통해 K이 Ba자리에 치환되어 정공이 증가하여 전자농도를 감소시켰다는 것을 예상 할 수 있다. 이후 전기 절연성 $BaSnO_3$ 단결정의 *c*-축을 잡고 연마도구를 사용하여 표면을 원자단위로 평평하게 연마하였다. 원자힘현미경 측정결과 연마한 $BaSnO_3$(001) 기판 표면의 아르엠에스 거칠기가 0.2 nm로 상용화된 기판의 그것과 거의 비슷한 수준이다. 성장하여 연마한 기판 위에 펄스레이저법을 활용하여 (Ba,La)SnO_3 박막을 성장하였다. 역공간본뜨기 측정 결과 박막이 결맞게 잘 증착되었고, 투과전자현미경 측정결과 박막에 선 어긋나기 등의 결함이 없이 깨끗한 것을 관찰하였다. 또한 상온에서 전하이동도가 최대 102 cm^{2}V^{-1}s^{-1}로 $SrTiO_3$(001) 기판 위에 증착한 (Ba,La)SnO_3 박막의 전하이동도보다 약 45 % 가량 향상 된 것을 확인하였다. $BaSnO_3$를 투명 전자소자로 활용하기 위한 기초 연구로 우리는 성장하여 연마한 $BaSnO_3$(001) 단결정을 기판으로 사용하여 이 위에 $BaSnO_3$ 채널, Al_2O_3 게이트 산화물, Au/Ti의 소스, 드레인, 게이트 전극을 증착하여 $BaSnO_3$ 전계효과트랜지스터를 제작하여, 온/오프 전류비가 1.2 × 10^6이고 전계효과 이동도가 48.7 cm^{2}V^{-1}s^{-1}인 특성을 얻었다.

(Ba,La)SnO_3의 고온에서의 안정된 전기적 특성의 물리적인 근원을 이해하는 것도 중요하다고 말할 수 있다. 우리는 전자석을 이용하여 고온에서 홀 효과 측정이 가능한 셋업을 구축 후, 530 ºC의 산소와 알곤 분위기에서 시간에 따른 (Ba,La)SnO_3 박막의 홀 효과를 측정하였다. 그 결과 (Ba,La)SnO_3의 전하이동도 (전자농도)는 산소공핍이 증가함에 따라 감소(증가)하는 경향을 확인하였다. 전자농도에 따른 전하이동도의 변화를 피팅한 결과, 산소공핍이 이온화된 불순물 산란의 영향이라는 것으로 이해할 수 있었다. 또한 시간에 따른 전자농도의 변화를 통해서 초반의 박막 표면에서의 빠른 산소 반응과 후반의 박막 내부로의 느린 산소 확산의 두 가지 매커니즘으로 분석 할 수 있었다. 또한 시간에 따른 전자농도를 피팅하여 구한 (Ba,La)SnO_3의 산소 확산계수가 약 10^{-16} cm^{2}s^{-1} 정도로 페로브스카이트 산화물 가운데 가장 작은데, 이것이 $BaSnO_3$의 고온에서의 안정된 전기적 특성과 밀접한 관련이 있을 것이라 예상

할 수 있다.

2004년 페로브스카이트 산화물의 이종접합구조 ($LaAlO_3/SrTiO_3$)의 계면에서 이차원전자가스가 발현되어 다양한 물리현상과 함께 활발한 연구가 진행중이다. 만일 $BaSnO_3$ 기반의 이종접합구조에서 이차원전자가스를 구현한다면 전기적으로 안정하면서 높은 전하이동도를 가지는 신 투명 산화물 반도체 전자소자를 바탕으로 기존에 연구되어온 GaN 또는 IGZO 기반의 투명 반도체 소재&소자를 대체할 수 있을 뿐만 아니라 페로브스카이트 산화물 이종접합구조 계면에서 발현하는 이차원전자가스의 메커니즘을 이해할 수 있을 것이다. 하지만 $BaSnO_3$ 기반의 이종접합구조를 구현하기 위해서는 원자단위로 평평하면서 스텝-테라스 구조를 가지는 $BaSnO_3$ 기판 표면 확보가 중요하다. 이를 위해 우리는 먼저 $BaSnO_3$ 기판의 두 가지 틀어짐 각도를 조절하여 표면을 연마하였다. 연마한 기판을 증류수에 식각 후 1200도의 고온에서 다양한 시간동안 어닐링을 시도하였다. 원자힘현미경 측정 결과 $BaSnO_3$ 기판 표면에서 원자단위로 평평한 선명한 스텝-테라스 구조를 확인하였다. 스텝-테라스 표면이 어떠한 원자층으로 구성되어 있는지 확인하고자 방사각에 따른 엑스선광전자분광학을 활용하여 기판을 측정한 결과 테라스 표면이 SnO_2로 구성되어 있다는 것을 분석하였다. 이러한 SnO_2로 종결된 $BaSnO_3$ 기판 위에 면-면 성장법을 활용하여 격자상수가 비슷한 고품질의 극성 또는 비극성 절연체 페로브스카이트 산화물을 접목시킨다면, 전기적으로 안정하면서 높은 전하이동도를 가지는 $BaSnO_3$ 기반 저전력 고속 투명 전자소자 구현이 상온 근방에서 가능할 것이라 예상할 수 있다.

주요어 : 바리움스테네이트, 단결정 성장, 박막 성장, 높은 전하 이동도, 열적 안정성, 이종구조

학번 : 2012-30900